Anizahyati Alisibramulisi

Through Process Modelling of Welded Aluminium Structures

Thesis for the degree of Philosophiae Doctor

Trondheim, November 2013

Norwegian University of Science and Technology
Faculty of Engineering Science and Technology
Department of Structural Engineering

NTNU – Trondheim
Norwegian University of
Science and Technology

NTNU
Norwegian University of Science and Technology

Thesis for the degree of Philosophiae Doctor

Faculty of Engineering Science and Technology
Department of Structural Engineering

ISBN 978-82-471-4788-7 (printed ver.)
ISBN 978-82-471-4789-4 (electronic ver.)
ISSN 1503-8181

Doctoral theses at NTNU, 2013:325

Printed by NTNU-trykk

Abstract

This thesis aims to evaluate the accuracy, efficiency and robustness of a 'Through Process Modelling' concept tailored for analysis of the structural behaviour of welded aluminium structures. In short, the modelling concept relies upon the coupling of a welding simulation tool (WELDSIM), a microstructure model (NaMo) and a non-linear mechanical model (LS-DYNA).

An experimental database addressing the capacity and ductility of simple welded joints of 6xxx and 7xxx alloys have been established. The experimental database includes results from studies on butt-welded specimens of aluminium alloy AA6005, AA6060, AA6061, AA7046 and AA7108. Two tempers; T4 and T6 prior to welding were investigated and the subsequent effects of natural ageing (NA) and post weld heat treatment (PWHT) were assessed. Cross-weld tensile tests were carried out with digital image correlation (DIC) to record the inhomogeneous strain field in these specimens. Variations of the mechanical properties of the material in the vicinity of the weld were further studied by hardness measurements. Uniaxial tensile tests were carried out to document and compare properties of unwelded and welded test specimens in the various conditions. Numerical investigations are carried out based on WELDSIM, NaMo and LS-DYNA for the AA6005, AA6060 and AA6061 alloys. The results are compared with the experimental data to identify present capability and limitations of the modelling approach.

Acknowledgements

I would like to express my deepest gratitude and appreciation to my supervisors: Professor Per Kristian Larsen (NTNU and SIMLab), Adjunct Professor Dr. ing Odd-Geir Lademo (SINTEF Materials and Chemistry and SIMLab) and Adjunct Professor Dr. ing Ole Runar Myhr (Hydro Aluminium and SIMLab) for their professional guidance, input and encouragement.

I would also like to thank Associate Professor Dr. ing Arne Aalberg for his passionate support in the early part of this study. Special thanks to Dr. ing Torodd Berstad for assisting in the numerical work, Dr. ing Stephane Dumoulin for his assistance in digital image correlation technique and Dr. ing Afaf Saai for her scripting assistance. Credits are also given to the laboratory staff at Department of Structural Engineering and Department of Materials and Engineering, NTNU, and at SINTEF Materials and Chemistry, namely: Arne Gellein, Asle Hellesvik, Terje Petersen, Pål Ulseth, Tone Anzjøn, Tore Wisth and Trond Auestad.

I am pleased to acknowledge my fellow PhD students and colleagues at SIMlab for many valuable discussions and stimulating teamwork environment.

This research has been made possible through scholarship granted by Ministry of Higher Education Malaysia (MOHE) and Universiti Teknologi MARA (UiTM), financial support from Norwegian University of Science and Technology (NTNU), Norwegian Research Council (NRC) and industrial support from Hydro Aluminium Structures (HAST), Raufoss. These supports are gratefully acknowledged.

Finally, my warmest appreciation goes to my daughters (Amiratul Soffiya, Amiratul Syuhada, Amiratul Syakirah and Amiratul Solihah) and family for having faith in me throughout this challenging period.

‘Alang-alang menyeluk pekasam, biar sampai ke pangkal lengan – Malay Proverb’

Contents

Notations

$\mathbf{D}$	rate-of-deformation tensor
$\mathbf{R}$	orthogonal rotation tensor
$\hat{\boldsymbol{\sigma}}$	co-rotational stress tensor
$\boldsymbol{\sigma}$	Cauchy stress tensor
$\mathbf{C}$	fourth-order tensor of elastic constants
E	Young's Modulus
v	Poisson's ratio
$\hat{f}$	yield criterion
$\hat{\boldsymbol{q}}$	scalar internal variables
$\bar{\varepsilon}$	effective plastic strain
σ_{y}	yield stress
$\bar{\sigma}$	effective stress
$\dot{\bar{\varepsilon}}$	effective plastic strain rate
$\dot{\lambda}$	plastic multiplier
σ_1	major principal stress
W_{cr}	fracture parameter
σ_f	flow stress
$\Delta\sigma_{\mathrm{d}}$	net contribution from dislocation hardening
σ_i	intrinsic yield strength of pure aluminium
σ_p	strength contribution from hardening precipitates
$\overline{F}$	mean interaction force between dislocations and particles
l	mean planar particle spacing along the bending dislocation
M	Taylor factor
b	magnitude of the Burgers vector
σ_{ss}	strength contribution from atoms in solid solution
C_j	concentration of a specific alloying element in solid solution
k_j	corresponding scaling factor of C_j
α	numerical constant
G	shear modulus
k_1	constant in the evolution equation for statistically storing of dislocations
k_2	constant in the evolution equation for statistically storing of dislocations
k_3	parameter related to the solute dependence of k_2
$\lambda_{g,o}$	geometric slip distance of non-shearable particles
$\rho_{g,s}^{ref}$	density of geometrically necessary dislocations (reference alloy)
ε^*	local plastic strain

ε_c	critical macroscopic strain
ε^p	macroscopic plastic strain
$\hat{C}_{Mg}$	equivalent Mg concentration
f_o	volume fraction of non-shearable particles
V	voltage
AA	aluminium alloy
HAZ	heat affected zone
PWHT	post weld heat treatment
NA	naturally aged
T4	solution heat treated and naturally aged
T6	solution heat treated and artificially aged
T7	solution heat treated and overaged or stabilized
KTL	heat treatment used by car manufacturers (German abbreviation)
$s_{0.2}$	yield stress at 0.2% permanent strain
s_{ult}	ultimate engineering tensile strength
DIC	digital image correlation
u_{dic}	deformation from DIC technique
u_{50}	deformation from extensometer
u_{ch}	deformation from crosshead
s	nominal stress
A	cross section area
A_0	initial cross section area
F	force
D	deformation capacity
$P_{0.2}$	conventional strength at 0.2% permanent strain
P_u	ultimate strength in uniaxial tensile test
δ_u	deformation corresponding to P_u
$\delta_{0.2}$	deformation corresponding to $P_{0.2}$
e_u	engineering strain at diffuse necking or maximum load
HV	Vickers hardness
L	radius of local thinning
NL	radius of non-local thinning

List of figures

List of tables

1 Introduction

1.1 Background

Welded components made of age-hardening aluminium alloys are to an increasing extent used within the transport and automotive industries due to their high strength, good formability, low density, and good resistance to general corrosion. However, in certain cases, the application of such alloys is restricted by a low strength in the heat affected zone (HAZ) due to softening reactions occurring during welding, which tend to reduce the overall load-bearing capacity of the component. In order to utilise the properties of aluminium alloys fully, a better understanding of the strength and ductility of welded joints is needed. In particular, it is imperative to be able to account for the effects of this manufacturing process on the structural crashworthiness. Proper modelling tools and concepts are required to meet the industrial need for rapid development and low cost of new products.

Figure 1.1 (a) and (b) show possible process routes for the manufacturing of a welded automotive sub-structure, where a number of different processing conditions and alloy combinations are feasible. Aluminium alloys have a strong memory of the previous processes, and thus a modelling procedure able to follow the process route and thereby, to properly predict the structural response is required. Such a procedure, which is illustrated by Figure 1.1 (c), is often denoted ‘Through Process Modelling (TPM)’. The evaluation of a particular TPM concept for applications within the automotive industry is the topic of the present investigation.

The present study is focused on a limited number of ‘downstream’ thermal process steps, as indicated by the orange frame in Figure 1.1 (a), while addressing a number of initial conditions, alloys and Post-Weld Heat Treatment (PWHT) procedures, see Figure 1.1 (b).

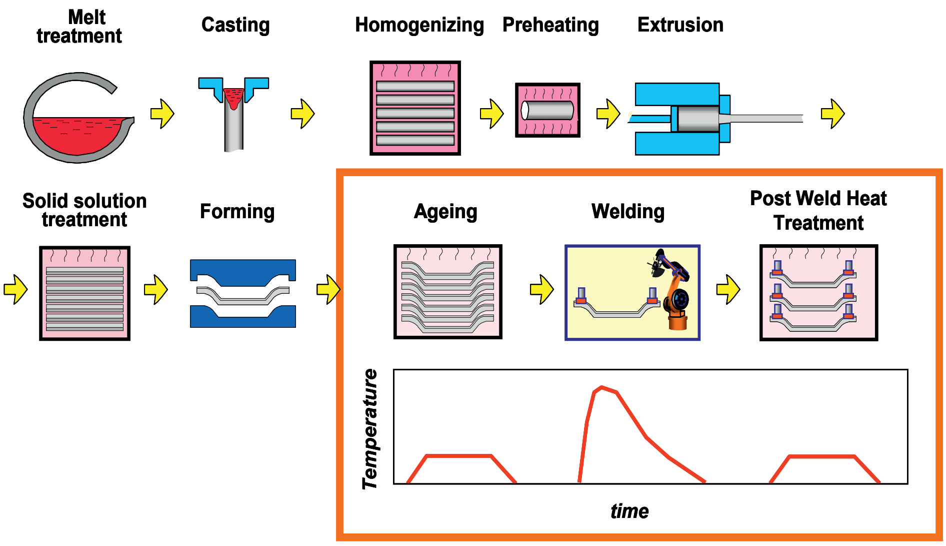

(a)

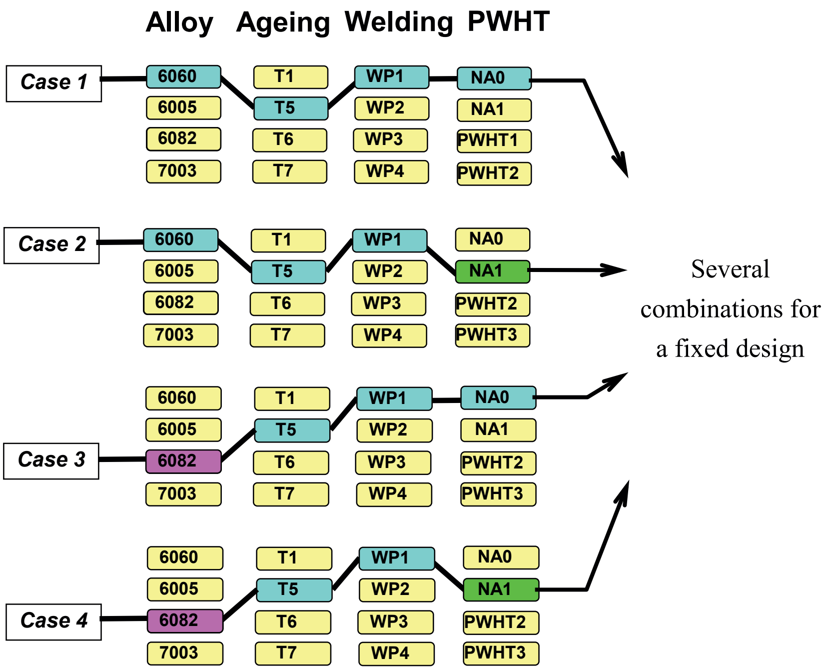

(b)

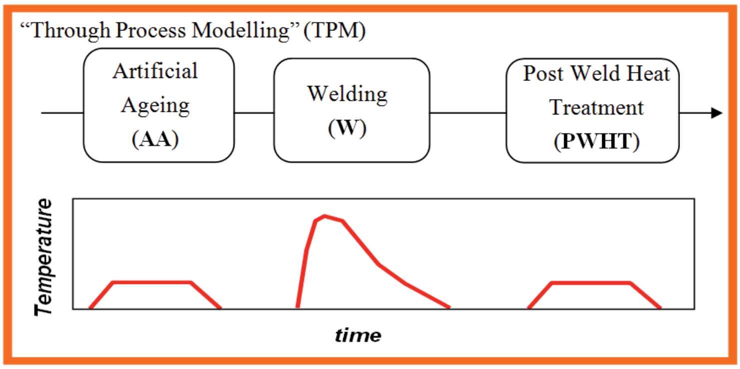

(c)

Figure 1.1: (a) A typical processing route for manufacturing of welded automotive components [20], (b) possible process and material combinations and (c) schematic temperature history for a specific material point in the structure as a basis for Through Process Modelling (TPM).

1.2 Review of previous works

Attempts of predicting the deformation behaviour, strength and ductility of welded components have been done by many researchers.

Matusiak [18] provided experimental data for planar butt and fillet welded connections and for the structural behaviour of welded beam-to-column joints in aluminium alloy 6082-T6. The joints consist of an unstiffened I-section subjected to a transverse tensile force by means of a plate fillet welded to the flange. His modelling efforts showed that the behaviour could be reproduced numerically, provided the mechanical properties of the material in the weld zone were correctly represented. However, it was beyond the scope of his work to properly predict the ultimate failure of the structure.

Nègre et al. [36] used the Gurson-Tvergaard-Needleman fracture model (GTN) for the simulation of crack extension due to ductile tearing of laser welded aluminium sheets. Good agreement was obtained between experiments and simulations.

Hildrum [12] studied the behaviour of butt-welded stiffened panels made of aluminium extrusions subjected to impact by a dropped object. The weld and HAZ were modelled with reduced strength, and the Lemaitre damage model was used to predict the response until failure. The numerical simulations predicted reasonably well the plastic instability (strain localization) and fracture process observed in the experiments.

Zheng et al. [15] studied the fracture of butt welds, using local strain gauge measurements and a single-parameter, mesh-dependent fracture model to fit the experimental data. The method has been extended in several papers, predicting fracture initiation and growth for structures under crash and impact loading.

Wang et al. [41] used shell elements to model the welded beam-to-column joints previously studied by Matusiak. The textured alloy was modelled using an anisotropic plasticity model, and the inhomogeneous work-hardening properties of the HAZ were accounted for in the material modelling. It was found that the numerical results were strongly mesh dependent. To obtain reliable results for both strength and ductility, the concept of non-local plastic thinning was used in the HAZ. This procedure reduces the mesh dependence of the strain localization at the cost of introducing one additional parameter, namely the radius of the non-local domain. The non-local approach was originally proposed by Bazant and Pijaudier-Gabot in 1988 [44].

Based on fundamental metallurgical principles, Myhr et al. [29] did process modelling for 6082-T6 aluminium weldments. They discussed how the hardness distribution in the HAZ depended on the interplay between two competing processes; dissolution and reprecipitation. Their microstructure model was based on elements from thermodynamics and kinetic theory that allowed predicting the hardness distribution after reheating and subsequent natural ageing, with a minimum of unknown calibration constants.

Myhr et al. [26, 28] combined precipitation, yield strength, work-hardening and mechanical models with the aim to optimize the performance of welded automotive components made of age hardening Al-Mg-Si alloys. They concluded that the main parameters that influence the structural performance in addition to the geometry and boundary condition are the; alloy composition, initial base plate temper condition, applied heat input during welding and subsequent post weld heat treatment. This model concept is the motivation of the present study as these parameters are accounted for in the numerical simulation.

Dørum et al. [5] investigate two methods for estimating the ductility in large-scale analyses of welded aluminium connections. The first approach was to link the element size to the length scale of failure mechanism and the second approach was to 'lump' the weakest zone of the HAZ into rows of cohesive elements and the corresponding traction-separation law. The local necking and fracture in the HAZ were modelled in an efficient way by these approaches. This study was a purely numerical one, i.e. it lacked validation against experimental data. Their study provides valuable comparisons between approaches based on brick, shell and cohesive elements, of strong relevance to the present study.

It can be concluded that, in order to obtain realistic simulation of the material response of age hardening aluminium alloys, due consideration must be given to welding and physically based yield strength and work hardening modelling. Thus, this thesis will build upon the work of Myhr et al. [26, 28] and aim to evaluate its accuracy, efficiency and robustness when applied to different alloys, initial conditions and PWHT schemes.

1.3 Objective

Primary objective:

The overall objective of the present study is to evaluate the accuracy, efficiency and robustness of the 'Through Process Modelling' concept previously developed, discussed and evaluated by Myhr et al. [24, 25, 26, 28] and Dørum et al. [5]. The evaluation will cover various heat-treatable aluminium alloys in the 6xxx and 7xxx series, in different initial temper conditions and relevant PWHT schemes.

Secondary objectives:

1) To establish an experimental database addressing the capacity and ductility of simple welded joints made of heat-treatable aluminium structures suited for the overall objective.
2) To perform numerical investigations based on the TPM concept.
3) The numerical study shall document present capabilities and limitations of the present sub-model versions and identify needs for further research.

1.4 Scope

To meet with the objectives, it was decided to set up an experimental campaign on generic welded 'structures' in the form of simple butt welded test specimens that were subjected to cross-weld tensile testing. The campaign investigates effects of the main steps in the manufacturing of the joints; initial ageing and condition of the material, welding and PWHT. Five different alloys (AA6005, AA6060, AA6061, AA7046 and AA7108), two initial tempers (T4 and T6) and four different PWHT schemes were selected. In addition to cross-weld tensile testing of the generic joints, the experimental programme covers uniaxial tensile and hardness tests. The study is limited to testing under quasi-static conditions.

In the numerical investigation, the scheme presented by Myhr et al. [28] is to be followed. A thermo-mechanical analysis [23], of the welding process is carried out by means of WELDSIM [21, 22, 23, 31, 33] to determine the temperature field in the weld, HAZ and surrounding base material. This field of thermal histories is used as an input to the microstructure model NaMo [25, 26, 27, 30] which determines the spatial distribution of the mechanical properties in the HAZ. These results are then transferred to LS-DYNA [16] for the structural response analysis. This work is carried out for the three 6xxx alloys, only, since further development of the NaMo model is found to be needed for 7xxx alloys. The experimental and numerical data are used to document present capabilities and limitations of the modelling concept.

1.5 Organisation of the report

The theoretical background for the work is outlined in Chapter 2. In Chapter 3, experimental results are reported, i.e. results from uniaxial tensile tests, hardness tests, and cross-weld tensile tests. In Chapter 4, comparisons between numerical simulations and experiments are presented and discussed. Chapter 5 draws the overall conclusions and gives recommendations for further work.

2 Theoretical background

2.1 Introduction

The main properties that make aluminium a valuable structural material are its low weight, high strength, recyclability, corrosion resistance, durability, ductility and formability. Due to this unique combination of properties, the variety of applications of aluminium continues to increase. Aluminium is weak in its pure form, and is normally only used in thin foils. However, alloying elements are added to aluminium to increase its strength or improve its other properties. The yield strength of pure aluminium is about 10 MPa, whereas the yield strength for commercial aluminium alloys ranges from about 50 MPa to 500 MPa. The strength increase is due to alloying elements that are dissolved in the aluminium matrix and finely distributed small particles that obstruct dislocation movements, and thus prevent plastic slip, which is the normal deformation mechanism in aluminium alloys at room temperature. Another way of strengthening aluminium alloys is by work hardening, e.g. through cold deformation, which leads to an increase in the dislocation density and a corresponding increase in obstacles for plastic slip.

The 6xxx series contains both soft and medium strength alloys that can be strengthened by heat treatment (precipitation hardening), due to the presence of the alloying elements silicon and magnesium. These alloys are generally weaker than the 2xxx and 7xxx series, but have good formability and are weldable. They also have excellent corrosion resistance. Precipitation hardening of the alloys is possible when silicon is combined with magnesium; forming (typically and among other) Mg_5Si_6 precipitates [4].

7xxx series are also heat treatable alloys that can be strengthened through precipitation hardening based on the combination of zinc and magnesium. However, these alloys are prone to stress corrosion. The 7xxx series may also contain Cu to increase the age-hardening potential and Zirconium (Zr) to refine the grain structure by inhibiting recrystallization. Here, the precipitating phases contain Mg and Zn in different combinations, while the stable equilibrium phase is $MgZn_2$. These series are known as high strength alloys [13].

The mechanical properties of a welded aluminium structure depend in general on the welding process and its parameters, in particular on the reduced strength of the HAZ. Previous research has led to the conclusion that a proper modelling must encompass realistic welding simulations and physically based work hardening models, allowing alloy, welding process and even PWHT to be accounted for [45]. Motivated by this conclusion, the current investigation is novel in a way that the mechanical input data for the FEM simulations are obtained by means of process simulation, and not by means of material tests.

2.2 Heat-treatable alloys

The precipitate structure is the prime factor that regulates the yield strength and work-hardening behaviour of heat-treatable aluminium alloys. The precipitate structure is rewegoverned by the chemical composition of the alloy and the thermal history of the material element. In order to predict the structural response of a welded aluminium component or parts, it is utmost important to understand the evolution of the precipitate structure during thermo-mechanical processing and its relation to the mechanical properties of the material. The present section provides a brief description of precipitates in Al-Mg-Si and Al-Mg-Zn alloys, and their dependency to thermal processing. A model that quantifies the precipitate structure, and the associated strength and work hardening of the material as function of thermal history is presented in Section 2.3.2.

Al-Mg-Si (6xxx) alloys

For Al-Mg-Si alloys, the precipitation sequence following quenching from a high temperature (i.e. the solid solution temperature) is generally accepted as [4, 19]:

$$\text{SSSS} \rightarrow \text{clusters} \rightarrow \text{GP zones (spherical)} \rightarrow \beta'' \text{ (needle)} \rightarrow \beta' \text{ (rod)} \rightarrow \beta \text{ } (Mg_2Si)$$

Here, SSSS means supersaturated solid solution, which means that the concentrations of Mg and Si atoms in the aluminium matrix are higher than the equilibrium concentration of these elements, leading to the formation of Si and Mg rich clusters during ageing. Then, different metastable phases form according to the sequence above, i.e. Guinier-Preston zones (GP zones) β'' and β' and finally the stable equilibrium β (Mg_2Si) phase.

This highly idealised precipitation sequence is rarely seen for typical industrial processes involving non-isothermal heat treatments like welding, where certain phases, like for instance β' may form directly from the supersaturated solid solution during cooling. The complex series of reactions taking place in the heat affected zone during welding of Al-Mg-Si alloys is described by Myhr et al. [25] and can be summarized as follows: During artificial ageing (AA), a high density of fine, needle-shaped β'' particles form uniformly in the matrix, as shown in Figure 2.1 (a). However, since these precipitates are thermodynamically unstable in a welding situation (W), the smallest ones will start to dissolve in the parts of the HAZ where the peak temperature has been above 250°C, while the larger ones will continue to grow. At the same time, coarse rod-shaped β' precipitates may form in the intermediate peak temperature range between 250 and 480°C, as indicated in Figure 2.1 (b). If welding is followed by a post weld heat treatment (PWHT), reprecipitation of hardening β'' particles will take place within the high peak temperature regions of the HAZ, as shown in Figure 2.1 (c). This occurs to an extent, which depends both on the matrix vacancy concentration and the level of Mg and Si in solid solution. Accordingly, the reprecipitation would be expected to be most extensive in the fully reverted region close to the weld fusion line owing to the combined effect of a high solute content and a high concentration of quenched-in vacancies. Conversely, the renewed β'' formation will be suppressed in parts of the HAZ where the peak temperature is lower because the aluminium matrix in these regions will be depleted with respect to vacancies and solute. This eventually leads to the development of a permanent soft region within the weld HAZ after PWHT [25].

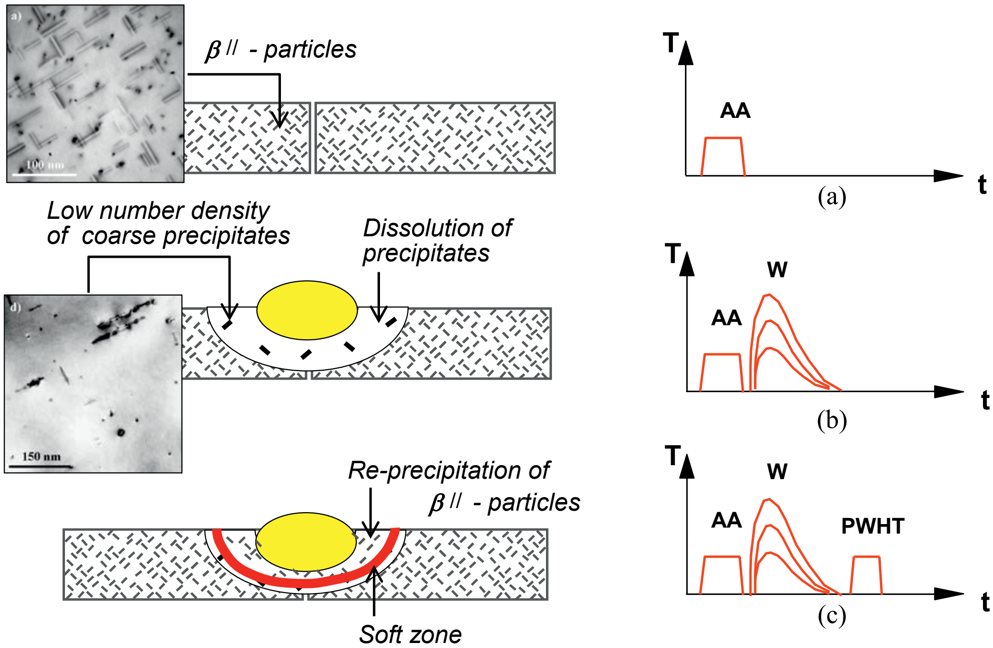

Figure 2.1: Evolution of the precipitate structure in the HAZ during heat treatment and welding of Al-Mg-Si (6xxx)-alloys. AA: artificial ageing, W: welding, PWHT: post weld heat treatment. The outer boundary of the HAZ is the curved lines [31]

Al-Mg-Zn (7xxx) alloys

For Al-Mg-Zn alloys, the precipitation sequence is generally accepted to be as follows:

$$\text{SSSS} \rightarrow \text{GP I zones} \rightarrow \text{GP II zones} \rightarrow \eta' \rightarrow \eta\ (MgZn_2) \qquad [3]$$

GP I zones, GP II zones and η′ are the phases that contribute to the precipitation hardening of the alloys in the underaged and peak-aged conditions, while η forms during overaging [11]. Aging of the alloys in the temperature range of 100–120°C usually leads to the formation of GP zones [9], while a subsequent aging in the temperature range of 140–170°C results in the formation of η´ and η phases, depending on the extent of aging [40]. In welding it is the reversed processes in the sequence above that are of main concern i.e. dissolution of strengthening precipitates that become unstable during heating, and the associated coarsening of precipitates that survive the thermal cycle. These reactions occur, to an extent depending on the peak temperatures and retention times experienced by the different regions of the HAZ. Full or partial dissolution of the strengthening precipitates occurs within the peak temperature range from about 200 to 340°C [22]. During the cooling stage of the welding, the cooling rates are usually high enough to suppress any reprecipitation. Hence, immediately after welding the HAZ yield stress or hardness will be low close to the weld fusion line. Most of the lost strength in this zone can be recovered by natural ageing due to extensive GP-zone formation after a period of 3-5 months [22]. PWHT causing reprecipitation of the hardening metastable phases is an even more efficient way to recover the strength loss in the HAZ [22].

Thermal cycles and temper conditions

The properties of a given material point in a heat-treatable alloy depend upon its precipitate structure and are governed by the alloy and the thermal history of the material element. The thermal process cycle for material elements in a welded aluminium structure is illustrated in Figure 2.2.

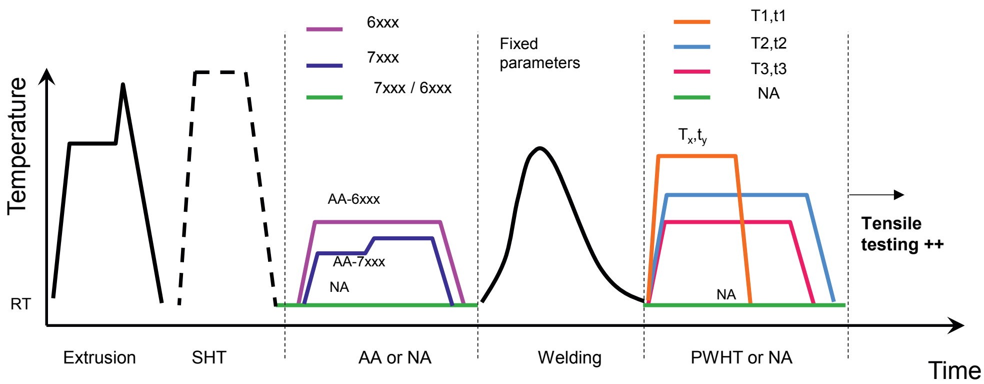

Figure 2.2: A schematic diagram illustrating the different processes and heat treatment schedules applied in the present study for preparation of welded plates for subsequent testing.

The second and third process steps are called Precipitation Hardening or Age Hardening and involves [13]: 'Solution Heat Treatment' (SHT) followed by quenching to create a supersaturated solid solution (SSSS) and 'Aging' to facilitate the formation of small finely dispersed precipitates which strengthen the alloy by acting as obstacles for dislocations during plastic deformation. The SHT is done by keeping the alloy in the so-called one-phase region of the equilibrium phase diagram, where a solid solution of the elements represents the thermodynamic stable phase, which means that precipitates such as Mg_2Si in the 6xxx series are dissolved. At the same time, high concentrations of vacancies are obtained. Water quenching is done in order to "freeze" the structure, i.e. both alloying elements in solid solution as a basis for precipitation, as well as vacancies which are necessary in order to achieve a rapid "transportation" of the elements by diffusion. The final ageing heat treatment can be achieved in two ways, i.e. by natural ageing (NA) or artificial ageing (AA). *Natural ageing* means prolonged storing at room temperature, where clusters start to form immediately. The formation of GP zones is slow due to a low diffusion rate at room temperature, which means that the corresponding increase in yield stress and hardness is also sluggish. *Artificial ageing* involves reheating to a temperature below the dissolution (solvus) temperature resulting in a more efficient formation of precipitates.

The different temper conditions for age-hardening aluminium alloys are defined in [13]. Three conditions are particularly relevant for the current investigation:

- T4: Solution heat treated and naturally aged to a substantially stable condition
- T6: Solution heat treated and artificially aged to peak hardness
- T7: Solution heat treated and artificially aged (overaged)

2.3 Constitutive and fracture modelling

The material response is in general characterized by constitutive equations which give the stresses as a function of the deformation history and certain internal state variables. An elastic-plastic constitutive model is used to describe the material behaviour of the aluminium alloys. In the elastic region, the material is assumed to be linear (Hooke's law) and to be isotropic. For modelling the plastic behaviour, the von Mises yield criterion, the associated plastic flow rule and isotropic hardening are here assumed.

In an elasto-plastic response analysis, the stress-strain curve has to be known for each integration (material) point in the structure. Each of these points may have undergone different thermal history during the welding, post weld heat treatment and aging, and will thus have a unique curve. Except in certain special cases an experimental determination of each of these curves is not feasible.

In the present investigation the yield (flow) stress and hardening at each point are determined by means of the micro-structure model NaMo [25, 26, 27, 28, 30] that tracks the evolution of precipitates and solid solution levels as a function of the thermal histories, as described in Section 2.4. By performing an incremental thermo-elastic analysis, spanning both the - welding and ageing process, by means of the WELDSIM program [21, 22, 23, 31, 33] the spatial distribution of the temperature as a function of time is determined throughout the structure. At each point and time instance, the precipitation model determines the particle size distribution (PSD), which provides the input, to a yield strength and work hardening model. By combining the results from the yield strength and work hardening models, the complete stress-strain curves can be estimated. Finally, the commercial FE-code LS-DYNA [16] is used to simulate the structural response of welded components. This was done by transferring the predicted stress-strain curves to the mechanical model.

2.3.1 Theory of plasticity

The constitutive model used in the subsequent finite element analysis is based on the theory of plasticity, using the von Mises yield criterion, associated flow rule, and isotropic hardening rule. The finite-strain formulation is used in the presentation, and large rotations are accounted for by use of a co-rotational formulation [39]. Small elastic strains are assumed. Hypoelastic-plastic models are typically used when elastic strains are small compared to plastic strains [39]. In addition, the concept of non local thinning for plane stress analyses, as proposed by Wang et al. [41] and the Cockroft Latham fracture criterion [17] are used respectively to reduce mesh dependence of strain localisation and to predict ductile fracture. In the formulation, a superposed “hat” denotes the co-rotational formulation and a superposed dot specifies material time differentiation.

The co-rotational rate-of-deformation tensor is decomposed into elastic and plastic parts:

$$\hat{\mathbf{D}}=\hat{\mathbf{D}}^{e}+\hat{\mathbf{D}}^{p}, \qquad \hat{\mathbf{D}}=\mathbf{R}^{T}\cdot\mathbf{D}\cdot\mathbf{R} \tag{2.1}$$

Where indices e and p denote elastic and plastic parts, respectively, $\mathbf{D}$ is the rate-of-deformation tensor and $\mathbf{R}$ is the orthogonal rotation tensor [39].

The hypoelastic stress-strain relation between the rate of co-rotational stress tensor and the elastic co-rotational rate-of-deformation tensor is defined as:

$$\dot{\hat{\boldsymbol{\sigma}}}=\mathbf{C}:\hat{\mathbf{D}}^{e}=\mathbf{C}:(\mathbf{D}-\hat{\mathbf{D}}^{p}), \qquad \hat{\boldsymbol{\sigma}}=\mathbf{R}^{T}\cdot\boldsymbol{\sigma}\cdot\mathbf{R} \tag{2.2}$$

Where $\hat{\boldsymbol{\sigma}}$ is the co-rotational stress tensor, $\boldsymbol{\sigma}$ is the Cauchy stress tensor and $\mathbf{C}$ is the fourth-order tensor of elastic constants. Assuming elastic isotropy, $\mathbf{C}$ depends on Young’s Modulus E and Poisson’s ratio v.

Yield function

The yield function defines the boundary between fully elastic and elastic-plastic behaviour, and evolves with material hardening. In this study, von Mises criterion is employed since it is the most widely used yield criterion for metallic materials which exhibit plastic incompressibility and from the modelling done proven to be acceptable. The criterion assumes isotropy, and plane stress is assumed in the analyses. The yield function *f* defines the elastic domain in stress space and expressed as:

$$\hat{f}(\hat{\boldsymbol{\sigma}},\hat{\mathbf{q}})=0 \tag{2.3}$$

Where $\hat{f}$ is the yield criterion and $\hat{\boldsymbol{q}}$ is a collection of scalar internal variables. The material behaves elastic when $\hat{f} < 0$, and plastic when the yield condition $\hat{f}=0$ is satisfied during deformation. When $\hat{\boldsymbol{q}}$ includes the effective plastic strain $\bar{\varepsilon}$ only; the yield criterion is defined as:

$$\hat{f}(\hat{\boldsymbol{\sigma}},\bar{\varepsilon})=\bar{\sigma}(\hat{\boldsymbol{\sigma}})-\sigma_y(\bar{\varepsilon}) \tag{2.4}$$

Where $\sigma_y(\bar{\varepsilon})$ is the flow stress in uniaxial tension and $\bar{\sigma}$ is the effective stress. The history of plastic deformation in metal plasticity is often characterized by the effective plastic strain, $\bar{\varepsilon}$ which is given by [39]:

$$\bar{\varepsilon}=\int \dot{\bar{\varepsilon}}\,dt \tag{2.5}$$

$\dot{\bar{\varepsilon}}$ is the effective plastic strain rate and can be defined from the specific plastic work rate as follows. The effective stress and strain rate and the Cauchy stress and the plastic rate-of-deformation are pairs of energy conjugate measures:

$$\dot{W}^{\mathrm{p}}=\hat{\boldsymbol{\sigma}}:\hat{\mathbf{D}}^{\mathrm{p}}=\bar{\sigma}\cdot\dot{\bar{\varepsilon}} \tag{2.6}$$

Flow rule

The flow rule describes the direction of the plastic strain increment. For metals, the rule of normality is commonly employed, where the plastic strain increment is directed along the outward normal of a flow potential. For the associated flow rule, the yield surface is taken as the flow potential of the plastic strain-rate tensor. Thus, the plastic rate-of-deformation and the equivalent plastic strain rate are given as [39]:

$$\hat{\mathbf{D}}^{\mathrm{p}} = \dot{\lambda}\frac{\partial \hat{f}}{\partial \hat{\boldsymbol{\sigma}}} \tag{2.7}$$

$$\dot{\bar{\varepsilon}} = \frac{\hat{\boldsymbol{\sigma}} : \hat{\mathbf{D}}^{\mathrm{p}}}{\bar{\sigma}} = \frac{\hat{\boldsymbol{\sigma}} : \left(\dot{\lambda}\frac{\partial \hat{f}}{\partial \hat{\boldsymbol{\sigma}}}\right)}{\bar{\sigma}} = \frac{\dot{\lambda}}{\bar{\sigma}}\hat{\boldsymbol{\sigma}} : \frac{\partial \hat{f}}{\partial \hat{\boldsymbol{\sigma}}} \tag{2.8}$$

Where,

$$\hat{\boldsymbol{\sigma}} : \frac{\partial \hat{f}}{\partial \hat{\boldsymbol{\sigma}}} = \bar{\sigma}, \qquad \text{thus: } \dot{\bar{\varepsilon}} = \dot{\lambda} \tag{2.9}$$

The loading and unloading conditions are written in the Kuhn-Tucker form:

$$\dot{\lambda} \geq 0, \hat{f} \leq 0, \dot{\lambda}\hat{f} = 0 \tag{2.10}$$

These equations are used to define plastic loading and elastic unloading, while the consistency condition $\dot{f} = 0$ determines the plastic multiplier, $\dot{\lambda}$ during a plastic process. When the yield condition $\hat{f} = 0$ is met; only plastic deformation will occur. During plastic loading ($\dot{\lambda} > 0$) the stress must remain on the yield surface, so that $\dot{f} = 0$. For elastic unloading $\dot{\lambda} = 0$, i.e., there is no plastic flow.

Hardening rule

The hardening rule describes the evolution of the yield surface with progressive yielding. Isotropic hardening is employed in this study, i.e. the yield surface expands uniformly in stress space as a function of the equivalent plastic strain, i.e. through equation $\sigma_y(\bar{\varepsilon})$. In the present study, the function is represented by the NaMo model concept as described in following section.

2.3.2 Microstructure model - NaMo

The microstructure model - NaMo (Nano Structure Model) [28] contains a precipitation model that calculates the time evolution of the Particle Size Distribution (PSD), which can be used to quantify the characteristics of the precipitate structure. The following presentation is based on ref [5, 25, 26, 27, 28, 30, 33]. Figure 2.3 shows the parameters extracted from the PSD, which are subsequently transferred to the yield stress and work-hardening models, respectively.

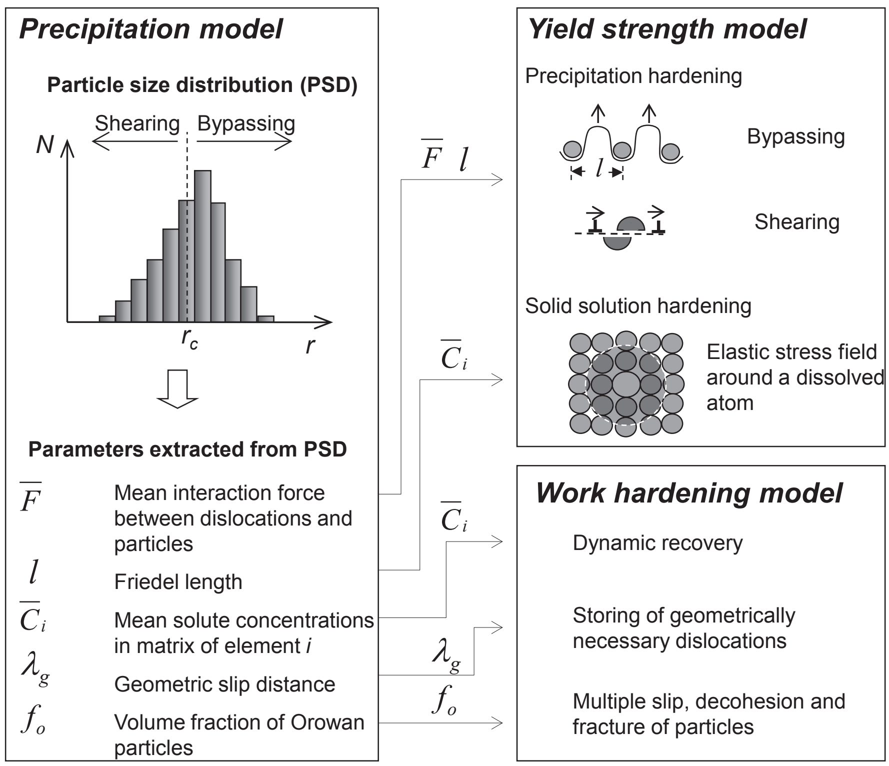

Figure 2.3: Parameters extracted from the Particle Size Distribution (PSD) and transferred to the yield stress and work hardening model [5]

The stress-strain curve can be determined from the effective plastic strain $\bar{\varepsilon}$ and the flow stress σ_f given by:

$$\sigma_f = \sigma_{\mathrm{y}} + \Delta\sigma_{\mathrm{d}} \tag{2.11}$$

Here, σ_{y} and $\Delta\sigma_{\mathrm{d}}$ are the yield stress and the net contribution from dislocation hardening respectively, both predicted from the precipitation model. By combining the results from the yield strength and the work-hardening models, the complete stress-strain curves at any position of the HAZ can be estimated and then transferred to LS-DYNA for the resulting mechanical response analysis.

Precipitation model

The precipitation model by Myhr and Grong [25, 26, 27, 30] is the key component in both the yield strength and the work hardening models. The model consists of the following three components:

(1) A nucleation law, which predicts the number of stable nuclei that form at each time step.

(2) A rate law, which calculates either the dissolution or the growth rate of each discrete particle size class.

(3) A continuity equation, which keeps a record of the amount of solute being tied up in the precipitates.

Yield strength model

The yield strength model converts the relevant output parameters from the precipitation model into an equivalent room temperature yield stress through dislocation mechanics.

The individual contributions to the overall macroscopic yield strength σ_y are given as follows:

$$\sigma_y = \sigma_i + \sigma_p + \sigma_{ss} \tag{2.12}$$

Where σ_i is the intrinsic yield strength of pure aluminium and σ_p is the precipitation hardening contribution, given by:

$$\sigma_p = \frac{M\overline{F}}{bl} \tag{2.13}$$

The mean interaction force $\overline{F}$ between dislocations and particles and the mean planar particle spacing *l* along the bending dislocation are both extracted from the PSD. *M* is the Taylor factor and *b* is the magnitude of the Burgers vector. σ_{ss} is the solid solution hardening potential of the alloy, which is calculated from the solid solution concentrations, and can be estimated from the following expression [30]:

$$\sigma_{ss} = \sum_j k_j C_j^{2/3} \tag{2.14}$$

Here, C_j is the concentration of a specific alloying element in solid solution and k_j is the corresponding scaling factor.

Work hardening model

The work hardening model predicts the individual evolution of statistically stored and geometrically necessary dislocations, respectively, based on well established evolution laws. The work-hardening model includes the precipitate structure through the fully integrated NaMo model. Thus, any changes in the particle size distribution due to heat treatment or welding will be reflected by a corresponding change in the work-hardening response, as represented by the net contribution from dislocation hardening $\Delta\sigma_d$ expressed by the response equation:

$$\Delta\sigma_d = \alpha MGb\sqrt{\left(\frac{k_1}{k_2}\right)^2\left[1-\exp\left(\frac{-k_2\varepsilon^p}{2}\right)\right]^2 + \rho_{g,s}^{ref}\frac{\lambda_{g,0}^{ref}}{\lambda_{g,0}}\frac{\varepsilon^*}{\varepsilon_c^{ref}}} \tag{2.15}$$

Here, α is a numerical constant and G is the shear modulus, k_1 is a model parameter, expressing the rate of generation of statistically stored dislocations during plastic straining. The alloy dependent parameter k_2 expresses the rate of dynamic recovery of statistically stored dislocations during plastic deformation. $\lambda_{g,o}$ and $\lambda_{g,o}^{ref}$ are the geometric slip distances, based on non-shearable particles, of an alloy and of the reference system, respectively. ε^* and ε_c^{ref} are the local plastic strain and the critical macroscopic strain for the reference system. $\rho_{g,s}^{ref}$ is the density of geometrically necessary dislocations. The parameters σ_y, k_2, $\lambda_{g,0}$ and ε_c are field variables that depend on the thermal history. The remaining parameters in Eq. (2.15) are independent of the thermal history. The index *ref* means a chosen reference alloy.

It is more convenient to introduce the parameters $\omega = \alpha MGb$ and $k_3 = \rho_{g,s}^{ref}\lambda_{g,0}^{ref}/\varepsilon_c^{ref}$ in Eq. (2.15) after which Eq. (2.11) reads:

$$\sigma_f(\varepsilon^p) = \sigma_y + \omega\sqrt{\left(\frac{k_1}{k_2}\right)^2\left[1-\exp\left(\frac{-k_2\varepsilon^p}{2}\right)\right]^2 + k_3\frac{\varepsilon^*}{\lambda_{g,0}}} \tag{2.16}$$

Hart [9] gives the relationship between the macroscopic plastic strain ε^p and local plastic strain ε^* by the differential equation:

$$\frac{d\varepsilon^*}{d\varepsilon^p} = 1 - \left(\frac{\varepsilon^*}{\varepsilon_c}\right)^n \tag{2.17}$$

From Eq. (2.17) it follows that the local strain ε^* is equal to the macroscopic plastic strain ε_p at small deformations, but approaches ε_c at large deformations for all relevant n values. Thus, in the limiting case, when $n = \infty$, the strain may be written as:

$$\varepsilon^* = \begin{cases} \varepsilon^p & \text{when } \varepsilon^p \le \varepsilon_c \\ \varepsilon_c & \text{when } \varepsilon^p > \varepsilon_c \end{cases} \tag{2.18}$$

The other parameters in Eq. (2.15), i.e. k_2 and ε_c, depend on the equivalent Mg concentration, $\hat{C}_{Mg}$, and the volume fraction of non-shearable particles, f_o, respectively, through the relationship:

$$k_2 = k_2^{\min} + \left(k_2^{\max} - k_2^{\min}\right)\exp\left(-\frac{\hat{C}_{Mg}}{\hat{C}_{Mg}^{ref}}\right) \tag{2.19}$$

$$\varepsilon_c = \frac{f_o^{ref}}{f_o}\varepsilon_c^{ref} \tag{2.20}$$

In Eq. (2.19), $k_2^{\min}$ and $k_2^{\max}$ are material dependent constants, and $\hat{C}_{Mg}^{ref}$ is the equivalent Mg concentration for the reference alloy, and in Eq. (2.10) ε_c^{ref} corresponds to the critical plastic strain for the reference material. A summary of the input data used in this NaMo model is listed in Table 2.1.

Table 2.1: Summary of input data used in the NaMo model [5]

Parameter	Value	Comments
α	0.30	Numerical constant
M	3.1	Taylor factor
G (N/m^2)	2.7x10^{10}	Shear modulus
b (m)	2.86x10^{-10}	Burgers vector
k_1 (m^{-1})	4x10^8	Material dependent constant related to the storing rate of statistically stored dislocations
k_3 (m^{-1})	4x10^8	Parameter related to the solute dependence of k_2
$\lambda_{g,o}^{ref}$ (m)	4.06x10^{-7}	Calculated from PSD
f_o^{ref}	0.0109	Calculated from PSD
ε_c^{ref}	0.05	Critical strain for a chosen reference material
$\rho_{g,s}^{ref}$ (m^{-2})	4.93x10^{13}	Density of geometrically necessary dislocations for a chosen reference material
$k_2^{\min}$	10	Estimated minimum constant in Eq. (2.19)
$k_2^{\max}$	70	Estimated maximum constant in Eq. (2.19)
$\hat{C}_{Mg}^{ref}$ (wt%)	0.35	Equivalent Mg concentration
σ_i (MPa)	10	Intrinsic yield stress of pure aluminium

2.4 Through-process modelling

The modelling strategy in the present study is to couple the thermal model (WELDSIM), the microstructure model (NaMo) and the mechanical model (LS-DYNA), as illustrated in Figure 2.4. NaMo is a stand-alone programme, with physical and mathematical background as described above. The FE tools, WELDSIM and LS-DYNA are presented in brief below, along with a description on how the information is transferred between, and used within, the different codes.

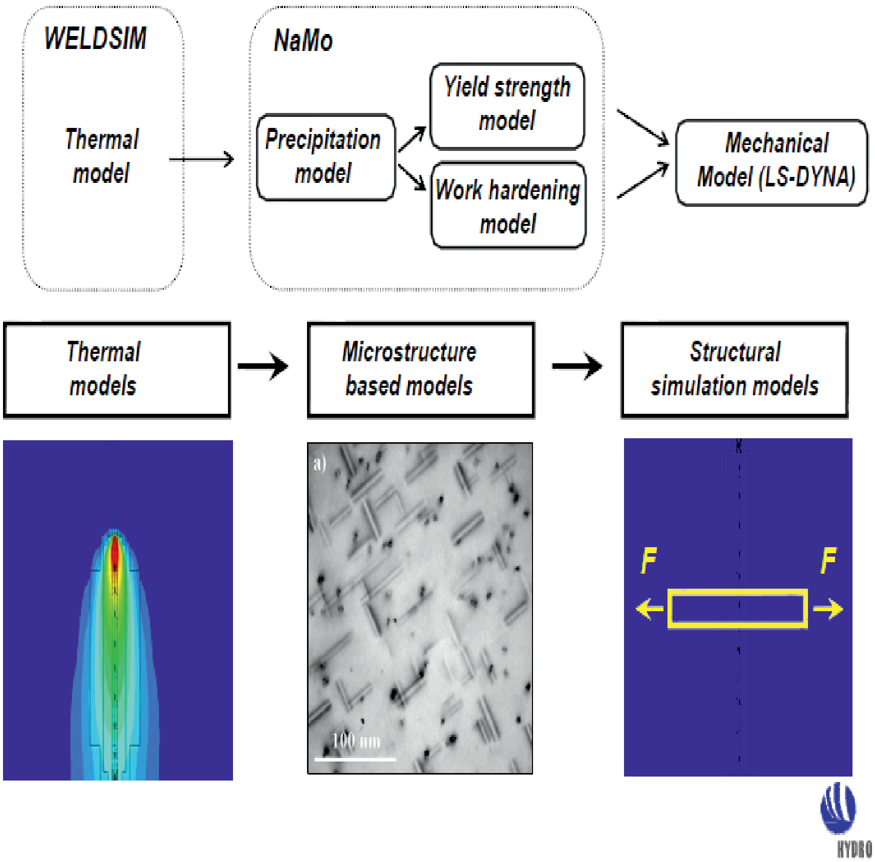

Figure 2.4: Through-process modelling - coupling of models [20]

Thermal model – WELDSIM

WELDSIM [21, 22, 23, 31, 33] is a special-purpose FE code for analysis of welding processes. The code is built upon three different modules, i.e. a thermal, a microstructure and a mechanical module, as presented in Figure 2.5. The program predicts the thermal field caused by welding processes, and estimates distortions and stresses due to welding. The microstructure module in the code is a basic variant of the NaMo subroutine used in the present work. WELDSIM has been demonstrated to be a powerful and accurate modelling tool, and it has for instance been used to optimize residual stresses and to minimize distortions [22, 23] as well as to optimize dimensions of welded components made of age-hardening aluminium alloys [33]. Figure 2.6 shows the main input and output of WELDSIM. The present work relies upon the thermal module of WELDSIM to predict the temperature field resulting from the welding process.

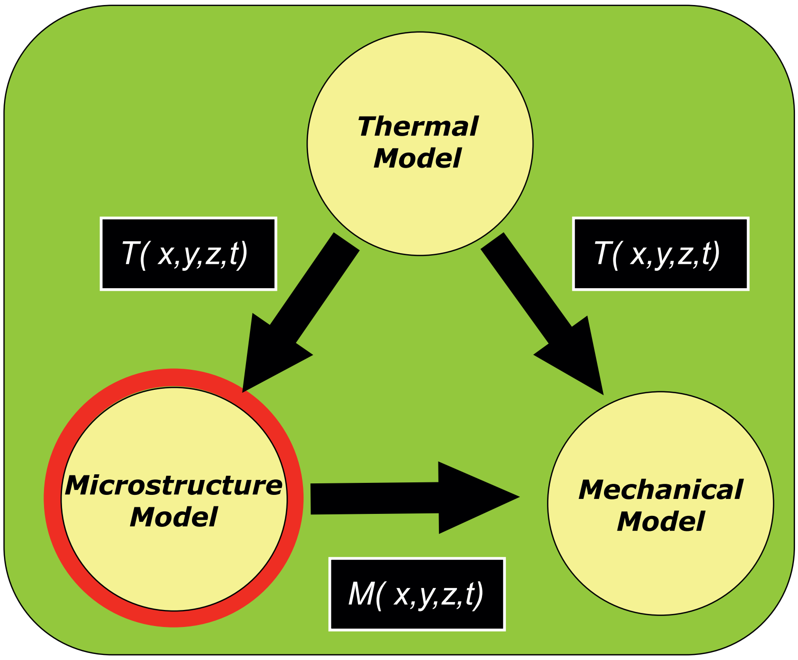

Figure 2.5: Basic structure of WELDSIM [21]

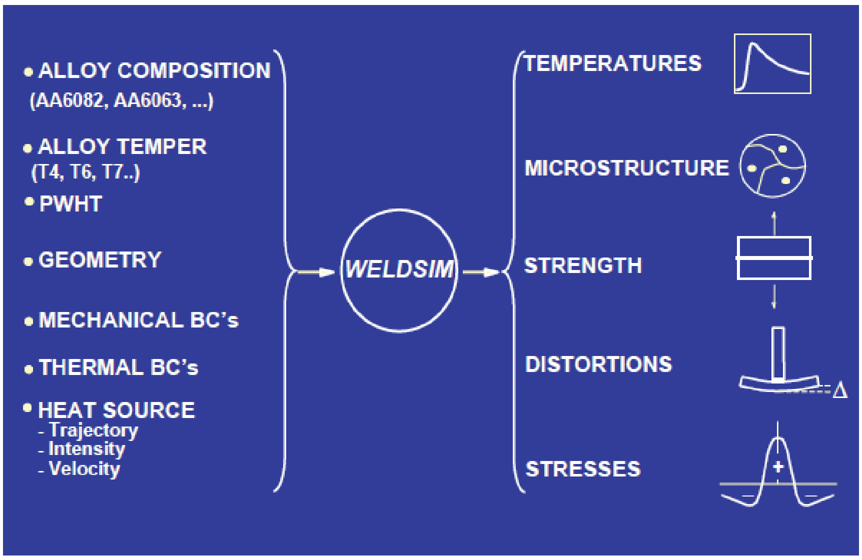

Figure 2.6: Main input and output from WELDSIM [33]

Mechanical model – LS-DYNA

LS-DYNA [16] is a general-purpose, nonlinear FE code for analyzing large deformation response of inelastic solids and structures, with both implicit and explicit solution capabilities. LS-DYNA can simulate and analyse highly nonlinear physical phenomenons occurred in real world problems. Usually such phenomenons are associated with large deformations within short time duration, e.g. crashworthiness simulations. Moreover, LS-DYNA provides many features making it a very powerful tool to solve a broad spectrum of applications.

The constitutive and fracture modelling concept presented in Section 2.3 has been implemented as a user-defined material model in the work of Myhr et al. [28], and is used in this study. Thus, the constitutive model assumes the von Mises yield criterion, associated flow rule, while the isotropic strength and strain hardening are identified from a microstructure model concept. The parameters σ_y, k_2, $\lambda_{g,0}$ and ε_c of the work-hardening model are provided by NaMo based on the alloy composition and thermal history obtained from WELDSIM.

2.5 Summary of the modelling strategy

The coupling of the three models in the present study is used to investigate the resulting cross-weld tensile properties of welded aluminium plates. This concept is also applicable for the analyses of real components e.g. in optimising the load bearing capacity of welded crash boxes of bumper systems made of age-hardening Al-Mg-Si alloys as illustrated in Figure 2.7.

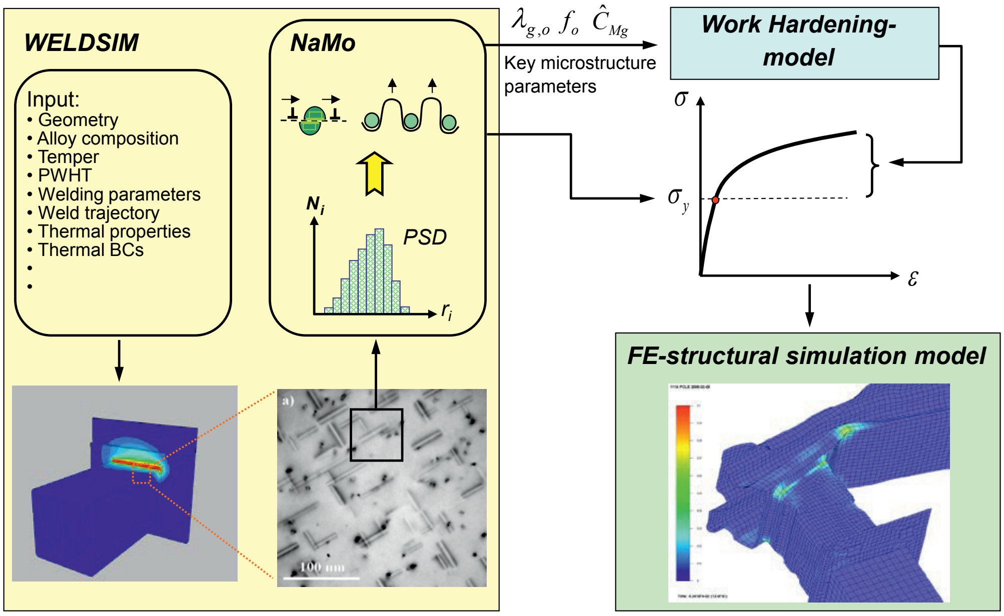

Figure 2.7: Summary of modelling strategy [24]

3 Experiments

3.1 Materials

Five alloys, each in two initial temper conditions, are investigated. The alloys are AA6005, AA6060, AA6061, AA7046 and AA7108 with chemical composition provided in Table 3.1. Flat profiles with quadratic cross section (200 mm by 3 mm) were extruded from each alloy. The extrusions were cut in lengths of 400 mm and given heat treatments corresponding to tempers T4 and T6. The alloys were selected by the former Hydro Aluminium Structures, Raufoss, Norway (now Benteler Aluminium Systems - BAS), which is a key industry in this project. All alloys are used in various industrial automotive components and assemblies.

Table 3.1: Chemical composition (in weight %)

Alloy	Composition								
	Fe	Si	Cu	Mg	Cr	Mn	Zn	Zr	Ti
7108	0.19	0.09	0.01	1.23	0.003	0.01	5.69	0.17	0
7046	0.19	0.09	0.01	1.22	0.003	0.009	6.59	0.16	0
6061	0.20	0.62	0.19	0.79	0.01	0.06	0.01	0.002	0.008
6060	0.21	0.53	0.001	0.41	0.001	0.02	0.01	0.001	0.01
6005	0.21	0.63	0.01	0.44	0.005	0.14	0.03	0.004	0.01

3.2 Welding

The plates were butt-welded along the extrusion direction to form a plate with nominal width and length of 400 mm, with the weld along its centre line. The plates were pulsed

MIG-welded using single sided welding and stainless steel backing. The aluminium-based filler material used was AlMg4.5Mn.

The butt welded plates were consecutively numbered after welding. A total of 27 welded plates were produced, but only 10 of these have been investigated in the present test programme. An overview of the alloys, tempers and plate identifiers are given in Table 3.2. The tempering conditions T4 and T6 is presented in more detail in Section 3.3. The plate identifiers refer to the numbering obtained from Hydro Aluminium Structures, and are stated here for future reference. No further reference to the plate identifiers is given in this report.

Table 3.2: Alloys, temper conditions and plate numbers

Alloy identifiers	Type of alloy	Butt welded plates in T4 condition marked as	Butt welded plates in T6 condition marked as
A	6005	23	7
B	6060	26	6
C	6061	22	1
D	7046	19	15
E	7108	21	12

The welding parameters are shown in Table 3.3 while the welding of the plates is illustrated in Figure 3.1. Ideally, both the weld metal and the HAZ should have strength comparable to, or higher than the parent metal. Heat-treatable aluminium alloys are, however, highly affected by the thermal history imposed to the material by the welding (see Section 2.2). The extent and magnitude of the property change in the HAZ depends primarily on the base metal composition, the geometry of the welded structure, the heat input provided by the welding process and the welding speed [25, 33].

Table 3.3: Welding parameters

Current [A]	Voltage [V]	Welding speed [mm/s]	Arc efficiency (assumed)	Predicted deposit area [mm^2]
145.0	15.8	16.0	0.8	10.0

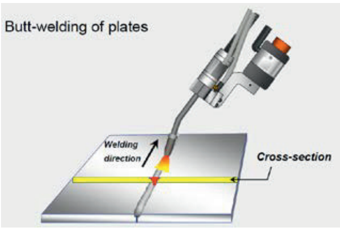

(a)

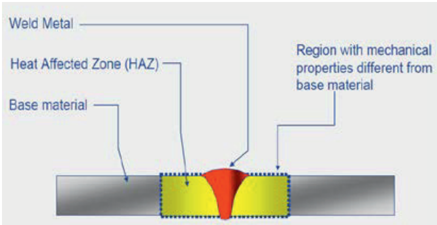

(b)

Figure 3.1: MIG welding of aluminium (a) butt-welded plates and (b) the Heat Affected Zones (HAZ) [20]

3.3 Post-Weld Heat treatment schemes

Four different schemes for PWHT have been investigated. The schemes are motivated by thermal cycles which are commonly imposed to the material in an industrial process chain, and they can be summarised as follows:

NA: Naturally aged at room temperature for more than 1 week.

PWHT-T6: Motivated by peak-aging T6 thermal cycle conditions.

PWHT-T7: Motivated by over-ageing T7 thermal cycle conditions.

PWHT-KTL: Heat treated to 195°C for 30 minutes.

The latter scheme is motivated by the typical thermal cycle resulting from paint baking of automotive structures, while the other schemes simulate – experimentally – conditions that could result from the production of for example bumper beam systems. PWHT was performed on blanks and specimens as discussed in the following.

3.4 Test programme and specimens preparation

The test programme shall produce an experimental database that addresses the capacity and ductility of simplistic welded joints of the five heat-treatable aluminium alloys in question. Generic welded joints are obtained by production of cross-weld tensile test specimens. In addition, hardness profiles and uniaxial stress-strain curves are to be obtained for the various alloys and PWHT schemes. In total the experimental programme comprises:

- 80 cross-weld tensile tests
- 80 uniaxial tensile test
- 40 hardness tests

All test specimens are oriented 90° to the extrusion direction.

From the welded plates, eight 40 mm wide blanks were cut perpendicular to the weld line and designated I, II, III, IV, V, VI, VII and VIII, see Figure 3.2. The blanks were next machined to provide the specimen geometry shown in Figure 3.3. Figure 3.2 also shows the location of specimens for hardness measurements. The uniaxial tensile tests of the base material were machined from different plates but having the same alloy and initial temper condition. All machining was done at Department of Structural Engineering, NTNU.

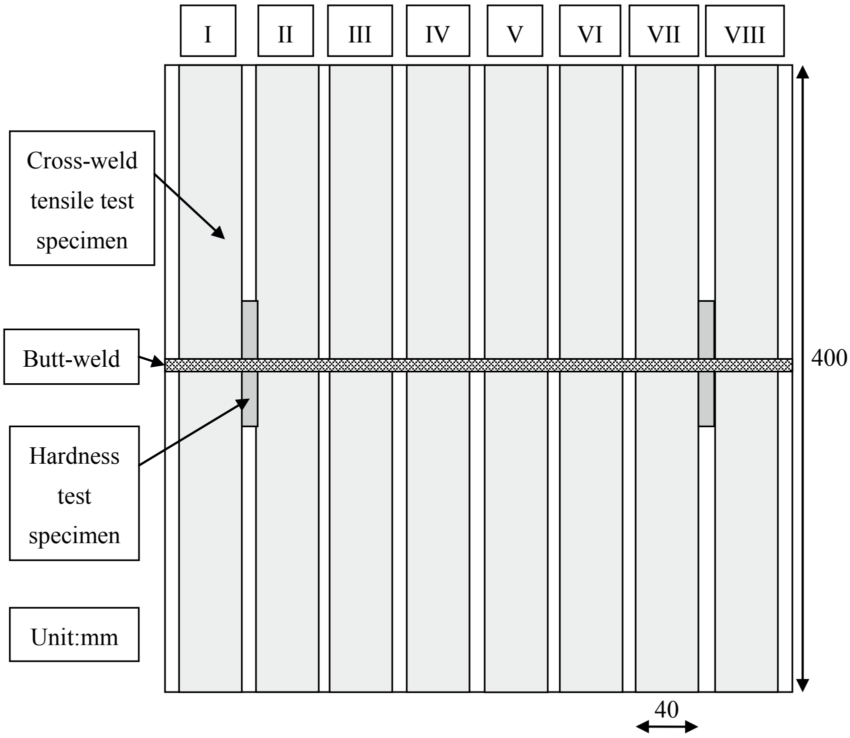

Figure 3.2: Butt-welded plate, blanks for cross-weld tensile tests, and positions of hardness profile measurements

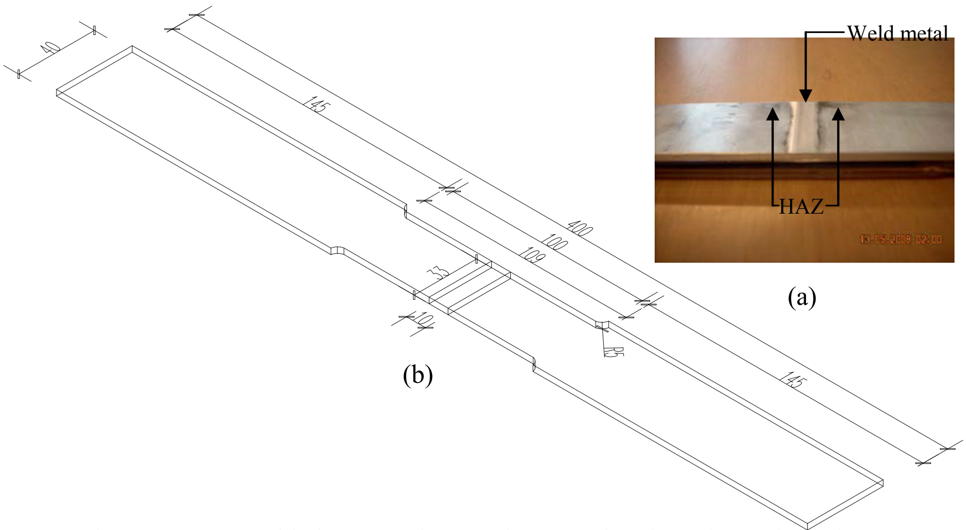

Figure 3.3: (a) Welded test specimens, (b) CAD drawing of actual specimen

The cross-weld tensile test specimens were identified by a designation X-T-Z-Y, where:

X = alloy (identifiers stated in Table 3.2)

T = initial temper condition (T4, T6)

Z = welded plate number (1-27)

Y = specimen number (I-VIII)

An example of a specimen designation is A-T4-23-VII.

The following pairs of cross-weld tensile specimens were subject to the different PHWT schemes (stated in parentheses): I&III (NA), II&IV (T6), V&VII (T7) and VI&VIII (KTL). Four hardness test specimens were taken from each welded plate and designated as M1A, M1B, M2A and M2B (also illustrated in
Figure 3.2).

The artificial PWHT ageing were performed in a furnace at the laboratory of Department of Materials Science and Engineering, NTNU. The blanks for the cross-weld tensile test, the uniaxial test coupons and the specimens for hardness measurements were aged in single batches for the individual alloys. The ageing schemes are summarised Table 3.4. The naturally aged specimens were stored at room temperature for more than one week, independent of alloy. The KTL PWHT is motivated by the thermal paint-baking process used in the automotive industry and was also the same for all alloys. The 'T6' and 'T7' PWHT schemes follows different schemes for the 6xxx and 7xxx alloys, and are deduced by detailed insight in the precipitation sequences, briefly discussed in Section 2.2.

Table 3.4: PWHT schemes

AA	NA	T6	T7	KTL
7108	RT > 1 week	5h/100+6h/150°C	5h/100+6h/180°C	30min/195°C
7046	"	"	"	"
6061	"	7h/185°C	7h/215°C	"
6060	"	"	"	"
6005	"	"	"	"

*Note: Initial T6 for AA6xxx:175°C/10h and AA7xxx:100°C/5h+150°C/6h

In what follows, results from the uniaxial tensile tests, hardness tests and cross-weld tensile tests are presented in Sections 3.5, 3.6 and 3.7, respectively.

3.5 Uniaxial tensile tests - base material

The uniaxial tensile test is the most common test to determine the strength and work hardening of materials. Key information, often reported in tables, are the yield strength ($s_{0.2}$), the (engineering) ultimate tensile strength (s_u) and some ductility measurement(s), most often the engineering strain (e_u) corresponding to the ultimate tensile strength.

In the present work these tests provides the means to evaluate the NaMo concept with respect to its description of the base material strength and work hardening. Strain-rate effects are outside the scope of the present investigation. Thus, all tests were performed at a quasi-static strain-rate.

For safety reason most structures are required to behave in a ductile manner, i.e. they shall have the ability to sustain large plastic deformation prior to failure. This requires that also the materials are ductile. Non-ductile structures are denoted brittle, and may fail without warning in the form of extensive deformations. There is no unique definition of structural ductility, and in the present investigation a definition proposed by Mazzolani and Piluso 1995 [8] is used:

$$D = \frac{\delta_u - \delta_{0.2}}{\delta_{0.2}} \tag{3.1}$$

Here, D is the structural ductility, δ_u is the deformation at ultimate load P_u, and $\delta_{0.2}$ is the deformation that corresponds to the load $P_{0.2}$ giving 0.2% permanent elongation. The ratio $P_u/P_{0.2}$ gives information on the work hardening. These additional measures, D and $P_u/P_{0.2}$, are also presented in the consecutive tables.

3.5.1 Test procedure

Five alloys in two initial conditions, and each subject to four PWHT schemes leads to 40 distinct materials/conditions. For each condition, 2 duplicate tests were performed, which results in a total of 80 uniaxial test specimens. The geometry of all specimens was carefully measured before testing. The tensile tests were done in an Instron machine with a 20 kN load cell. The tests were performed at room temperature under displacement control and with a crosshead displacement rate of 2 mm/min. An extensometer with a 20 mm gauge length was used to measure the strains in the centre gauge section. The geometry of the specimens is provided in Figure 3.4 while the test set up is shown in Figure 3.5. All data were recorded with Instron Bluehill Software version 2.12.

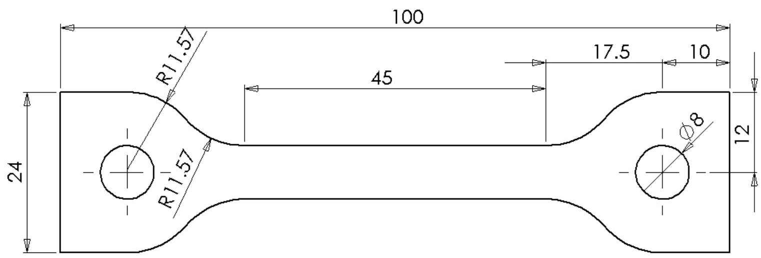

Figure 3.4: Uniaxial tensile test specimen dimensions [42]

Figure 3.5: Uniaxial tensile test set up

3.5.2 Test results

In the following, test results in the form of engineering stress vs. engineering strain curves are presented for all alloys and processing conditions. The curves are labelled according to the PWHT scheme imposed to the materials; NA, T6, T7 or KTL. In other words, the curves labelled NA (natural ageing) refer to specimens that have been naturally aged (room temperature) until the same age as the other specimens. The NA curves thus represent the response of the as-delivered ('virgin materials').

NOTE: Since an extensometer, only, was used to measure the specimen elongation, the curves are plotted up to the onset of necking (ultimate force). Beyond this point the extensometer elongation measurement is dependent upon the position of the neck in the gauge section and invalid.

The following formulae were employed to calculate the engineering stress s and engineering strain e:

$$s = \frac{F}{A_o} \tag{3.2}$$

$$e = \frac{L - L_o}{L_o} \tag{3.3}$$

Here F is the measured force, A_o is the initial cross-sectional area of the specimen, L is the extensometer length and L_o is the initial extensometer gauge length. Based on these measures, the stress at 0.2% plastic strain $s_{0.2}$, the ultimate engineering stress s_u and the corresponding engineering strain e_u were tabulated for each material (alloy, initial condition and PWHT).

AA6060

Figure 3.6 and Table 3.5 present the results from the uniaxial tensile tests on the AA6060 alloy. It is evident (and expected) that the initial temper greatly affects the tensile properties of the material. In the as-delivered conditions (i.e. the NA curves in a) and b)); the $s_{0.2}$ is significantly lower in T4 than in the peak-aged T6 condition. The work hardening is, however, considerably larger for the former condition. In agreement with Considers' classical criterion [2] for the onset of diffuse necking, this leads to a more ductile specimen response for the T4 compared with the T6 condition.

From a theoretical point of view the T6 condition is, per definition, the peak aged condition of the material. Consequently, further thermal processing should reduce the material strength, due to precipitate coarsening. For initial condition T4, the precipitate structure is not in peak-aged size and distribution. Thus, the PWHT schemes represent an artificial ageing sequence that shall increase the strength of the material. The strength increase occurs on the cost of a reduced work hardening, i.e. causing a reduction of the specimen ductility towards the levels seen for the material in the as-delivered T6 condition. Principally, the experimental results are in accordance with theory, except that the T6 PWHT scheme causes a slight strength increase also for the material in as-delivered T6 condition. This is to be expected if the received T6 material was slightly underaged rather than aged to peak strength. Then prolonged heating at the ageing temperature corresponding to PWHT-T6 would lead to a strength increase similar to one observed in Figure 3.6(b). It is not uncommon for industrially produced materials that the T6 condition does not correspond to the real peak strength that can be obtained for the alloy due to a non-optimised ageing practice.

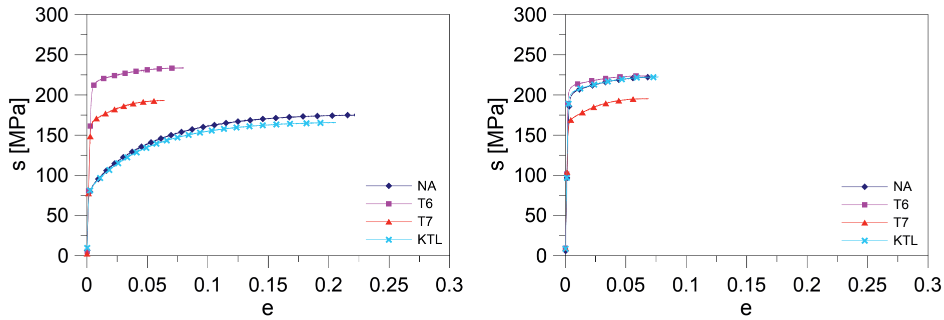

(a) Initial T4 (b) Initial T6

Figure 3.6: Uniaxial tensile test results of AA6060, label indicates PWHT scheme

Table 3.5: Effect of PWHT schemes on AA6060 – characteristic measures

Condition	PWHT and label	$s_{0.2}$ [MPa]	s_{ult} [MPa]	e_u [mm/mm]	D	$\frac{P_u}{P_{0.2}}$
T4	NA	84	175	0.221	64.7	2.1
	T6	212	234	0.080	13.4	1.1
	T7	167	193	0.064	12.2	1.2
	KTL	84	166	0.206	62.0	2.0
T6	NA	199	223	0.075	14.6	1.1
	T6	209	224	0.068	14.3	1.1
	T7	169	196	0.069	15.3	1.2
	KTL	201	223	0.077	16.0	1.1

AA6061

This alloy differs from AA6060 by its Mg, Si and Mn contents and is thereby able to attain higher strength. This is due to the fact that the amount of Mg and Si are essential in order to form hardening β''- Mg_5Si_6 particles during the ageing process, or alternatively, GP zones during room temperature storing [10].

The experimental results are presented in Figure 3.7 and Table 3.6. The results are in accordance with what is observed and discussed for the AA6060 material.

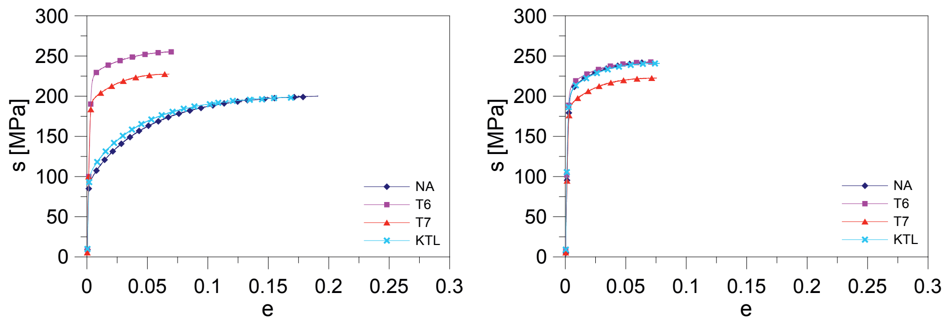

(a) Initial T4 (b) Initial T6

Figure 3.7: Uniaxial tensile test results of AA6061, label indicates PWHT scheme

Table 3.6: Effect of PWHT schemes on AA6061 – characteristic measures

Condition	PWHT and label	$s_{0.2}$ [MPa]	s_u [MPa]	e_u [mm/mm]	D	$\frac{P_u}{P_{0.2}}$
T4	NA	97	200	0.191	57.0	2.1
	T6	225	255	0.071	12.5	1.1
	T7	195	228	0.068	13.5	1.2
	KTL	107	199	0.169	44.6	1.9
T6	NA	206	243	0.072	13.9	1.2
	T6	211	243	0.073	15.5	1.2
	T7	189	223	0.076	15.3	1.2
	KTL	204	241	0.078	17.3	1.2

AA6005

This alloy differs from the AA6060 alloys only in Cu and Mn contents, but the Mg and Si contents that play a vital role in 6xxx series are more or less the same. Thus, the behaviour and results are expected to be comparable to what has been discussed for the AA6060 (and AA6061) alloy. The results of the planned test programme of uniaxial tensile tests are compiled in Figure 3.8 a) and b) for initial condition T4 and T6, respectively, while Table 3.7 presents the characteristic strength and ductility measures.

For the T4 condition, the effect of PWHT is comparable to the other alloys, but the results for the T6 condition came out as a surprise. As seen, this material responds strongly to both KTL and T6 heat treatment, and has also strength much lower to what is obtained by T6 PWHT scheme on the T4 conditioned material. Hence, it was suspected that something had gone wrong during the production of the plate material and caused a low yield stress of the as-delivered T6 (169 MPa). To conclude on this it was decided to carry out additional tensile tests on the remaining of the plate material, with objective to identify the actual T6 strength of the material. To this means, two (solution heat treatment at 520 °C for 30 minutes, rapidly cooled by water quenching, and left at room temperature for at least 4 hours and artificially aged at 175 °C for 10h). The results of one of these tests are presented along with the original results in Figure 3.8 (c). As seen the actual T6 strength is much higher than the as-delivered 'T6' material. It is concluded that the original plates had a too low yield stress probably due to slow cooling (air cooling) after solution heat treatment. *These data must be used with care in further validation studies since the actual thermal processing of the as-delivered material is uncertain.*

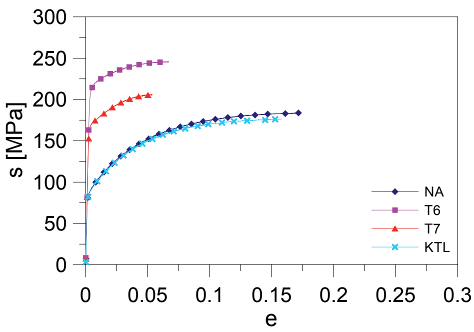

(a) Initial T4

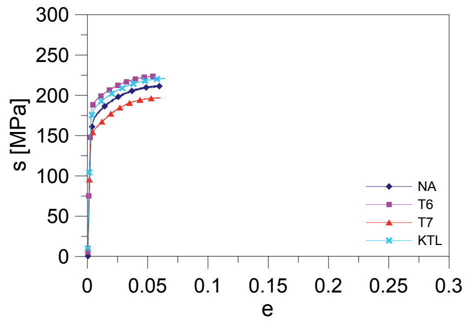

(b) Initial T6

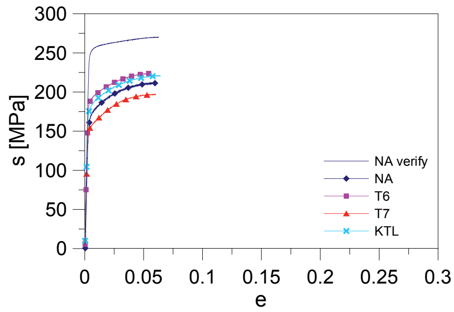

(c) Initial T6 – Verifying test

Figure 3.8: Uniaxial tensile test results of AA6005, label indicates PWHT scheme

Table 3.7: Effect of PWHT schemes on AA6005 – characteristic measures

Condition	PWHT and label	$s_{0.2}$ [MPa]	s_u [MPa]	e_u [mm/mm]	D	$\frac{P_u}{P_{0.2}}$
T4	NA	88	184	0.172	59.0	2.1
	T6	215	246	0.067	11.9	1.1
	T7	170	206	0.054	11.4	1.2
	KTL	89	176	0.158	44.0	2.0
T6	NA	172	212	0.060	9.0	1.2
	T6	189	224	0.057	11.5	1.2
	T7	155	197	0.060	13.3	1.3
	KTL	180	221	0.064	13.9	1.2

AA7046

Figure 3.9 present the results from the uniaxial tensile tests on the AA7046 alloy, while Table 3.8 summarises the characteristic strength and ductility measures. Note that in initial condition T4, the NA PWHT scheme gives strong work hardening and results in the highest ultimate strength. The failure of this specimen seems not to be due to diffuse necking, but an abrupt though-thickness shear failure. The observations are further in line with precipitation theory, i.e. the T6 PWHT scheme leads to higher yield strength and reduced work hardening for the material in initial condition T4, whereas over-ageing (T7) lowers the strength. For initial condition T6, the as-delivered material shows the highest strength, i.e. all the PWHT schemes cause a reduction in strength. Note the much stronger effect of the KTL PWHT scheme as compared to what was observed for the AA6xxx alloys presented above.

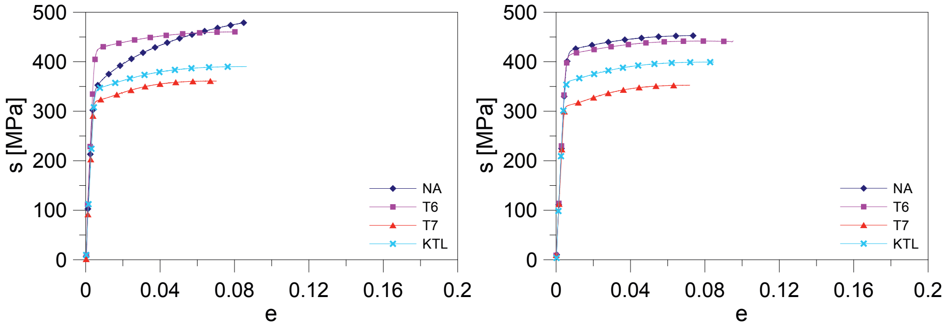

(a) Initial T4 (b) Initial T6

Figure 3.9: Uniaxial tensile test results of AA7046, label indicates PWHT scheme

Table 3.8: Effect of PWHT schemes on AA7046 – characteristic measures

Condition	PWHT and label	$s_{0.2}$ [MPa]	s_{ult} [MPa]	e_u [mm/mm]	D	$\frac{P_u}{P_{0.2}}$
T4	NA	351	479	0.085	13.3	1.4
	T6	424	460	0.081	12.2	1.1
	T7	321	361	0.070	10.5	1.1
	KTL	345	390	0.087	12.2	1.1
T6	NA	420	453	0.081	9.1	1.1
	T6	413	442	0.102	12.1	1.1
	T7	311	353	0.072	10.4	1.1
	KTL	359	400	0.085	12.1	1.1

AA7108

The response curves for both initial tempers and all PWHTs are depicted in Figure 3.10, while characteristic strength and ductility measures are given in Table 3.9. The general trends are comparable to what was observed for AA7046. The failure of the 'NA' specimen for the as-delivered T4 material is again due to a shear fracture, but for this material this failure mechanism was also observed for some specimens in as-delivered T6 condition ('NA' and 'T7' PWHT schemes). The modelling of this mechanism is beyond the scope of the present work, but it is emphasized that the ductility of the different material tests are limited by two different phenomena (instability and localised necking), and that proper models for the ductility of AA7xxx materials must also invoke attention to the phenomenon of through-thickness shear fracture. For this reason the experimental data related to the ductility must be used with care in further validation studies.

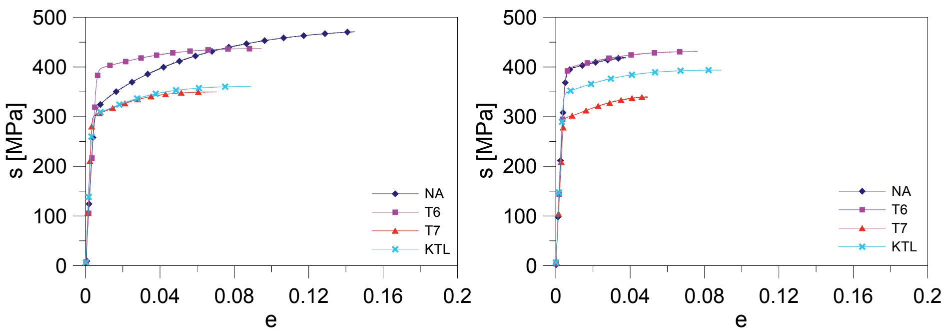

(a) Initial T4 (b) Initial T6

Figure 3.10: Uniaxial tensile test results of AA7108, label indicates PWHT scheme

Table 3.9: Effect of PWHT schemes on AA7108 – characteristic measures

Condition	PWHT and label	$s_{0.2}$ [MPa]	s_{ult} [MPa]	e_u [mm/mm]	D	$\frac{P_u}{P_{0.2}}$
T4	NA	319	471	0.145	22.2	1.5
	T6	397	437	0.094	10.8	1.1
	T7	304	350	0.070	12.1	1.2
	KTL	306	361	0.089	14.9	1.2
T6	NA	392	419	0.037	4.7	1.1
	T6	397	431	0.076	10.7	1.1
	T7	299	340	0.049	7.1	1.1
	KTL	349	394	0.089	13.8	1.1

3.6 Hardness tests – HAZ extent and properties

The combination of WELDSIM and NaMo model provides information about the yield stress and hardening at any point in a welded structure. However, the accuracy of this model concept must be verified by experimental data. As there are no practical methods for direct experimental determination of the yield stress close to the weld, this was done implicitly by means of hardness measurement and correlation formulas.

Hardness is a measure of a metal's resistance to localized plastic deformation. In hardness testing, a small indenter is forced into the surface of the material under controlled conditions of load and rate of indentation. The depth or size of the resulting indent is measured, which in turn is related to a hardness number; the softer the material, the larger and deeper the indent, and the lower the hardness index number. It should be noted that the hardness may be measured by various test methods, and it is not an intrinsic material property. Thus, every test result has a label identifying the test method used. In this programme, the standard Vickers Hardness (HV) test method was used [37].

3.6.1 Test procedure

A total of 40 hardness test were carried out. Four specimens with different PWHT from each alloy and initial condition were cast in epoxy in the same mould. The mould with the four specimens and the polished specimens ready to be tested are shown in Figure 3.11 (a) and (b) respectively. The locations of the test points are shown in Figure 3.12. The specimens were 25 mm long, 10 mm wide and 3 mm thick. It can be seen that the specimens extended about 25 mm from the weld centre line. After 8 hours of hardening in the mould, the specimens were grinded, washed and polished, using sand papers with grain size 800, 1200 and 2400. A LEICA VMHT MOT test machine and 1 kg load was used for the indentation.

(a)

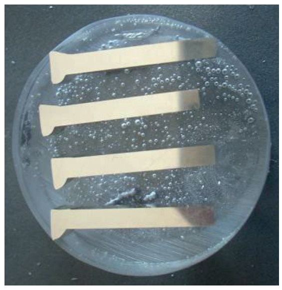

(b)

Figure 3.11: (a) Hardness specimens in mould and (b) Polished specimens in mould

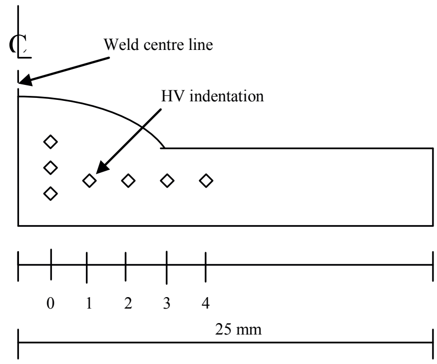

Figure 3.12: Location of test points

Anodizing

Anodizing was carried out to identify the boundary of weld metal and base material (fusion line), and the location of the indentation points relative to this boundary. Figure 3.13 and Figure 3.14 illustrate some of the results. Based on this information, indentation data from the weld were disregarded since these are dependent upon among other parameters the choice of filler material. In what follows, the hardness profiles are based on indentation data starting from the fusion line.

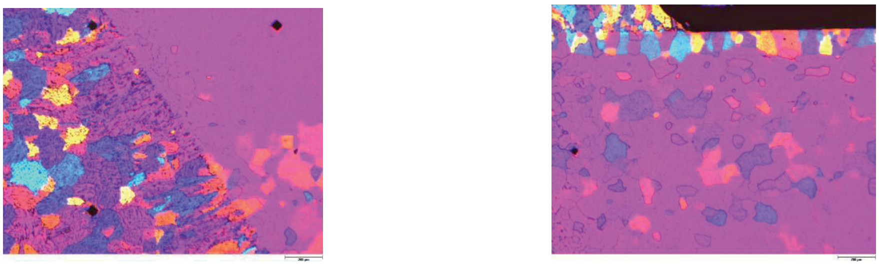

(a) 1st indent data and 2nd indent (b) top edge of specimen

Figure 3.13: Anodizing of hardness specimens AA6060, initial T4 following PWHT-T7

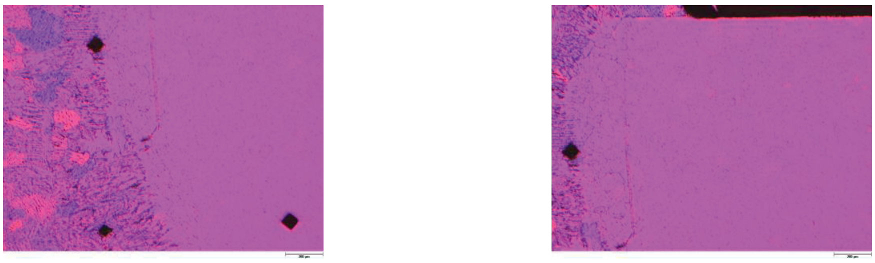

(a) 1st indent data and 2nd indent (b) top edge of specimen

Figure 3.14: Anodizing of hardness specimens AA6060, initial T4 following NA

3.6.2 Test results

AA6060

Figure 3.15 a) and b) shows the hardness profiles determined for the AA6060 weldments in initial condition T4 and T6, respectively where the abscissa represents the distance from the fusion line.

For initial temper T4, the hardness seems to be almost constant for each of the four PWHT schemes. In other words, the hardness measurements indicates that there are only limited traces of the welding process with almost no weakening of the HAZ for this initial condition.

From the hardness profiles for the materials welded in initial T6 condition, a clearly weakened HAZ with an extent of approximately 8 mm is seen for the NA and KTL PWHT schemes. For the T6 PWHT scheme the hardness of the HAZ seems to be fully recovered, but then again a slightly weakened HAZ appears to be present for the T7 PWHT scheme.

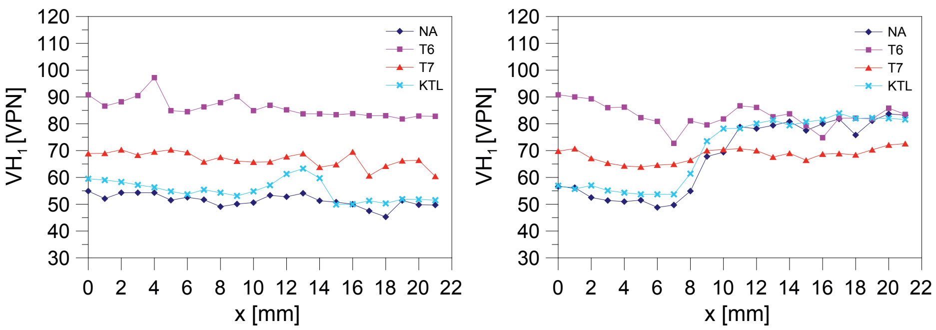

(a) Initial T4 (b) Initial T6

Figure 3.15: Hardness test results of AA6060, after NA and PWHT

AA6061

Figure 3.16 depicts the hardness profiles for AA6061. For initial temper T4, shown in part a) of the figure, all PWHTs actually increase the hardness in the HAZ. All artificial PWHT schemes give higher hardness than NA.

For initial temper T6, the T6 PWHT scheme gives peak hardness next to the weld. The hardness decreases gradually from the fusion line and reaches a minimum for x = 4 mm – 6 mm. The results for the three other PWHTs show an approximately 8 mm wide zone with reduced hardness.

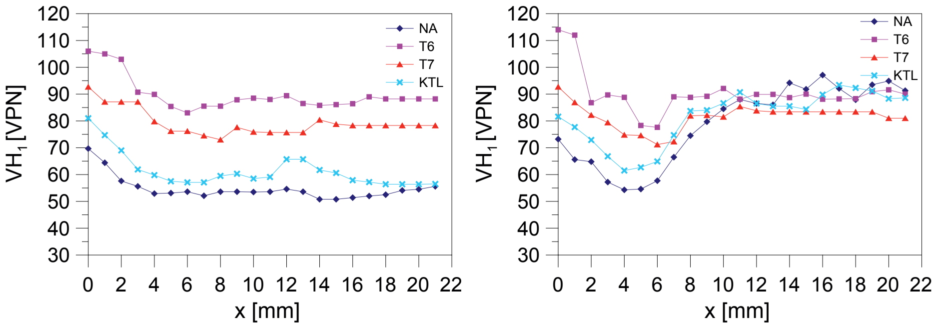

(a) Initial T4 (b) Initial T6

Figure 3.16: Hardness test results of AA6061, after NA and PWHT

AA6005

Figure 3.17 a) and b) show the hardness profiles for initial tempers T4 and T6, respectively. For initial condition T4, the profiles are similar in shape, except for a narrow zone of 3-4 mm width next to the weld showing higher hardness as compared to the rest of the measured region.

In initial T6 temper, the NA and KTL PWHT schemes, a HAZ extending about 10 mm from the fusion line is observed. The T6 and T7 PWHT schemes are able to recover the hardness close to the fusion line, but shows some variation, with a local minimum at about 5 mm distance from the fusion line.

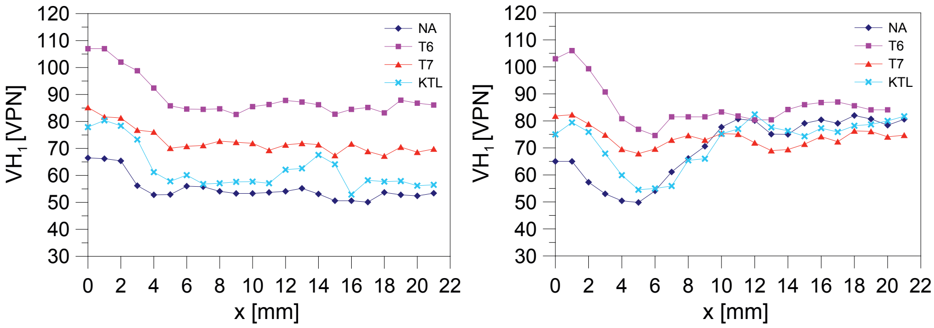

(a) Initial T4 (b) Initial T6

Figure 3.17: Hardness test results of AA6005, after NA and PWHT

AA7046

The measured HAZ hardness profiles for alloy AA7046 are shown in Figure 3.18. In general, the 7xxx series have higher strength and hardness compared to the 6xxx series, which is recognised in generally higher hardness.

For initial condition T4, the hardness in the HAZ seems to be comparable to, or higher, than the hardness outside the HAZ. For initial condition T6, a weakly softened HAZ seems present for the NA and KTL PWHT schemes, with minimum hardness at about 10 mm away from the fusion line. The softening is much less prominent as compared to what was observed for the AA6xxx alloys.

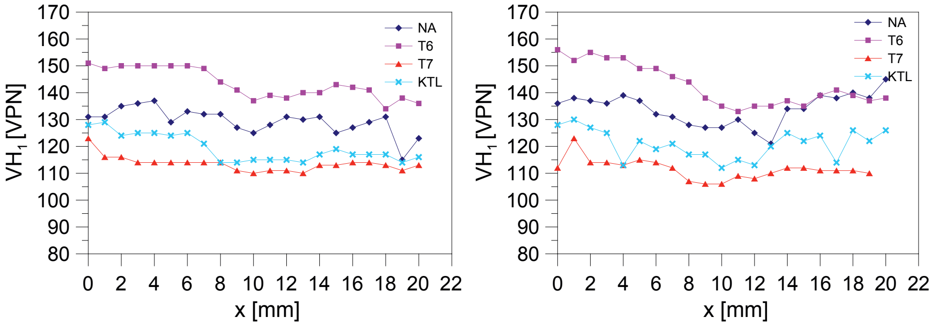

(a) Initial T4 (b) Initial T6

Figure 3.18: Hardness test results of AA7046, after NA and PWHT

AA7108

As seen in Figure 3.19, the hardness profiles for AA7108 shows an almost uniform hardness reduction when moving away from the weld for initial condition T4. This falling tendency is broken by distinct dips at a distance of about 10 mm for NA and PWHT-T6. Considering the uniformity of the remaining measurements this could have been attributed to experimental errors. However, as will be discussed later, the failure positions of the cross-weld tensile tests (in Figure 3.33) support the hardness measurements in the sense that the corresponding tests failed in this position.

For initial condition T6, the hardness is rather uniform, but a weakened HAZ extending up to 14 mm is recognised for NA, KTL and T6 PWHT schemes.

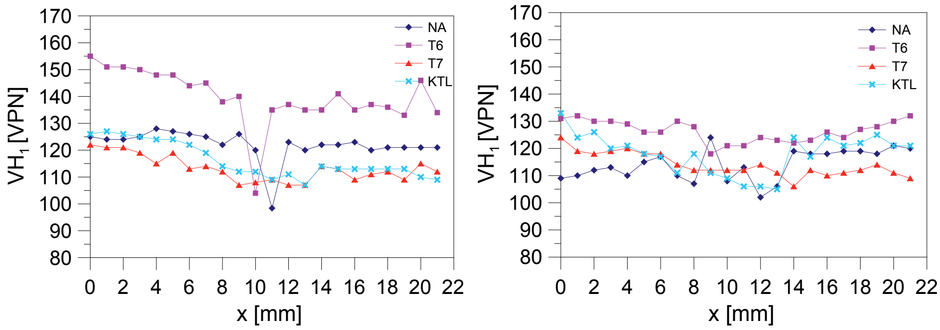

(a) Initial T4 (b) Initial T6

Figure 3.19: Hardness test results of AA7108, after NA and PWHT

3.7 Cross-weld tensile tests – generic joints

3.7.1 Test procedure

The cross-weld tensile test programme covers the same numbers of materials/conditions as the uniaxial tensile test programme, also with 2 duplicate tests, i.e. ending up with 80 cross-weld tensile tests, also.

The tests were carried out at room temperature in a hydraulic Instron test machine with a 250 kN load cell. The geometry of these specimens is provided in Figure 3.20, where the weld is positioned perpendicular to the longitudinal axis of the specimen in the middle of the gauge section. The specimens were clamped by hydraulic grips i.e., not using clevis arrangements. The tests were performed under displacement control with crosshead displacement rate of 5 mm/min. The deformation in the centre region of the specimen was measured using an extensometer with 50 mm gauge length and a Canon EOS 1D camera was used for strain field determination using Digital Image Correlation (DIC; see Figure 3.21 a).

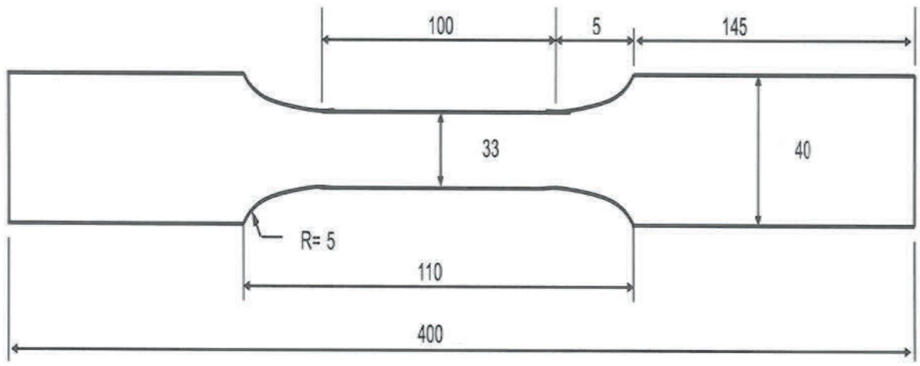

Figure 3.20: Tensile test specimen dimensions [14]

The DIC technique provides displacement and strain fields during the test. The lens of the camera was positioned at the same vertical position as the centre of the specimen, at a distance of 300 mm from the specimen surface, Figure 3.21 b). A pattern on the specimen surface is required to determine the displacement and strain fields from images using the DIC technique. The pattern was created before testing by paint sprays. The specimen surface was first sprayed with black paint followed with white paint in order to create random speckles on the surface. A specimen to be tested with single-camera DIC must be flat. Thus irregularities like welds must be grinded down. As the name suggests, DIC involves comparing successive digital images to determine the relative displacement of surface features between ‘undeformed’ and ‘deformed’ images. The DIC is superior to the traditional extensometer because it measures the surface strain field instead of the average strain over a gauge length. Thus, it is useful when dealing with heterogeneous strain distributions as well as to determine the local strains in necked regions.

The principle of this technique is further illustrated in Figure 3.22, which is adopted from reference [43]. Note that this reference gives detail of the technique. The figure shows that the material points are compared between a reference image and a deformed image, and from which a computer program is used to calculate the deformation of the sample. Figure 3.23 shows an example of the measured deformation in a cross-weld tensile test (AA6060-T6, T7 PWHT scheme) as obtained with DIC.

a)

b)

Figure 3.21: Test set up including a) extensometer and b) camera for image acquisition

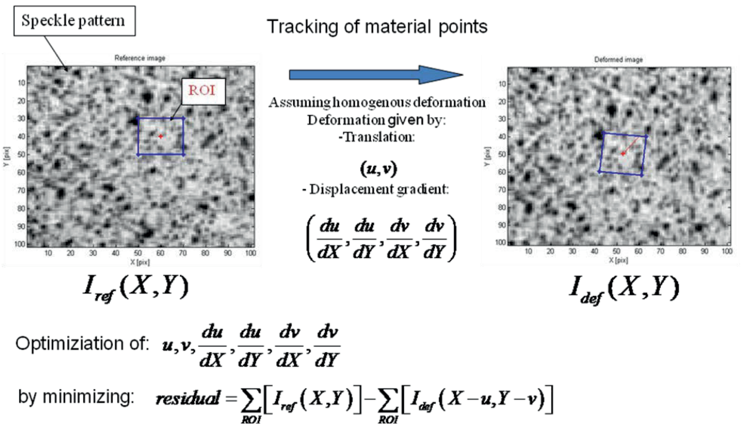

Figure 3.22: Principles of Digital Image Correlation (DIC) Technique [43]

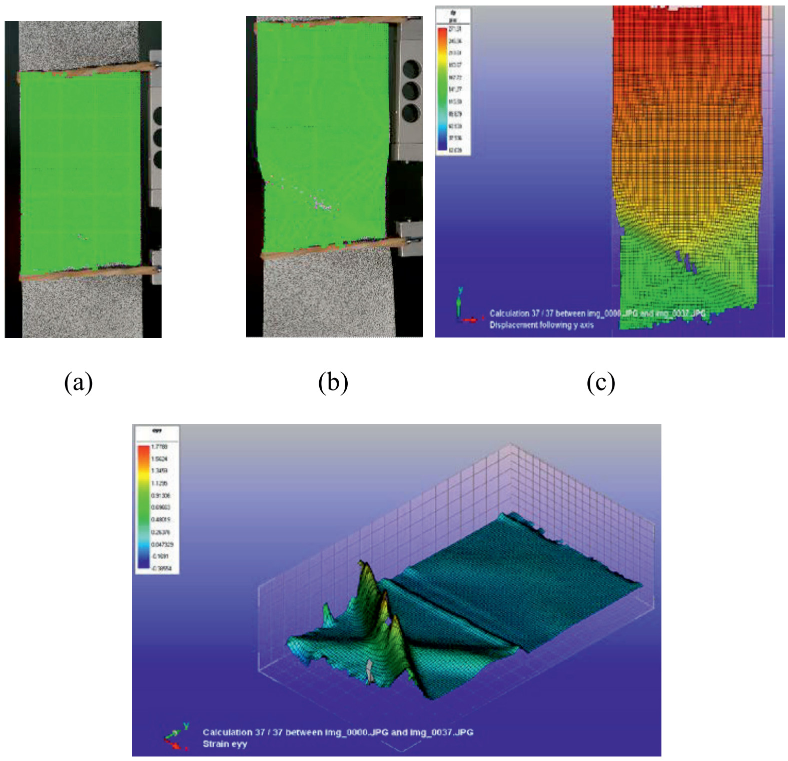

(a) (b) (c)

(d)

Figure 3.23: Deformations measured using DIC, (a) initial grids on image, (b) final grids on image and (c) and (d,) displacement and strain along longitudinal axis of specimen, respectively.

3.7.2 Test results

The test results are presented in the same format as the uniaxial tensile tests data, i.e. in the form of engineering stress vs. engineering strain curves $(s-e)$, plotted up to the maximum force. For the present tests, the curves must be considered as normalised force vs. displacement curves since they represent the response of an inhomogeneous test specimen. The engineering strain is calculated from the DIC measurements using a gauge length of 50 mm. Engineering stress vs. *crosshead* displacements curves are placed in Appendix 1 – 5 for further reference. Also provided in Appendix 6 – 15 are comparisons between $(s-e)$ curves obtained using the DIC technique and by the extensometer measurements. There are only small deviations between the two, showing that DIC is a valid method. Note further that the experimental results are compiled in Figure 3.35 through Figure 3.39 for the five investigated materials. *Some of the effects discussed in the following are most easily observed in the latter figures.*

AA6060

Figure 3.24, a) and b) show engineering stress-strain curves from the cross-weld tensile tests of alloy AA6060, welded in initial condition T4 and T6, respectively. The results for the material welded in initial condition T4 is comparable to the base material response as discussed in Section 3.5.2 (most easily seen in Figure 3.35). However, the elongation of the welded coupons is generally somewhat lower than what was observed for the base materials. This is in accordance with the hardness measurements and shows that the welding and PWHT schemes result in rather homogeneous properties in the test coupons, i.e. with weak effects of the weldment and HAZs.

For the material in initial condition T6 the welding is detrimental to the strength of the cross-weld tensile tests as compared with the base material properties. This is due to dissolution of the strengthening precipitates in the HAZ as discussed in Section 2.2. The ultimate capacity of these tests is expected to be governed by weakest section of the HAZ. As expected it is seen to correlates well with the hardness measurements as presented in Figure 3.15 b). The T6 and T7 PWHT scheme brings properties (strength and elongation) comparable to the ones of the base material test coupons, while the KTL scheme is insufficient to regain the strength capacity.

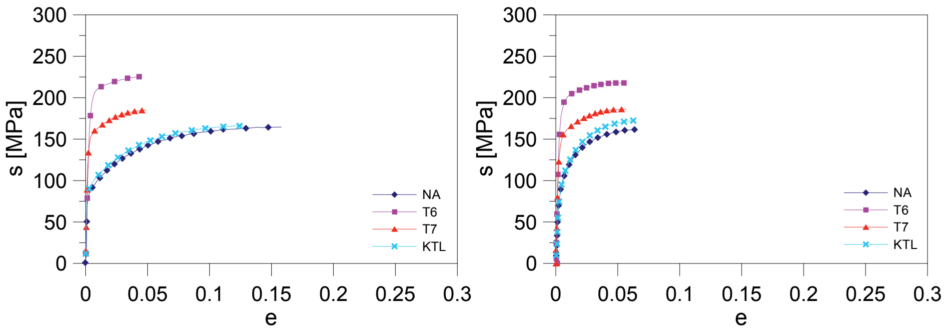

(a) Initial T4 (b) Initial T6

Figure 3.24: Cross-weld tensile test results of AA6060, after NA and PWHT

Table 3.10: Compilation and comparison of results from cross-weld tensile tests (CWTT) and uniaxial tensile tests (UTT) of AA6060

Condition	PWHT and label	s_{ult} [MPa]		e_u [mm/mm]		D		$\frac{P_u}{P_{0.2}}$	
		CWTT	UTT	CWTT	UTT	CWTT	UTT	CWTT	UTT
T4	NA	165	175	0.158	0.221	39.9	64.7	1.9	2.1
	T6	226	234	0.045	0.080	7.3	13.4	1.1	1.1
	T7	185	193	0.049	0.064	10.8	12.2	1.2	1.2
	KTL	166	166	0.126	0.206	39.4	62.0	1.8	2.0
T6	NA	122	223	0.064	0.075	11.5	14.6	1.7	1.1
	T6	218	224	0.052	0.068	10.2	14.3	1.2	1.1
	T7	186	196	0.057	0.069	11.0	15.3	1.3	1.2
	KTL	172	223	0.063	0.077	10.3	16.0	1.7	1.1

The ductility of the different specimens is discussed in view of Figure 3.25 showing the failure mode of all specimens and Table 3.10. The failure modes can also be understood and correlated to the hardness profiles presented above. For initial temper T4 the hardness shows a slightly falling tendency away from the fusion line without any distinct minimum for all PWHTs. For this reason, plasticity is not localized in the HAZ, and the ultimate failure occurs in the base material. For initial temper T6 a clearly weakened HAZ was observed for the NA and KTL PWHT schemes, and these specimens fail in the HAZ. For the T6 and T7 PWHT schemes the hardness profile showed no clear minimum, and failure occurs in the form of a localised neck, in principle, positioned outside the HAZ.

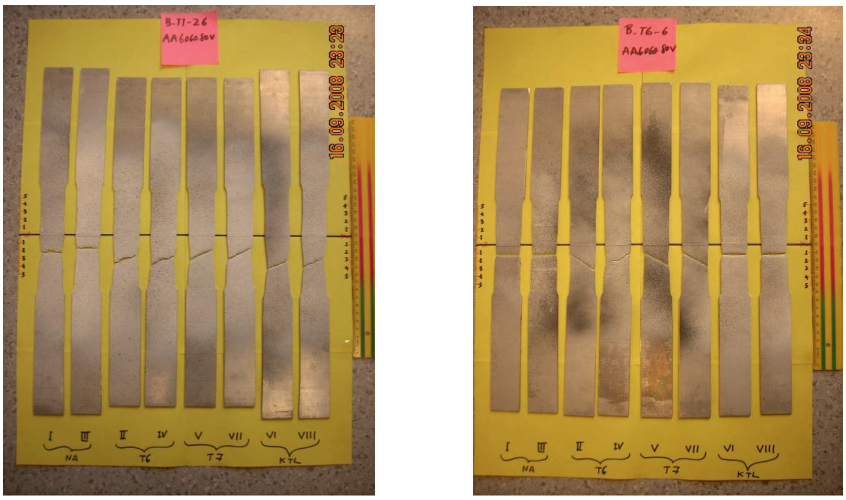

(a) initial T4 (b) initial T6

Figure 3.25: Failure pattern of tensile test results AA6060, after NA and PWHT

AA6061

Figure 3.26 and Table 3.11 show that $s_{0.2}$ and s_{ult} for AA6061 are larger than the corresponding values for the previous 6xxx alloy, both with respect to tempers and PWHTs. This is due to the higher magnesium content in AA6061. Welding causes a reduction in the s_{ult} for both T4 and T6 for all PWHTs, except for T7 PWHT scheme. It may also be noted that for KTL PWHT scheme the strain at ultimate stress is smaller than NA in T4. As for the previous alloy, the ultimate strain is significantly reduced for T6. And it is observed that welding has little influence on the work hardening, except for NA and KTL PWHT scheme in initial temper T6.

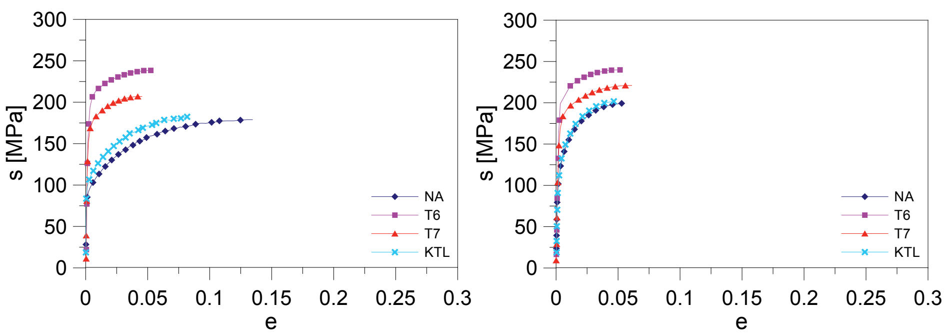

(a) Initial T4 (b) Initial T6

Figure 3.26: Cross-weld tensile test results of AA6061, after NA and PWHT

Table 3.11: Compilation and comparison of results from cross-weld tensile tests (CWTT) and uniaxial tensile tests (UTT) of AA6061

Condition	PWHT and label	s_{ult} [MPa]		e_u [mm/mm]		D		$\frac{P_u}{P_{0.2}}$	
		CWTT	UTT	CWTT	UTT	CWTT	UTT	CWTT	UTT
T4	NA	179	200	0.130	0.191	44.9	57.0	1.9	2.1
	T6	238	255	0.050	0.071	11.3	12.5	1.2	1.1
	T7	207	228	0.045	0.068	10.5	13.5	1.2	1.2
	KTL	183	199	0.082	0.169	30.3	44.6	1.7	1.9
T6	NA	199	243	0.053	0.072	14.8	13.9	1.7	1.2
	T6	240	243	0.052	0.073	9.5	15.5	1.1	1.2
	T7	221	223	0.061	0.076	12.1	15.3	1.2	1.2
	KTL	202	241	0.047	0.078	11.7	17.3	1.6	1.2

The changes in the ductility can be explained by the failure locations, as given by the photos in Figure 3.27 and by the hardness profiles presented in Figure 3.16. Except for a narrow zone with high hardness in narrow zone next to the fusion line, the hardness is almost constant for all PWHTs in temper T4. Failure may therefore be initiated at any point in the base material, which is also what happened. For T6 all profiles have a distinct minimum about 5 mm from the fusion line, and as shown in Figure 3.27 all failures, with one exception, occurred in the HAZ.

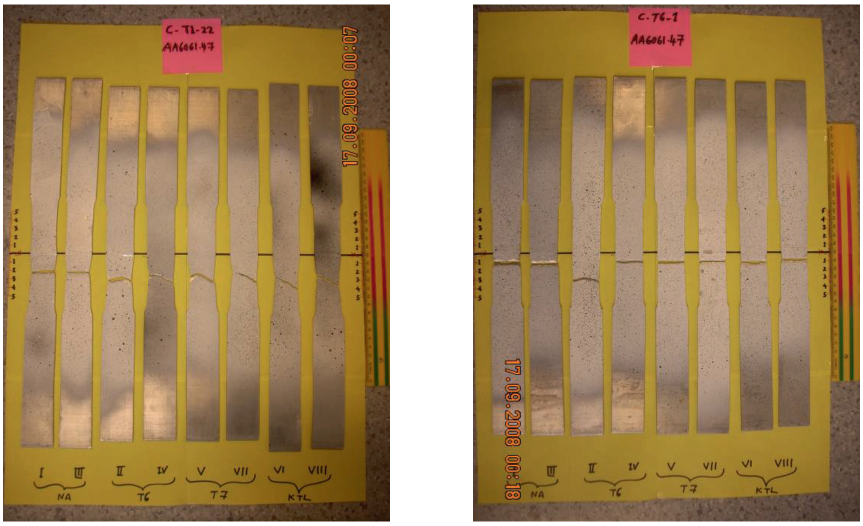

(a) initial T4 (b) initial T6

Figure 3.27: Failure pattern of tensile test results AA6061, after NA and PWHT

AA6005

Figure 3.18 (a) and (b) show engineering stress-strain curves from the cross-weld tensile tests of alloy AA6005, welded in initial condition T4 and T6, respectively. The following observations are made for the NA and KTL PWHT schemes, which results in very similar response curves for both initial conditions: 1) The s_{ult} is slightly larger when welding is done in T6 condition, and 2) the specimen elongation is larger when welding is done in T4 condition.

The T6 and T7 PWHT schemes result in enhanced strength for both initial conditions. For the tests based on initial condition T6, also the specimen ductility is increased by these PWHT schemes. In other words, the effects are entirely positive with respect to the mechanical properties of the component (specimen). For the tests in initial condition T4, these PWHT schemes reduce the specimen elongation, similarly to what is experienced for the base material.

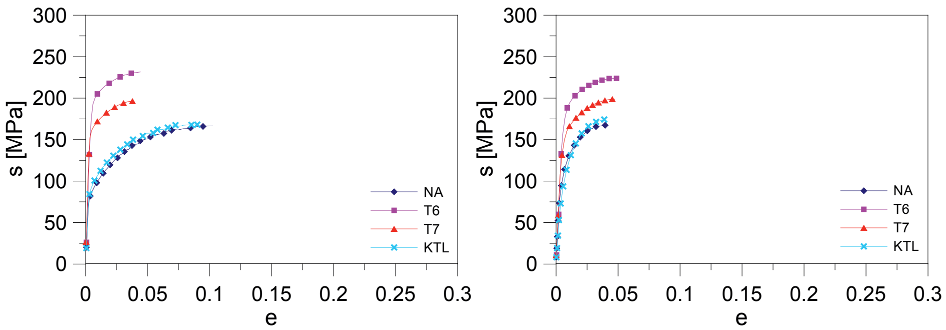

(a) Initial T4 (b) Initial T6

Figure 3.28: Cross-weld tensile test results of AA6005, after NA and PWHT

Table 3.12 summarizes the mechanical parameters for the cross-weld tensile tests and the uniaxial tensile tests presented in Section 3.5.2. For T4 welding causes a reduction in the s_{ult} for all PWHTs, with the maximum reduction for NA. For T6 reductions are observed for NA and KTL PWHT scheme, while there are no strength reductions for the other PWHTs. From the ratio $P_u/P_{0.2}$ it is seen that welding does not affect the work hardening in initial T4, but it causes a reduction for NA and PWHT-KTL in initial T6.

Table 3.12: Compilation and comparison of results from cross-weld tensile tests (CWTT) and uniaxial tensile tests (UTT) of AA6005

Condition	PWHT and label	s_{ult} [MPa]		e_u [mm/mm]		D		$\frac{P_u}{P_{0.2}}$	
		CWTT	UTT	CWTT	UTT	CWTT	UTT	CWTT	UTT
T4	NA	167	184	0.102	0.172	21.0	59.0	2.0	2.1
	T6	232	246	0.044	0.067	5.7	11.9	1.2	1.1
	T7	197	206	0.039	0.054	7.0	11.4	1.2	1.2
	KTL	169	176	0.091	0.158	18.2	44.0	1.8	2.0
T6	NA	167	212	0.040	0.060	7.0	9.0	1.7	1.2
	T6	224	224	0.049	0.057	5.1	11.5	1.2	1.2
	T7	199	197	0.045	0.060	6.1	13.3	1.4	1.3
	KTL	175	221	0.039	0.064	5.1	13.9	1.8	1.2

Figure 3.29 shows pictures of the failed specimens for the two different initial conditions. For initial temper T4 the specimens failed outside the HAZ for all PWHTs. This could be expected as it is known that welding in temper T4 gives little reduction of the yield stress in HAZ. This is substantiated by the hardness measurements given in Section 3.7. As will be seen, the hardness measurements reveal that a 3-4 mm wide zone next to the weld has higher hardness than the rest of the specimen, which demonstrate a uniform hardness profile. Naturally, failure initiates at a point within the weaker region.

Welding in T6 is known to strongly reduce the strength in the HAZ. The NA and KTL PWHT schemes do not remedy this strength drop. Thus, failure occurs in the HAZ for these PWHT schemes. For the T6 and T7 PWHT schemes, hardness profiles demonstrate that the loss of strength in the HAZ is regained by the heat treatment. In other words, the specimens have almost constant hardness (strength) along the gauge section. This caused the failure to occur in the base material, except for specimen VII that failed in the HAZ. Note: for T7 PWHT, the response curve, results from specimen V that failed outside of the HAZ.

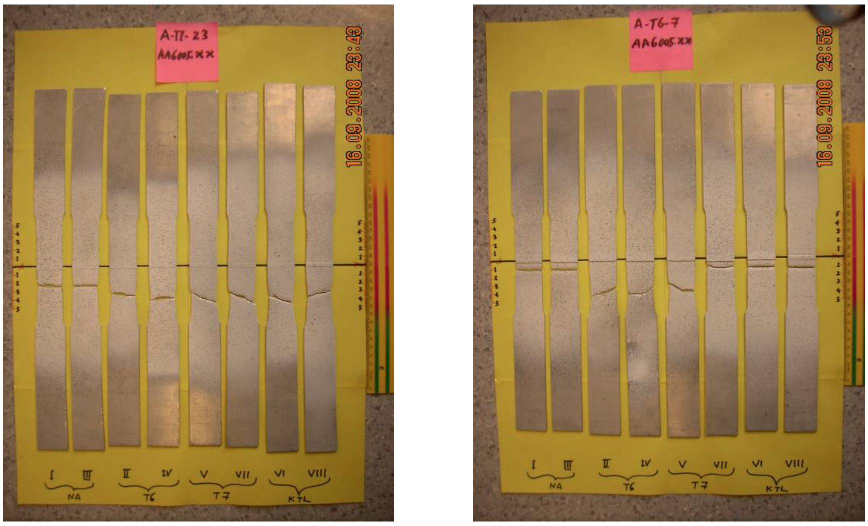

(a) initial T4 (b) initial T6

Figure 3.29: Failure pattern of tensile test results AA6005, after NA and PWHT

AA7046

Figure 3.30 and Table 3.13 present the results for alloy AA7046. Again, the initial temper has little effect on the tensile strength and the amount of strain hardening. The T7 PWHT scheme clearly reduces the strength, while NA gives higher strength than observed for 6xxx alloys. Note that for both initial tempers the s_{ult} for NA is reached while the response curves still have a positive gradient, which is caused by rapid growth of GP zones at room temperature. Welding causes in general an approximate 5% reductions in $s_{ult,}$ except for NA where the reduction is 14%.

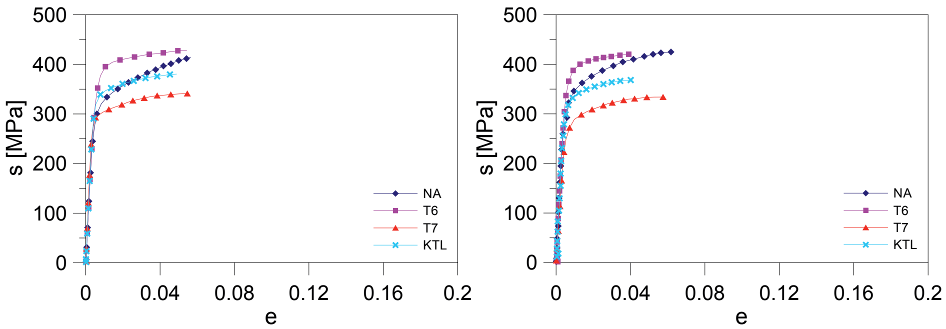

(a) Initial T4 (b) Initial T6

Figure 3.30: Cross-weld tensile test results of AA7046, after NA and PWHT

Table 3.13: Compilation and comparison of results from cross-weld tensile tests (CWTT) and uniaxial tensile tests (UTT) of AA7046

Condition	PWHT and label	s_{ult} [MPa]		e_u [mm/mm]		D		$\frac{P_u}{P_{0.2}}$	
		CWTT	UTT	CWTT	UTT	CWTT	UTT	CWTT	UTT
T4	NA	414	479	0.056	0.085	7.6	13.3	1.4	1.4
	T6	428	460	0.054	0.081	6.3	12.2	1.2	1.1
	T7	341	361	0.055	0.070	8.8	10.5	1.2	1.1
	KTL	380	390	0.049	0.087	6.5	12.2	1.2	1.1
T6	NA	425	453	0.062	0.081	9.6	9.1	1.5	1.1
	T6	420	442	0.039	0.102	4.7	12.1	1.1	1.1
	T7	334	353	0.057	0.072	7.3	10.4	1.2	1.1
	KTL	368	400	0.040	0.085	5.2	12.1	1.2	1.1

Figure 3.31 shows that for T4 the failure occurred at a distance of about 10 mm from the fusion line for NA and T6 PWHT schemes and at a distance of about 20 mm for T7 and KTL PWHT schemes. This is in agreement with the location of the minimum hardness as seen from the profiles in Figure 3.18. For T6 the location was inconsistent and occurred at either 10 mm or 20 mm for each PWHT. The hardness profiles do not indicate preference for either location.

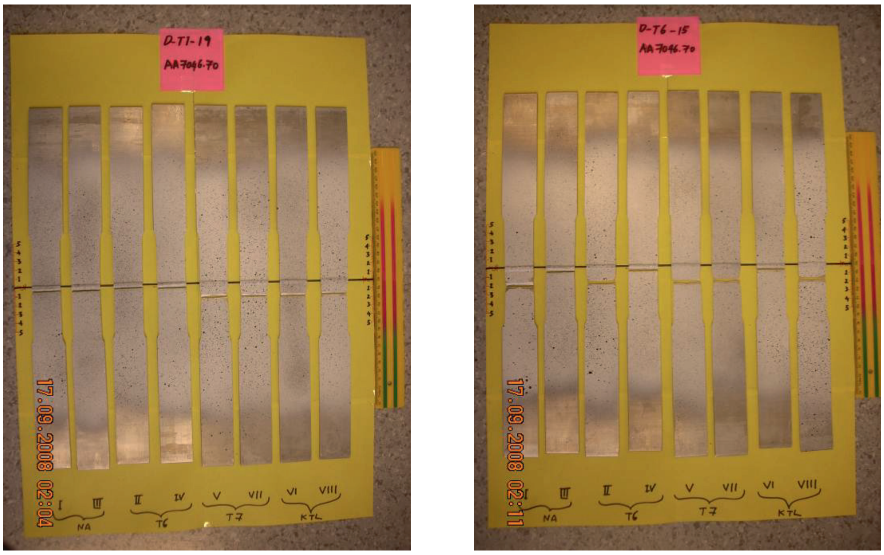

(a) initial T4 (b) initial T6

Figure 3.31: Failure pattern of tensile test results AA7046, after NA and PWHT

AA7108

The response data for AA7108 are presented in Figure 3.32 and Table 3.14, and as seen the results differ little from those of AA7046. The welding causes a reduction in s_{ult} of about 5%, independent of the initial temper, and again the highest value is obtained for NA. Also here the T7 PWHT scheme gives the lowest strength. Due to the experimental problems no data are available for KTL PWHT scheme in T4. The ductility *D* for NA and T7 PWHT schemes in T6 are anomalous, as welding appears to improve the ductility significantly.

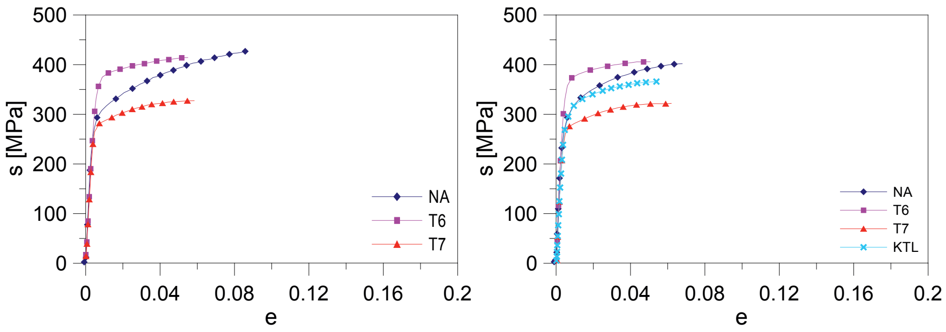

(a) Initial T4 (b) Initial T6

Figure 3.32: Cross-weld tensile test results of AA7108, after NA and PWHT

Table 3.14: Compilation and comparison of results from cross-weld tensile tests (CWTT) and uniaxial tensile tests (UTT) of AA7108

Condition	PWHT and label	s_{ult} [MPa]		e_u [mm/mm]		D		$\frac{P_u}{P_{0.2}}$	
		CWTT	UTT	CWTT	UTT	CWTT	UTT	CWTT	UTT
T4	NA	427	471	0.086	0.145	14.6	22.2	1.5	1.5
	T6	414	437	0.055	0.094	6.6	10.8	1.2	1.1
	T7	327	350	0.058	0.070	8.3	12.1	1.2	1.2
	KTL	-	361	-	0.089	-	14.9	-	1.2
T6	NA	402	419	0.068	0.037	12.6	4.7	1.4	1.1
	T6	406	431	0.051	0.076	7.0	10.7	1.1	1.1
	T7	322	340	0.062	0.049	9.2	7.1	1.2	1.1
	KTL	366	394	0.054	0.089	7.3	13.8	1.2	1.1

As seen from Figure 3.33, failure for T4 occurs at the same locations as for AA7046, while there is less variation in the location for T6. Considering the hardness profiles in Figure 3.19, it is seen that the hardness decreases with increasing distance from the fusion line, except for distinct local dips for NA and T6 PWHT schemes for initial T4 at a distance of 10 mm. Initially this was thought to be due to a measurement error, but Figure 3.33 shows that this is where the failure actually occurred. For T6 the minimum hardness occurs at a distance of about 12 mm for all PWHTs, which is also where the specimens failed.

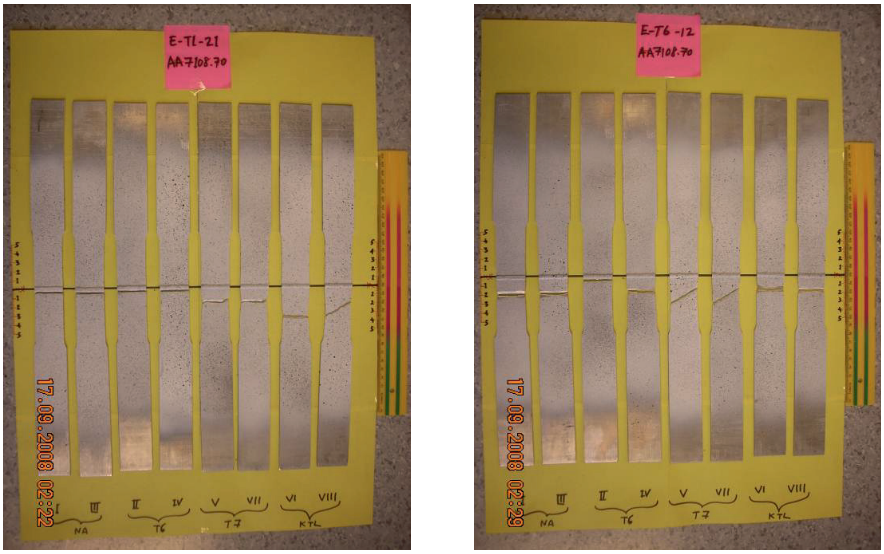

(a) initial T4 (b) initial T6

Figure 3.33: Failure pattern of tensile test results AA7108, after NA and PWHT

3.8 Discussion and concluding remarks

In the previous sub-sections of this chapter, the tests on the individual materials have been presented and discussed. Figure 3.35 to Figure 3.39 have been prepared to provide overview of all experimental results. The three tests methods, namely Uniaxial tensile tests, Cross-weld tensile tests and Hardness tests provide complimentary information about the material and how it is affected by temperature. The collected illustrations provide the means to explore the consistency of the results, and to analyse the systematic effects of alloy, initial condition, welding and PWHT on the strength and ductility of base materials and the generic welded joints. In addition, a column graph that summarizes the Yield stress (YS) and Ultimate Tensile Stress (UTS) of all alloys is further provided in Figure 3.40.

Uniaxial tensile test

The initial temper affects the tensile properties of the material significantly. For the as-delivered conditions (i.e. the NA), the yield stress is much lower in T4 than in the peak-aged T6 condition. The work hardening is, however, much larger and this leads to a more ductile specimen response.

For the AA6xxx alloys in the as-delivered T4 condition, the PWHT schemes generally increase the strength of the material at the cost of a reduced work hardening and reduced ductility. For 7xxx series in the as-delivered T4 condition, the strength increases only for the T6 PWHT scheme. Both KTL PWHT and over-ageing (T7 PWHT) lowers the strength. Here, NA gives the highest work hardening and ultimate strength.

For the materials delivered in initial condition T6, the PWHT schemes generally cause a reduction in strength for AA6xxx, except for AA6005-T6, due to improper temperature control during manufacturing. The deviating response of AA6005-T6 is seen by comparing Figure 3.37 (d) with the corresponding results for AA6060-T6 and AA6061-T6 (Figure 3.35 (d) and Figure 3.36 (d), respectively). The strength reduction is small for T6 PWHT and T7 PWHT for the (remaining) AA6xxx (-T6) alloys and AA7xxx (-T6) alloys. Only KTL PWHT scheme increases in strength for AA7xxx (-T6) alloys.

<u>Hardness tests</u>

The hardness profiles are much affected by the base metal chemistry and initial temper of the materials. A pronounced hardness reduction in the HAZ was observed for the AA6xxx alloys in temper T6. A less pronounced, but notable, hardness reduction is seen for the AA7xxx-T6 materials. In T4 conditions, no clear trends are observed. The PWHT schemes may effectively recover the strength loss in the HAZ for the investigated materials, but some *variations* in hardness prevail after welding and PWHT. The inhomogeneous properties may affect how and where strain localisation takes place in the cross-weld tensile tests.

From the hardness measurements it is possible to predict an approximate value of the yield stress using simple regression formulas reported in the literature. For Al-Mg-Si and Al-Zn-Mg extruded profiles, the following equations have been shown to give fair estimates of the yield stress [7, 46].

Al-Mg-Si: $$\sigma_{y\,0.2}(MPa) = 3.0HV - 48.1 \tag{3.4}$$

Al-Zn-Mg: $$\sigma_{y\,0.2}(MPa) = 3.7HV - 100.0 \tag{3.5}$$

The yield stress obtained from cross-weld tensile tests should be expected to give almost the same yield stress as estimated from the measured minimum HAZ hardness, which is confirmed by the good correlation shown in Figure 3.34. The small discrepancy observed, is probably due to the fact that the yield stress values from cross-weld tensile tests represent mean values over the specimen cross-sectional area, whereas the yield stress values from hardness measurement values are referring to a point within this area. It might be expected that the narrower the specimen tested, the better the correlation [18].

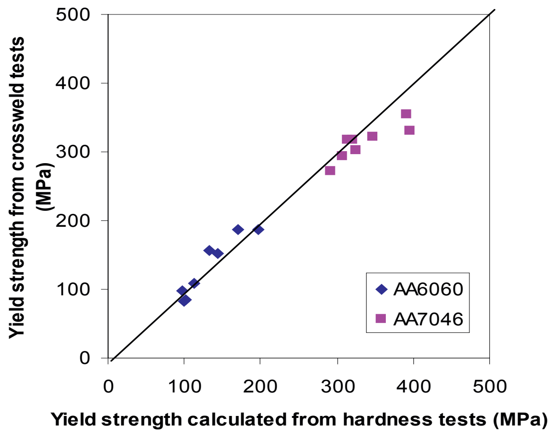

Figure 3.34: Correlation between minimum HAZ yield stress converted from hardness measurements, and measured yield stress in tensile testing of the HAZ normal to the welding direction for AA6060 and AA7046 [1].

<u>Cross-weld tensile tests:</u>

It is known that the strength of AA6xxx alloys in initial temper T4, which is not artificial aged, is relatively unaffected by welding. However, alloys in temper T6 have achieved their increased strength by artificial ageing, and subsequent welding will thus negate these beneficial effects.

This is confirmed by the response curves for the cross-weld tensile tests for initial temper T4. As seen, both f_y and f_u remain practically unchanged, while a reduction in the ductility is observed primarily for NA and KTL. For the other PWHTs the reduction is insignificant. These conclusions are substantiated by the hardness profiles which do not display a hardness drop that can be associated with a HAZ.

For alloys in initial temper T6 the hardness profiles show a significant drop in hardness in a region next to the weld for NA and KTL, indicating the presence of a HAZ. For the other PWHTs no such reduction is observed. These observations are substantiated by the response curves, which show a significant reduction in the ultimate limit strength for the NA and KTL-PWHT. On the other hand the ductility is relatively unaffected by the welds.

The hardness profiles for AA7046 and AA7108 show no drops in the vicinity of the weld, indicating that there are no HAZs, neither for initial T4 nor T6. Also for these alloys the welding has caused a small reduction in ductility (except of NA in initial T6).

AA6060	Uniaxial tensile test	Cross-weld tensile test	Hardness test
Initial T4	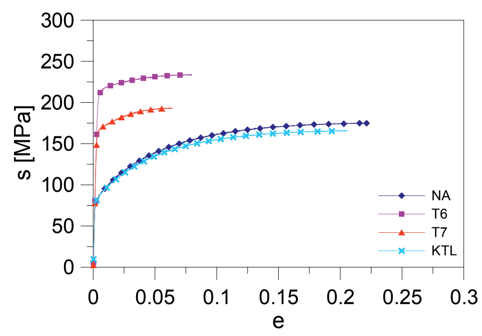 (a)	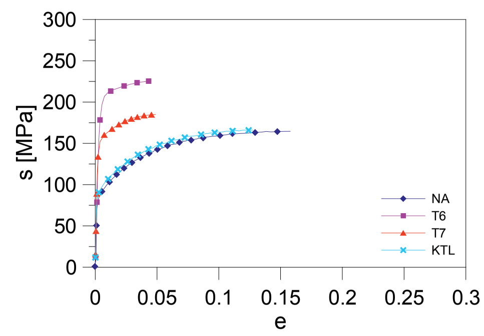 (b)	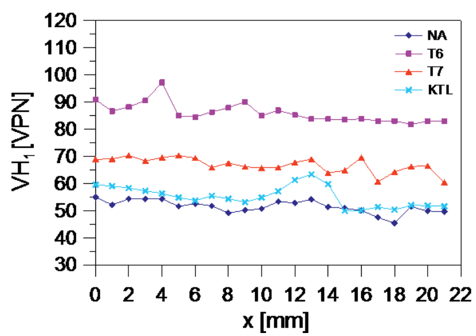 (c)
Initial T6	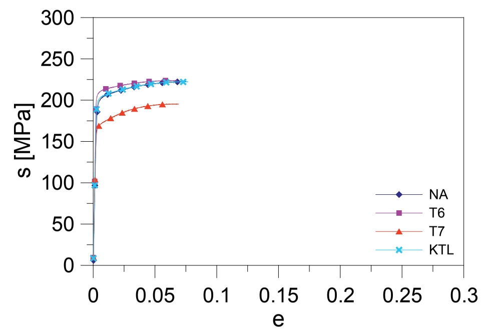 (d)	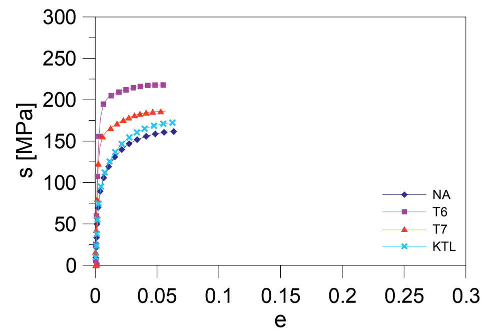 (e)	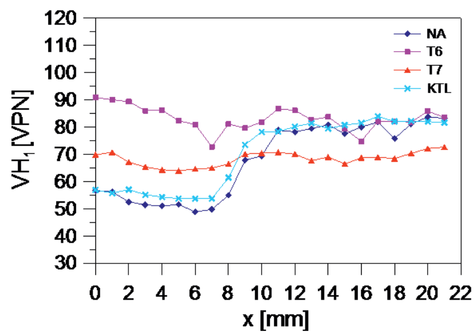 (f)

Figure 3.35: AA6060 – Uniaxial tensile test, Cross-weld tensile test and Hardness test – after NA and PWHT

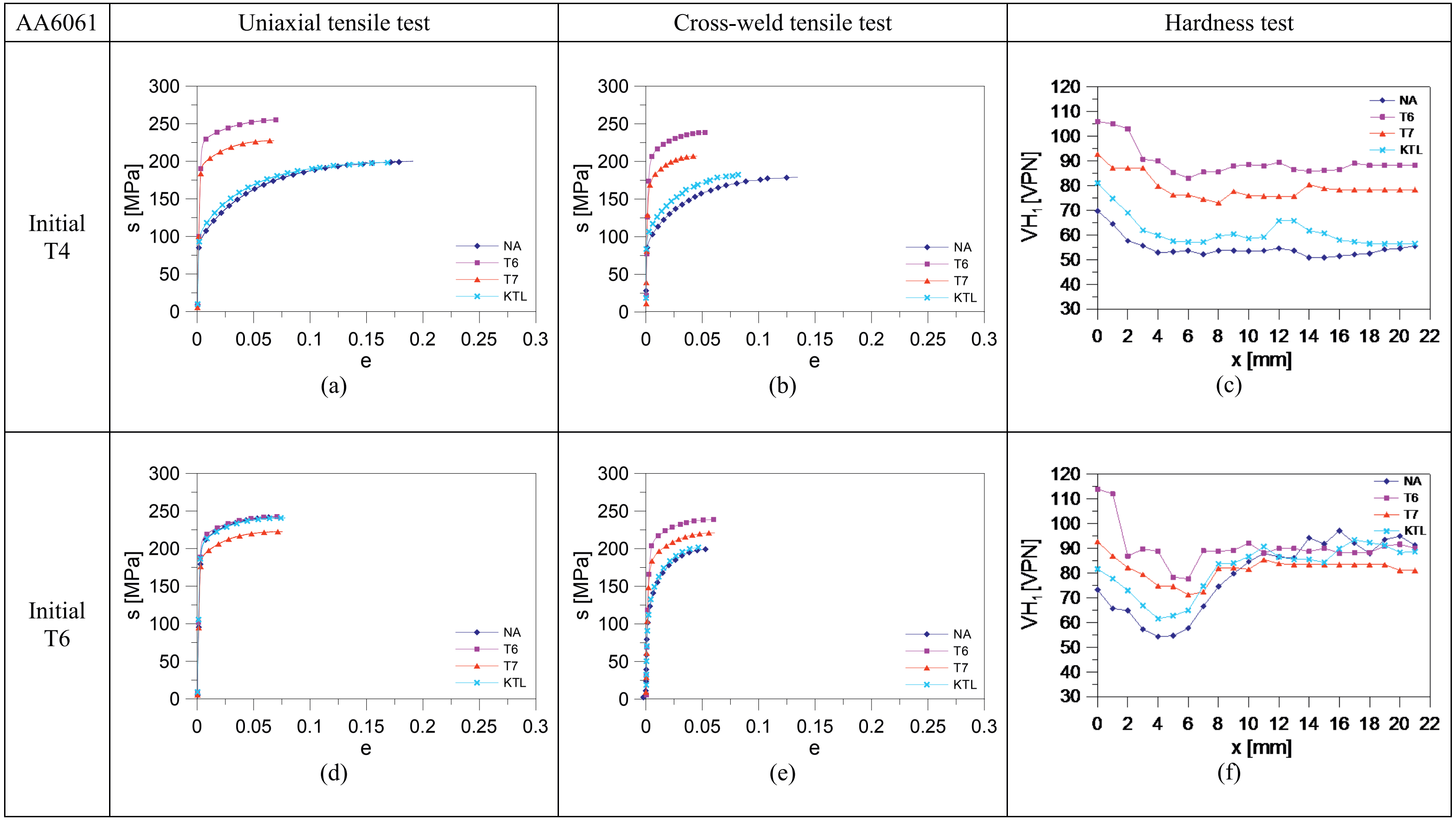

Figure 3.36: AA6061 – Uniaxial tensile test, Cross-weld tensile test and Hardness test – after NA and PWHT

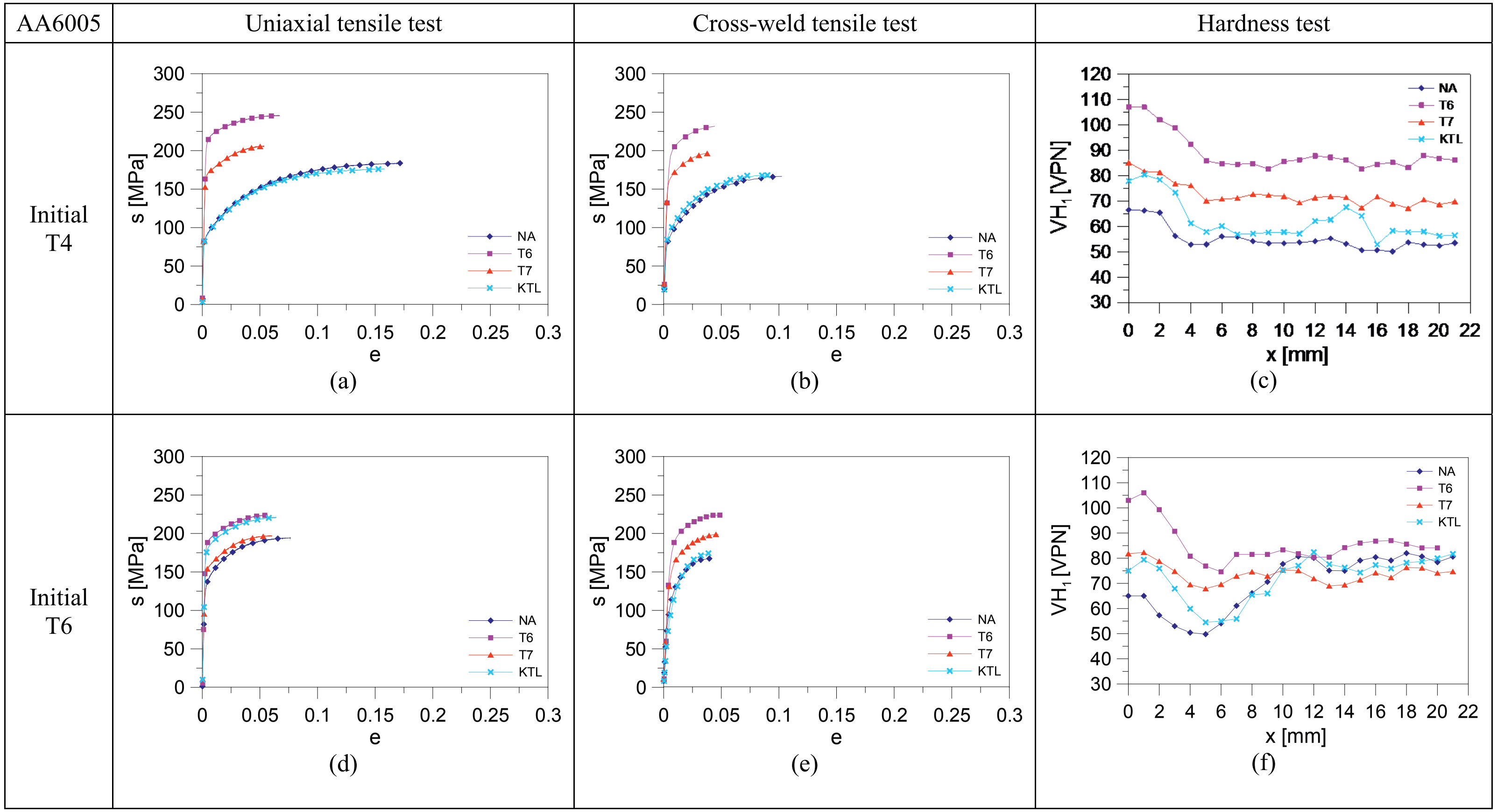

Figure 3.37: AA6005 – Uniaxial tensile test, Cross-weld tensile test and Hardness test – after NA and PWHT

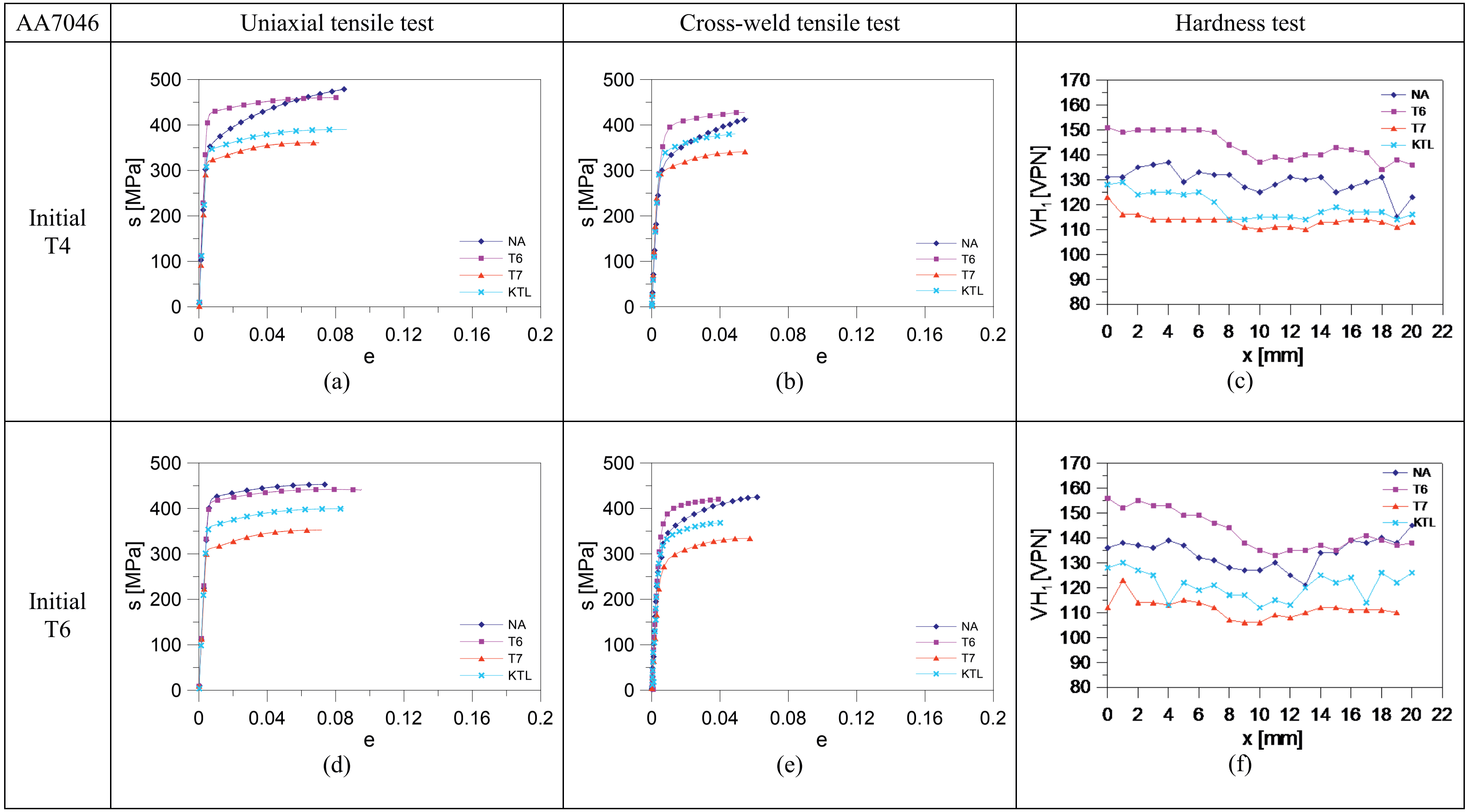

Figure 3.38: AA7046 – Uniaxial tensile test, Cross-weld tensile test and Hardness test – after NA and PWHT

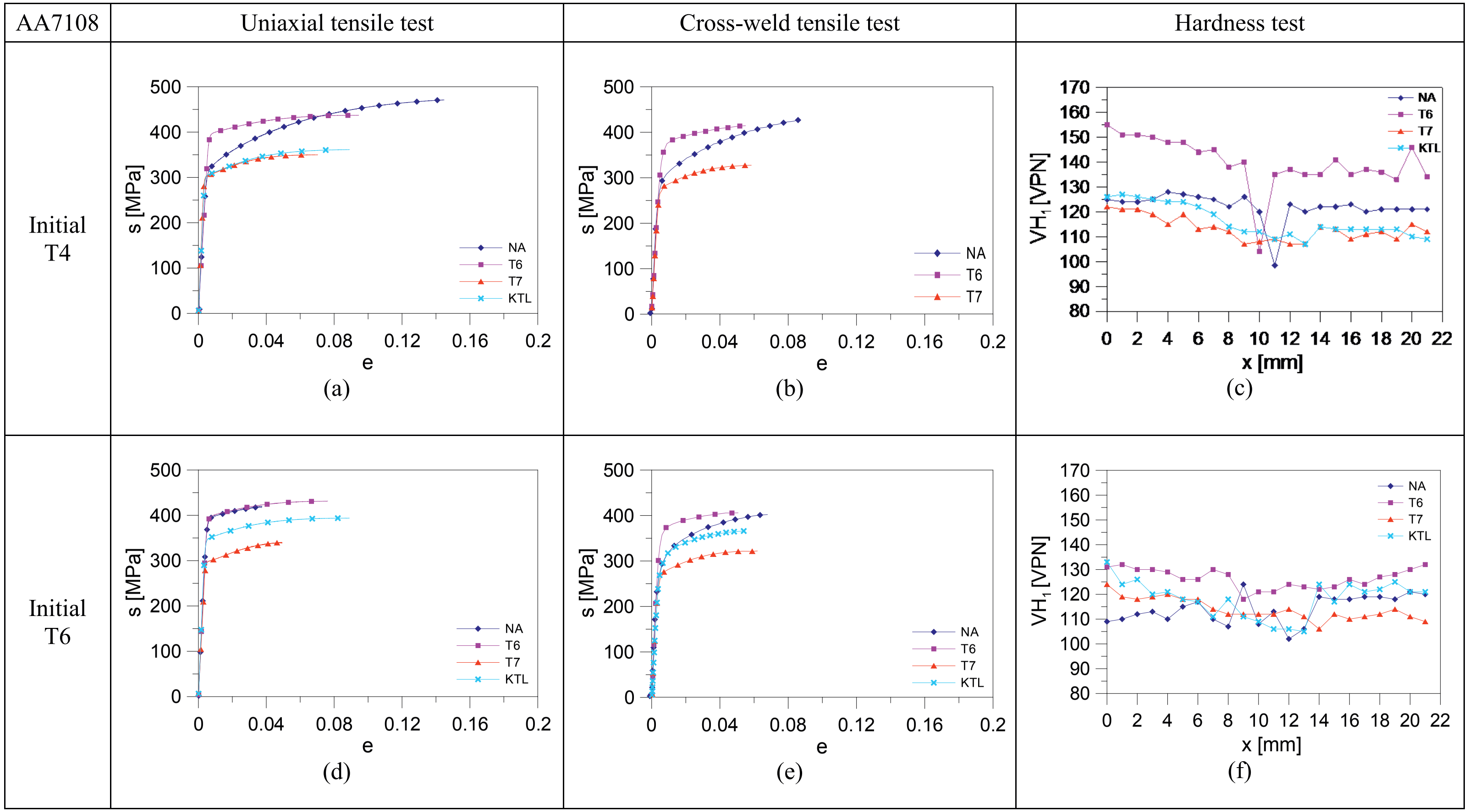

Figure 3.39: AA7108 – Uniaxial tensile test, Cross-weld tensile test and Hardness test – after NA and PWHT

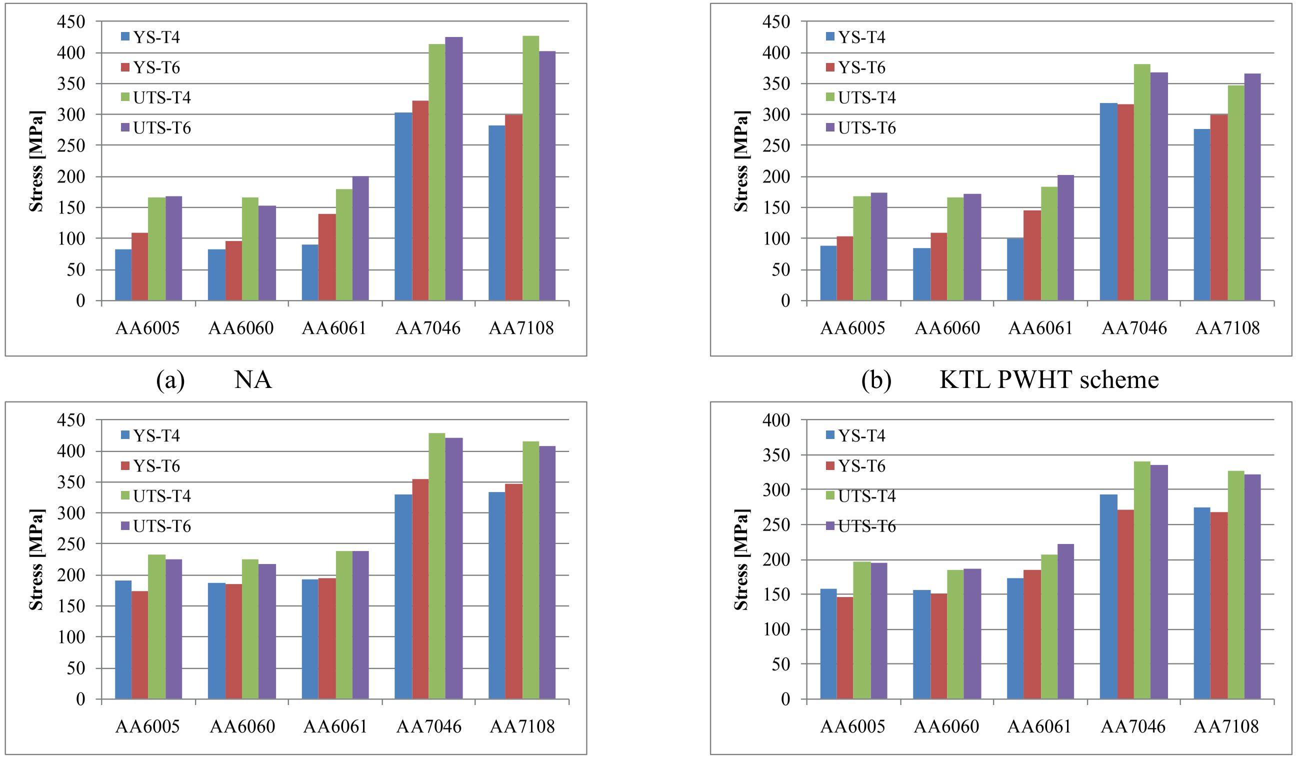

(a) NA

(b) KTL PWHT scheme

(c) T6 PWHT scheme

(d) T7 PWHT scheme

Figure 3.40: Yield stress (YS) and Ultimate Tensile Stress (UTS) column graph for the five different alloys, initial T4 and T6 cross-weld specimens

4 Simulations

4.1 Introduction

This chapter presents results from the models and modelling procedures, both based on the NaMo model and the through-process simulations, in comparison with the experimental results.

The NaMo model is presently not fully developed for all the alloys and initial tempers included in the test program. Further, in Chapter 3 (Section 3.5.2), it was found that the original *as-delivered* plates of AA6005 in (the planned) T6 condition had too low yield stress, probably due to improper heat treatment. Thus, these experimental data are not explored in the present validation studies and, hence, only predictions and simulations for AA6060 and AA6061 in initial temper T6 are covered. The study investigates and documents each of the four PWHT schemes for these two materials. The experimental results for AA6xxx initial temper T4 and AA7xxx in both tempers are currently used for further development of the NaMo model in concurrent research performed by Hydro Aluminium.

As described in Chapter 2, the NaMo model consists of three parts: a precipitation model, a yield strength model and a work hardening model. The data from the precipitation model constitute the input data for the two latter models. The results of the NaMo model are presented in terms of stress-strain curves relating the flow stress σ_f to the plastic strain ε^p, and in terms of hardness profiles.

For the structural response simulations using LS-DYNA, a parametric study was carried out to explore and document effects of element type, mesh size and effects of non-local regularisation.

4.2 Uniaxial tensile test simulations

The prime input to the NaMo simulations is the temperature histories, derived from WELDSIM, at a number of reference points in the structure. In addition, the material constants given in Chapter 2 (Table 2.1) are used. The predicted flow stress σ_f (as a function of the plastic strain ε^p and as resulting from NaMo and Equation 2.17) is plotted in Figures 4.1 to 4.3 for the three alloys and four PWHT procedures considered. In the same figures, the experimental results from the coupon test are given.

AA6060

The measured and predicted work hardening curves for AA6060 are given in Figure 4.1. As seen, there is very good agreement between the curves, thus indicating that the NaMo model is able to predict the precipitation mechanisms and precipitate strengthening effects of this alloy.

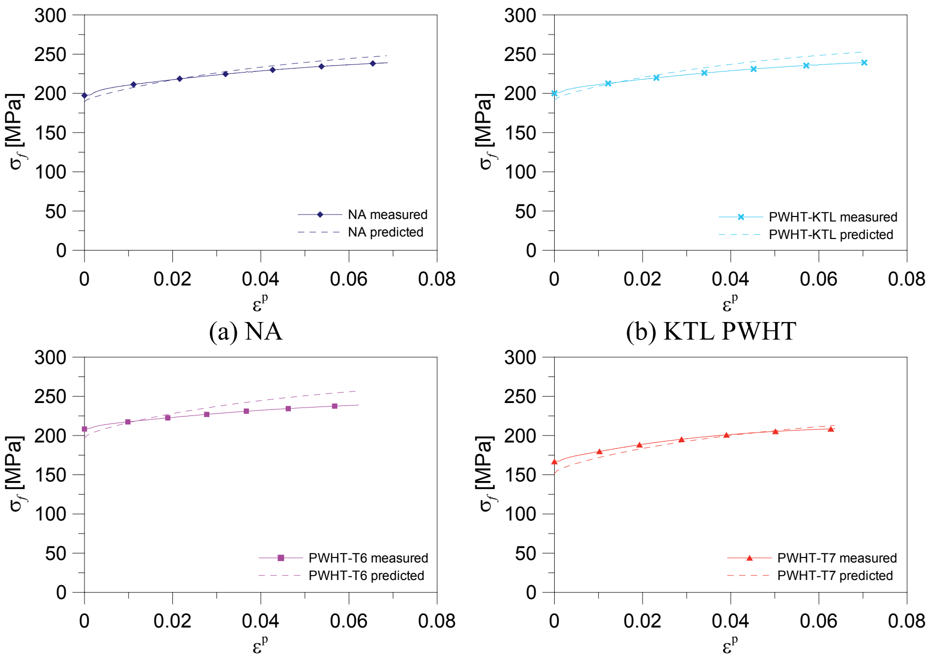

(a) NA (b) KTL PWHT

(c) T6 PWHT (d) T7 PWHT

Figure 4.1: Measured and predicted flow stress vs. logarithmic plastic strain, AA6060 coupons, initial T6

AA6061

Figure 4.2 depicts the measured and predicted work hardening curves for the AA6061 alloy. For this material, the base version of the NaMo model predicts much too high strength for the NA, KTL and T6 PWHT schemes, while the agreement is quite good for T7 PWHT scheme. This signalises that the base version of the NaMo model needs modifications. The probable cause for the deviation is the model calculates too much precipitates. And since only yield strength model is affected, the principal amendment to the model, relates to the parameters extracted from PSD (precipitation model) which are then transferred to the yield strength model.

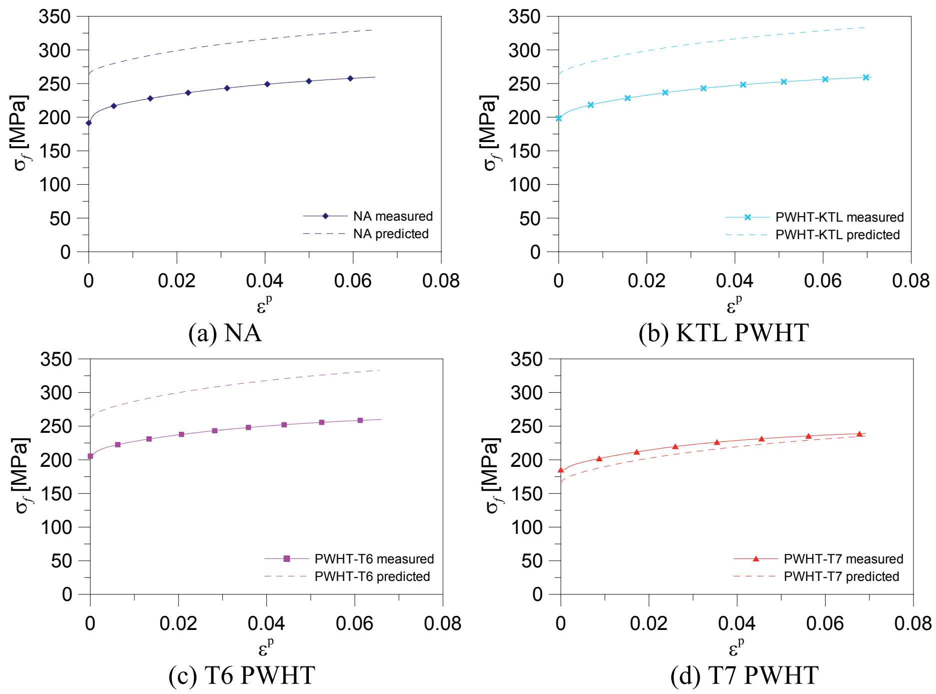

Figure 4.2: Measured and predicted flow stress vs. logarithmic plastic strain, AA6061coupons, initial T6

4.3 Hardness profile predictions

The Through-process Modelling scheme explored in the present study allows to estimate the spatial distribution of the yield stress and work hardening as a function of the distance x (in mm) from the weld fusion line. Uniaxial tensile tests are intractable for experimental validation due to the large spatial gradients in the property variation. Instead, an indirect comparison is carried out, where the yield stress predicted by NaMo is converted to hardness VH (in VPN) by means of Equation 3.4 - 3.5 and compared with the corresponding experimental results already presented and discussed in Section 3.6.2.

AA6060

Figure 4.3 shows the measured and predicted hardness profiles for alloy AA6060. Overall, the agreement is very good for the base material, i.e. outside the HAZ, which is in agreement with the results found in the preceding section. The predicted extent of the HAZ is somewhat smaller (2 - 3 mm) than what is shown by the associated experimental data. In more detail, for the NA PWHT scheme NaMo *underestimates* the minimum hardness in the HAZ by approximately 16%, while for KTL PWHT scheme, the minimum HAZ strength is *overestimated* by about 18%. For the T6 and T7 PWHT schemes, NaMo predicts almost constant hardness over the entire HAZ. This is, however, not in full accord with the experimental data; the hardness is significantly underestimated near the fusion line (from 0-7 mm) for both PWHT schemes.

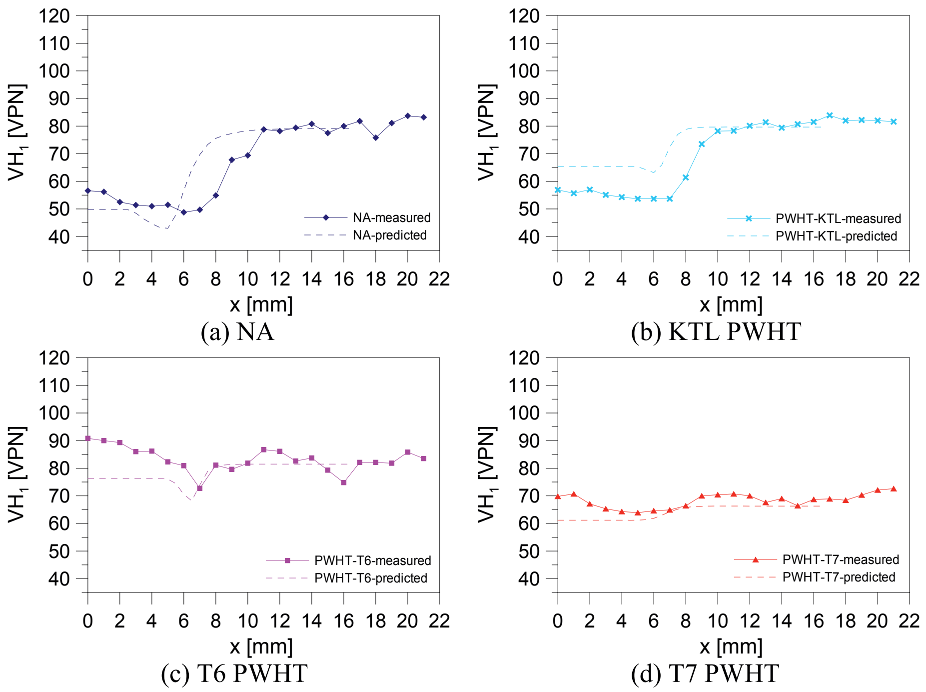

(a) NA

(b) KTL PWHT

(c) T6 PWHT

(d) T7 PWHT

Figure 4.3: Experimental and simulated hardness profiles AA6060, initial T6

AA6061

The measured and predicted hardness profiles for alloy AA6061 in initial condition T6 are shown in Figure 4.4. For this material the deviations are large. For the NA and KTL PWHT schemes, the predicted width of the HAZ is smaller than the measured ones, and the hardness exceeds the measured one both close to the fusion line and in the base material. Still, the predicted minimum values are rather similar to the experimental values. The discrepancies are significant also for T6 and T7 PWHT schemes.

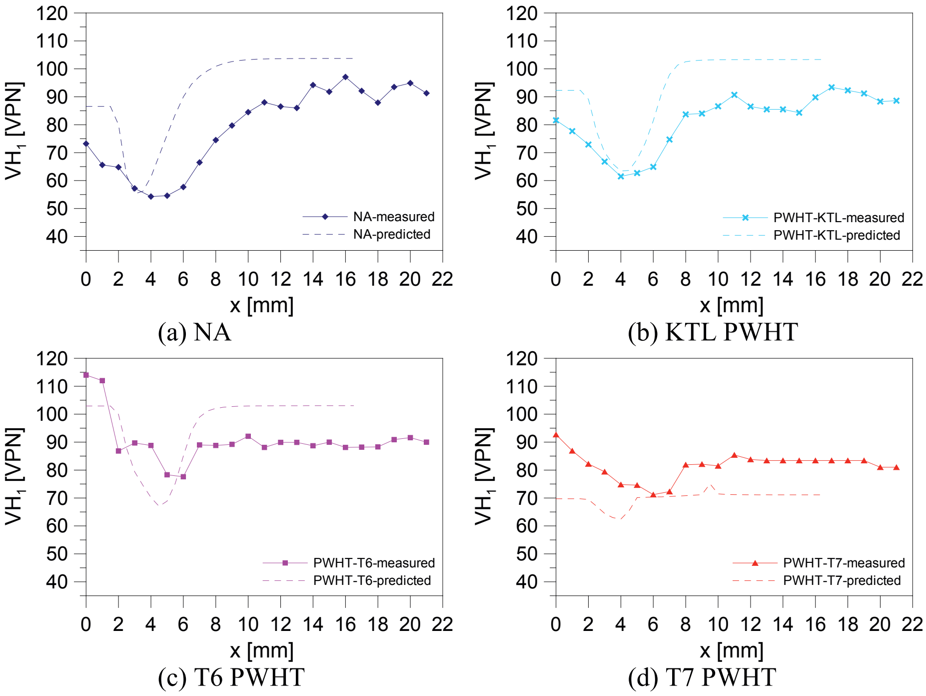

(a) NA (b) KTL PWHT

(c) T6 PWHT (d) T7 PWHT

Figure 4.4: Experimental and simulated hardness AA6061, initial T6

4.4 Cross-weld tensile test simulations

The present section presents the results of the through-process simulations of the cross-weld tensile tests specimens, in comparison with experimental data. The first section summarises the methods and assumptions for the analyses. In the consecutive sections results from three different finite element models are presented: 1) shell analysis excluding non-local thinning, 2) shell analysis including non-local thinning and 3) brick element analysis. The latter Section includes comparisons between results obtained with the three methods. All simulations were carried out using the explicit solver of LS-DYNA.

Figure 4.5 illustrates results from an experiment (AA6060-T6, PWHT-NA) and a corresponding numerical simulation. Part (a) shows a picture taken after failure, which occurred by strain localisation and sub-sequent material fracture in the HAZ. Note the position of the weld indicated by the black lines above and under the specimen. Part (b) of the Figure presents the deformations field as measured by DIC. Note the strain localisation in the HAZ at about 12 mm distance from the weld. The result from a numerical analysis performed in LS-DYNA is depicted in part (c) of the figure. It can be noted that the necking initially occurred on both sides of the weld, followed by subsequent intensified localisation and fracture on one of the two sides.

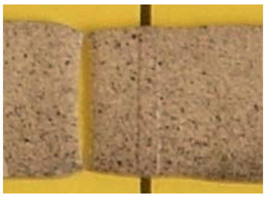

(a) Physical cross-weld tensile specimen

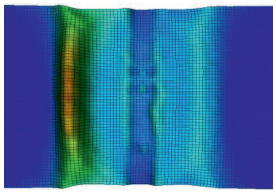

(b) Deformation near the weld by DIC

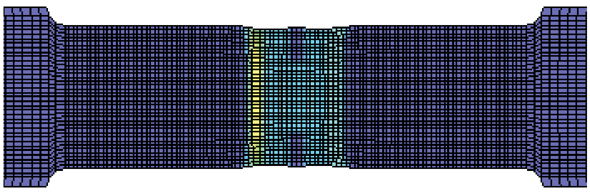

(c) Strain localization in the HAZ given by FEM

Figure 4.5: Physical and virtual cross-weld tensile specimen from FE simulation

4.4.1 Methods and assumptions

Material models and loading

The actual weld part was represented by a separate past and a standard model elastic-plastic material model (*MAT_PIECEWISE_LINEAR_PLASTICITY) of LS-DYNA. The remaining of the specimen, i.e. the HAZ and base metal, was modelled by using a user-defined material mode (*MAT_USER_DEFINED_MATERIALS), in which the yield stress and the work hardening are modelled by means of NaMo, as presented previously.

Loading was applied at one end of the clamped specimen ends, while the other clamped end was constrained. Total displacement of 20 mm was imposed over 15 ms raise time. The raise time is shorter than the duration of the experimental test. Nevertheless, in all simulations the kinetic energy was only a small fraction of the internal energy of the system to ensure that quasi-static response is achieved. The choice of the chosen total displacement was based on the ductility of the welded joint itself.

Shell elements and non-local thinning

The response of thin-walled structures, where the dimension in the thickness direction is much smaller than the other two directions, is most efficiently investigated by shell theory or FE analyses using shell elements, in particular when using explicit solution methods. The gain in efficiency stems from a lowered number of degrees of freedom and a higher critical time step needed to perform the analyses.

When shell elements are used to study failure due to strain localisation and material fracture, however, the solution is prone to convergence problems, as the strain tends to localize randomly with mesh refinements, leading to solutions that can change significantly from one mesh to another. Even if a sufficiently dense mesh may appear to represent the position of the strain localization well, the evolution of the plastic thinning may be incorrect. The absence of through-the-thickness stress in the shell causes a highly concentrated plastic thinning that in reality would takes place over a larger region. This problem does not appear when using brick elements.

As discussed by Wang et al. [41], the non-local approach was originally proposed by Bazant and Pijaudier-Gabot [44] in order to solve the mesh dependence problem in softening materials. In damage mechanics it is generally experienced and reported that non-local damage evolution greatly reduces the mesh sensitivity of fracture predictions, leading to results that converge to a unique solution as the mesh is refined. Similarly, Wang et al. [41] suggested remedying the shell element issues discussed above with the concept of non-local plastic thinning for better response prediction regardless of element sizes applied. The non local approach, introduced by Lademo et al [34] was adopted, where the plastic thickness strain ratio $\dot{\varepsilon}_t^p$ is the variable subjected to the nonlocal equation. Dørum et al [5] also applied this method so that the resistance of the shell elements towards thinning will be enhanced (depends on the radius of non-local domain).Thus, increasing ductility as the predicted strain localization will occur later. Another feature of non-local approach that allows the definition of separate work hardening curves for various pre-strain levels within one material ID can be referred to Lademo et al. [35]. Apart from the non-local thinning approach studied here, there are other non-local regularisations or regularisation by including rate dependence in the constitutive model by Belytschko et al. [38] to solve the mesh dependency matters.

In the approach of Wang et al. [41], the incremental plastic thickness strain in a given element is calculated as a weighted average of the incremental plastic thickness strains of elements within a non-local domain defined by a radius L from the centre of the considered element, illustrated in Figure 4.6. The radius L is typically in the order of the thickness of the material. Note that only integration points lying in the same plane within the radius are considered in the averaging procedure. By this approach, the resistance of the shell elements towards thinning will be enhanced, depending on the size of the non-local domain. As a result, the structural ductility increases. The *MAT_NONLOCAL option in LS-DYNA is used to invoke non-local averaging of a given history variable. Reference is made to Wang [41] for a more detailed presentation of the approach.

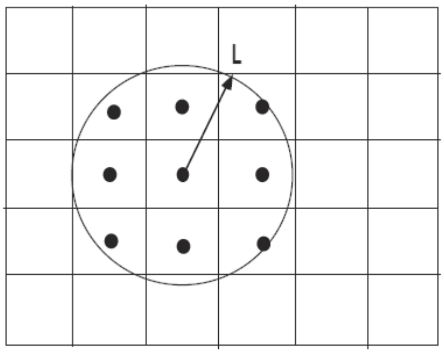

Figure 4.6: Radius of non-local approach that span for a few elements [18]

4.4.2 Base model(s): Shell elements without non-local thinning

This section presents results obtained with a set of base models using shell elements without regularisation by non-local thinning, in comparison with the experimental data. Seven different meshes, with minimum element size ranging from 0.6 mm to 3.0 mm, were used to evaluate the mesh sensitivity. The minimum size was used in the parts of the cross-weld tensile test specimen that were prone to experience strain localisation and fracture, i.e. the weak HAZ and weld region. The default shell element in LS-DYNA was used, namely the Belytschko-Tsay shell element with one-point Gauss quadrature and two integration points through the thickness. Hourglass control was activated to control zero-energy modes in the under-integrated shell elements. The number of elements for the various models is: 16722 (0.6 mm), 12246 (0.74 mm), 9580 (0.9 mm), 8292 (1.0 mm), 6448 (1.2 mm), 1814 (2.3 mm) and 1031 (3.0 mm).

AA6060

The response curves for AA6060 (initial condition T6) are shown in Figure 4.7 (a), (b), (c), and (d) for the NA, KTL, T6 and T7 PWHT schemes, respectively. The various element sizes have, at least for this material, little effect on the force-deformation characteristics. Some mesh dependency is, however, seen on the tail of the force-deformation curves, i.e. a steeper slope and reduced ductility is predicted with decreasing element size. A convergent solution is reached with element size 0.9 mm for all PWHT schemes. Except for the KTL PWHT scheme there is good agreement between the experimental and simulated results. For the KTL PWHT the discrepancy is large. Here, the onset of yielding in the experiment takes place at a significantly lower stress than for the simulation. Further, the ultimate strength is obtained at a deformation of about 7 mm (not shown in figure), which is much higher than the elongation observed in the experimental tests.

The large deviation observed for the KTL PWHT is understandable from the associated deviation in experimental and predicted hardness profiles (See Figure 4.3). The strength of the specimen is governed by the minimum strength in the HAZ and, as seen from the mentioned figure, NaMo over predicts the strength considerably for this PWHT scheme. The same effect reduces the strength difference, i.e. inhomogeneity in the specimen, which again increases the predicted elongation of the specimen.

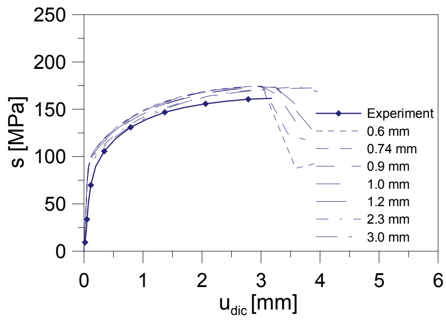

(a) NA

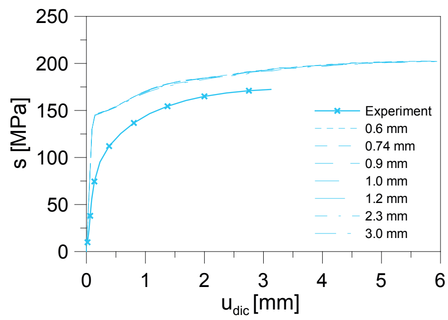

(b) KTL PWHT

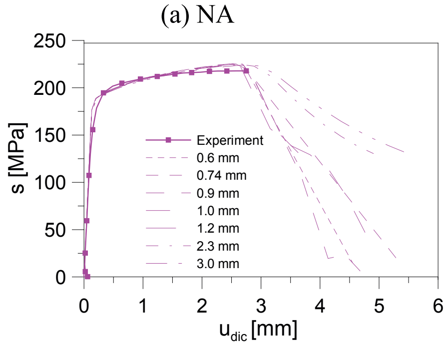

(c) T6 PWHT

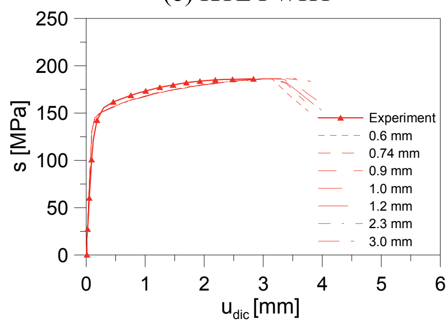

(d) T7 PWHT

Figure 4.7: Engineering stress vs. deformation of cross weld tensile test – a comparison between experiment and simulations with various mesh sizes for AA6060

AA6061

The simulated response curves for AA6061 deviate significantly from the experimental ones for all PWHTs see Figure 4.8. This deviation is most obvious for the elongation at ultimate stress, with values only a fraction of the experimental values. The predicted ultimate stress agrees reasonably well with the experiments for the NA and KTL PWHT schemes but differs significantly for the T6 and T7 PWHT schemes.

Again the deviations are reasonable given the discrepancies between the experimental and predicted hardness profiles (See Figure 4.5). In other words; rather accurate predictions of the minimum strength (NA and KTL PWHT) results in rather accurate predictions of the ultimate capacity of the specimens. Further, the generally low ductility of the cross-weld tensile specimens correlates well with the trend that NaMo predicts too narrow and sharp HAZ softening. Again, it can be concluded that for this alloy, the present NaMo model is not sufficiently developed.

For this material the mesh dependency is more pronounced, but a rather good convergence is obtained for an element size of 0.9 mm.

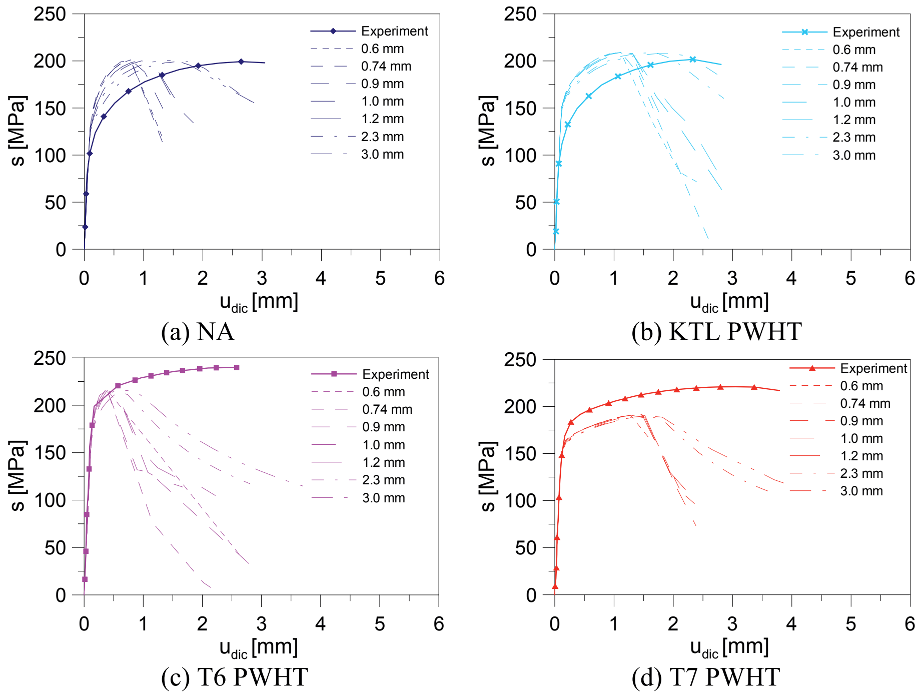

Figure 4.8: Engineering stress vs. deformation of cross weld tensile test – a comparison between experiment and simulations with various mesh sizes for AA6061

4.4.3 Shell elements with non-local thinning

This section presents results obtained with shell elements and the regularisation technique of non-local (NL) thinning in comparison with experimental data and results obtained shell elements without regularisation. The analyses are carried out for element sizes 0.6 mm, 0.7 mm and 0.9 mm and the radius of non-local thinning was taken as 2.0 mm, 3.0 mm and 4.0 mm. The chosen radius was due to the observation that the width of the strain localization in physical experiments is often the same order as the sheet thickness.

AA6060

Figure 4.9, Figure 4.10 and Figure 4.11 compare experimental and numerical results (without and with NL thinning), for the AA6060-T6 material, of the NA, T6 and T7 PWHT schemes, respectively. For all of these analyses the non-local radius of influence was set to 2.0 mm. As seen, the introduction of the NL thinning significantly increases the predicted specimen ductility. The general trend is that the analyses without NL thinning are in better accordance with the experiments, than the ones with NL thinning.

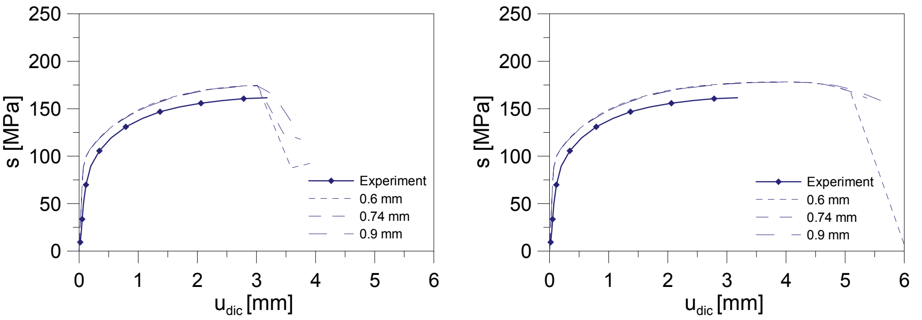

(a) without NL (b) with NL = 2.0 mm

Figure 4.9: Engineering stress vs. deformation of cross weld tensile test – a comparison between experiment and numerical simulations for AA6060 after NA

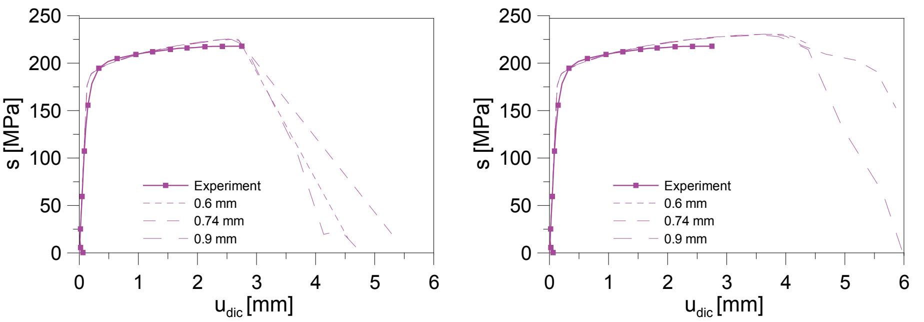

(a) without NL (b) with NL = 2.0 mm

Figure 4.10: Engineering stress vs. deformation of cross weld tensile test – a comparison between experiment and numerical simulations for AA6060 after PWHT-T6

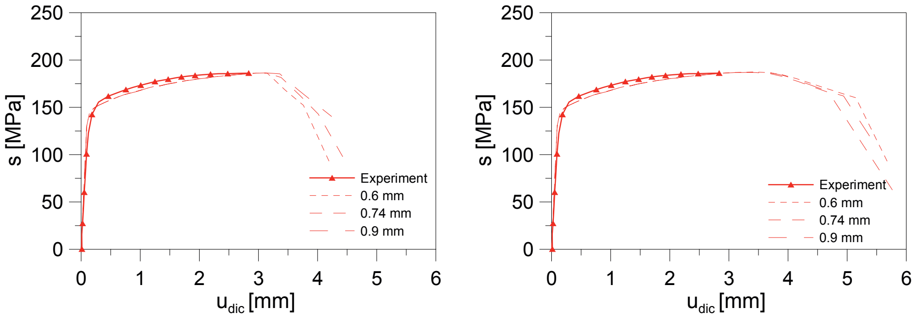

(a) without NL (b) with NL = 2.0 mm

Figure 4.11: Engineering stress vs. deformation of cross weld tensile test – a comparison between experiment and numerical simulations for AA6060 after PWHT-T7

AA6061

Figure 4.12, Figure 4.13 and Figure 4.14 compare results obtained with and without NL thinning, for the AA6061-T6 material, of the NA, T6 and T7 PWHT schemes, respectively. The response curves for KTL PWHT scheme showed the same tendency as for NA PWHT and are not presented. The figures include results with various radius of influence as specified by the caption of each figure. The deviations between the experimental and predicted results are rather large for this alloy, and it has already been concluded that this is due to weaknesses in the (present version of the) NaMo model for this alloy. The results contained herein are thus serving more to document experience with mesh convergence and non-local regularisation for the problem at hand than the purpose of model validation.

The use of the concept of non-local thinning in the analyses results in a significant increase in the predicted ultimate stress and specimen elongation. As should be expected, the larger radius of influence the larger becomes the predicted specimen ductility. For NA (and KTL) PWHT the elongation is underestimated without non-local thinning. With non-local thinning the elongation may artificially be made to correspond to the experimental results. The results for a radius of influence of 2.0 mm and 3.0 mm are almost indistinguishable. For T6 and T7 PWHT schemes, the simulated elongation is grossly underestimated even for large values of the radius of influence. This is considered to be caused by the much larger inhomogeneity in properties exhibited by the model than the experiments, as documented by the experimental and predicted hardness profiles. The results are relatively independent of the mesh chosen.

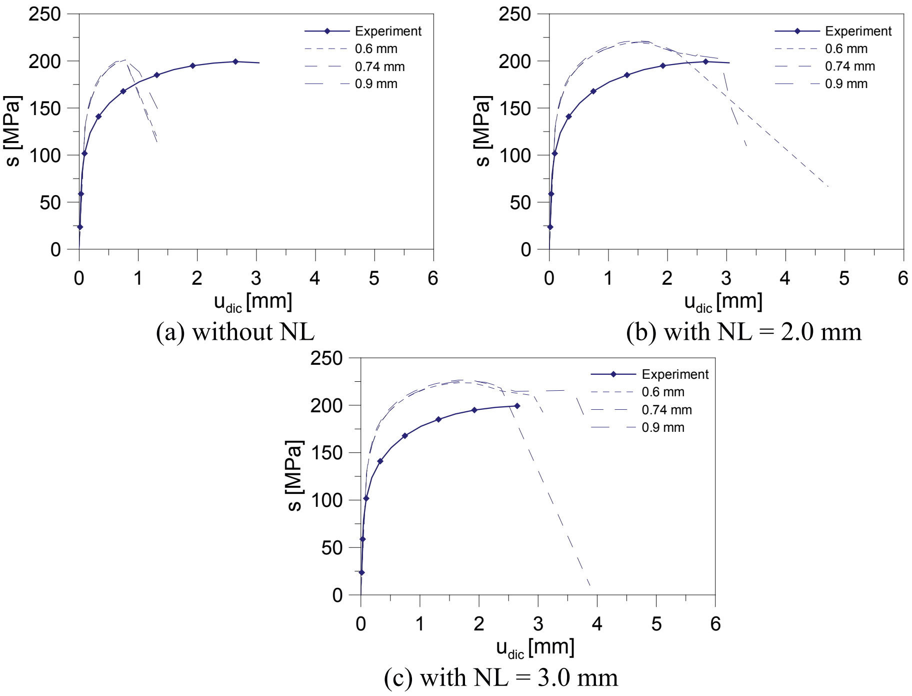

Figure 4.12: Engineering stress vs. deformation of cross weld tensile test – a comparison between experiment and numerical simulations for AA6061 after NA

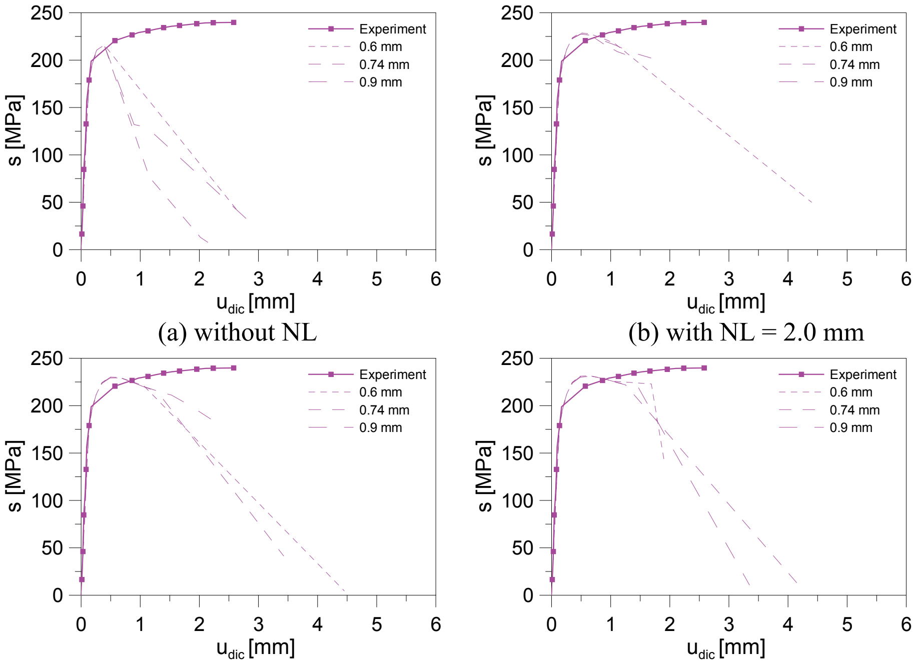

(a) without NL (b) with NL = 2.0 mm

(c) with NL = 3.0 mm (d) with NL = 4.0 mm

Figure 4.13: Engineering stress vs. deformation of cross weld tensile test – a comparison between experiment and numerical simulations for AA6061 after PWHT-T6

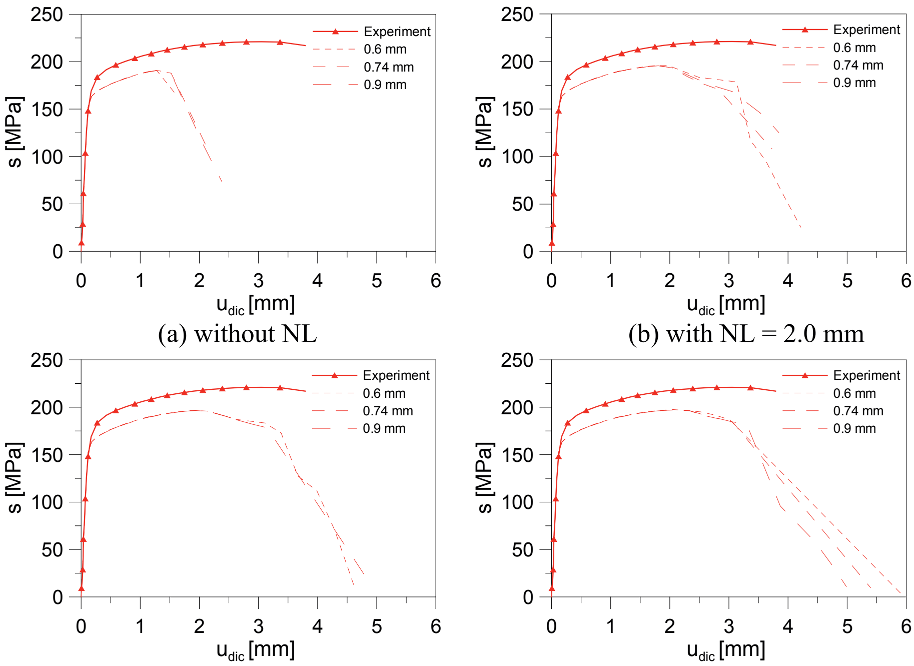

(a) without NL (b) with NL = 2.0 mm

(c) with NL = 3.0 mm (d) with NL = 4.0 mm

Figure 4.14: Engineering stress vs. deformation of cross weld tensile test – a comparison between experiment and numerical simulations for AA6061 after PWHT-T7

4.4.4 Shell vs. brick elements

In this sub-study, a comparison is made between results obtained for shell and brick models. The brick model was built using the default constant-stress brick element in LS-DYNA having one node at each corner and using three elements through the thickness of the specimen. In both models, the element size was taken as 0.9 mm.

The response curves for AA6060-T6 and AA6061-T6 are given in Figure 4.15 and Figure 4.16, respectively. For NA and KTL PWHT, all analyses overestimate the ultimate stress, with the brick model giving the highest value. While T6 PWHT is well predicted for both alloys, T7 PWHT is underestimated for AA6061. Nevertheless, in accordance with the findings of Dørum et al., the brick analyses compares better with the shell element analysis using non-local regularisation than to the ones without this remedy.

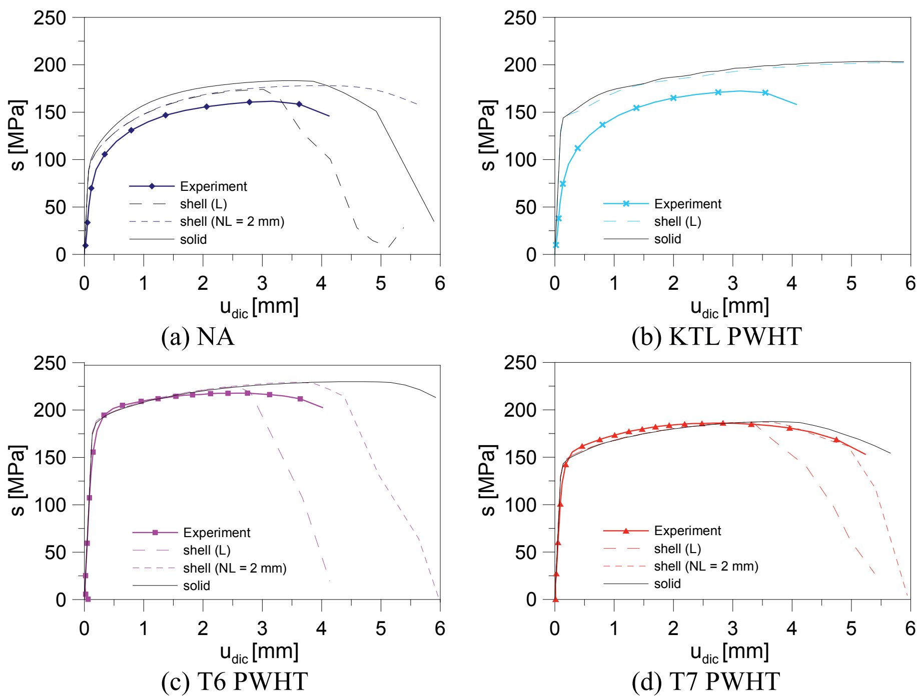

(a) NA (b) KTL PWHT
(c) T6 PWHT (d) T7 PWHT

Figure 4.15: Comparison of engineering stress vs. deformation curve, using shell and brick elements for AA6060

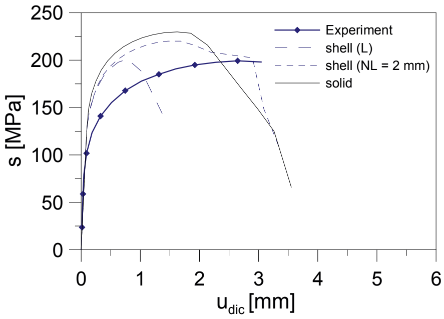

(a) NA

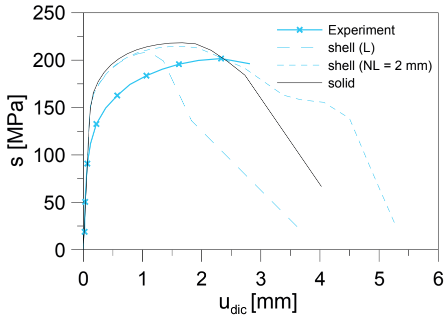

(b) KTL PWHT

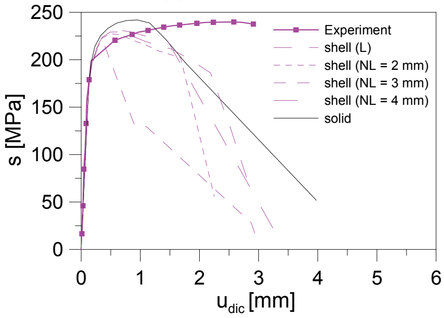

(c) T6 PWHT

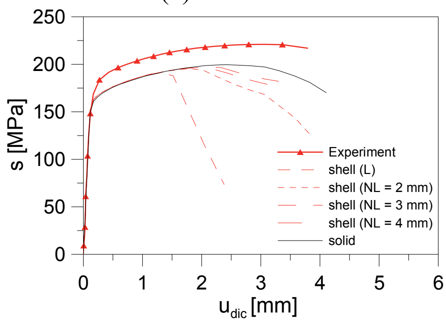

(d) T7 PWHT

Figure 4.16: Comparison of engineering stress vs. deformation curve, using shell and brick elements for AA6061

4.5 Discussion and concluding remarks

Simulations of uniaxial tensile test

The NaMo model gives good predictions for AA6060 alloy subjected to NA and all PWHT schemes. The same results would be expected for AA6005 as the chemical composition only deviates in terms of Mn and Cu. The NaMo model greatly over-predicts the yield stress for NA, KTL and T6 PWHT scheme of AA6061, while the agreement is quite good for T7 PWHT scheme. Anyhow, this indicates that the NaMo model needs modifications for alloys of this, or similar composition.

Simulations of hardness tests

For AA6060 subjected to NA, NaMo underestimates slightly the minimum hardness in the HAZ but overestimates it for KTL PWHT. For both cases, the agreement is very good in the base material outside the HAZ. NaMo predicts an almost constant hardness over the entire profile both for T6 and T7 PWHT schemes, but it underestimates the hardness significantly near the fusion line for both cases. For AA6061, the predicted hardness profile is too inaccurate.

Simulations of cross-weld tensile tests

The NaMo model gives good results for AA6060-T6 except for PWHT-KTL. The results are inaccurate for AA6061-T6.

A fine mesh is necessary both for shell and brick elements to get accurate predictions for the ductility of the welded aluminium connections in question. Dørum et al. [5] found that shell element simulations using a non-local radius of influence equal to the thickness of the specimen gave results comparable to those of brick element simulations. Wang et al. [41] found that a radius of influence equal to half of the specimen thickness improved the shell element simulations. In the present investigation, a non-local radius of influence equal to 2/3 of the thickness gave best results. The correlation is, however, highly dependent upon the predictions of the NaMo model. An actual experimental validation and the development of a modelling guideline require further improvements of the NaMo model, in particular for the alloy AA6061 and alloys of similar composition. Based on the needs documented by the present study, concurrent work has been undertaken by Hydro Aluminium to improve the NaMo model. Model revisions now exist that will be evaluated towards the experimental database documented herein in forthcoming studies.

5 Conclusions

This thesis evaluates the accuracy, efficiency and robustness of the 'Through Process Modelling' concept previously developed, discussed and evaluated by Myhr et al. [24, 25, 26, 28] and Dørum et al. [5]. Through experiments and numerical analysis, the evaluation covered various heat-treatable aluminium alloys of 6xxx and 7xxx series, in different initial temper conditions and relevant PWHT schemes. The secondary objectives stated in the introduction are

1. To establish an experimental database addressing the capacity and ductility of simple welded joints made of heat-treatable aluminium structures suited for the overall objective.
2. To perform numerical investigations based on the TPM concept.
3. The numerical study shall document present capabilities and limitations of the present sub-model versions and identify needs for further research.

An experimental database has been established. The experimental study investigates effects of the main steps in the manufacturing of the joints; initial ageing and condition of the material, welding and PWHT. Five different alloys (AA6005, AA6060, AA6061, AA7046 and AA7108), two initial tempers (T4 and T6) and four different PWHT schemes were selected. Due to improper manufacturing control, it is concluded that the original plates of AA6005-T6 had a too low yield stress probably due to slow cooling (air cooling) after solution heat treatment. These data must be used with care in further validation studies since the actual thermal processing of the as-delivered material is uncertain. The remaining dataset is thought to meet with the stated objective.

A numerical study has been carried out to explore and document present capabilities and limitations of the TPM concept and associated sub-model versions. The NaMo model is presently not fully developed for all the alloys and initial tempers included in the test program. The NaMo version underlying the study is developed for AA6xxx alloys in stable conditions, i.e. for the materials in initial condition T6 but not for T4. For reasons stated above, the data for AA6005-T6 are excluded. In other words, numerical studies have only been carried out for AA6060 and AA6061 in initial temper T6.

The NaMo model shows promising results for alloy AA6060, but is inaccurate for AA6061. Based on the needs documented by the present study, concurrent work has been undertaken by Hydro Aluminium to remedy the observed deficiency of the NaMo version explored in the present study. This also includes work for AA7xxx alloys and other unstable conditions.

For the structural response simulations using LS-DYNA, a parametric study was carried out to explore and document effects of element type, mesh size and non-local regularisation. For the element type, shell elements were found to be convenient and efficient. The force vs. deformation curves presented clearly shows that the predicted response is mesh-dependent and a convergent solution was not achieved. This is due to the fact that strain tends to localize randomly with mesh refinement. Thus, results can change significantly from mesh to mesh. Convergent solution is then obtained with 0.9 mm mesh size in this study. Mesh density was found to have little influence on the prediction of strength. As for structural ductility, relatively accurate predictions of elongation were obtained by the refined mesh. Finer mesh was seen to represent the position of strain localisation very well, however not the evolution of the plastic thinning. Hence, non-local thinning is a potential remedy to regularise the situation and obtaining mesh convergence. The chosen non-local radius is often the same order as the sheet thickness, but for this study, two third of sheet thickness works better. For the same study, without non-local thinning, the numerical simulations generally predicted the structural strength and ductility reasonably well for AA6060, except KTL PWHT. However, the ductility was underestimated for AA6061. Whereas, with non-local thinning applied, good agreement between the experimental and numerical results was achieved for AA6060, but the elongation was over-estimated. Again, the ductility was underestimated for AA6061. Nevertheless, it can be seen that the prediction of ductility was improved by the nonlocal approach. It is also noted that it depends very much on the assumed criterion and parameters in the model. An actual experimental validation and the development of a modelling guideline require further improvements of the NaMo model, in particular for the alloys of similar composition to AA6061.

5.1 Recommendations for further work

This thesis brings contributions to the development of 'Through Process Modelling' concept for welded aluminium structures. A number of topics remain unsolved and wait for further works.

First, NaMo has been developed for 6xxx alloys and for stable conditions. The version explored herein, is inaccurate for the alloys AA6061. Work should be done to improve NaMo and to establish analogue models for unstable conditions and for 7xxx alloys. Note that such work has been undertaken in parallel to the present PhD study in concurrent activity at Hydro Aluminium. The revised NaMo model should be used in validation studies on the basis of the experimental database contained herein, and ultimately lead to a modelling guideline.

In this study, the response of the weld metal is not modelled. For 7xxx alloys, the weld metal is often weaker than the minimum HAZ strength and should be considered.

Validation studies on industrial systems should be performed. This work has partly been undertaken in concurrent studies at Benteler Aluminium Systems in parallel with the study documented herein.

Large-scale industrial exploitation of the methods demands for ease of use and numerical efficiency. Cohesive zone modelling should be explored further with the established methodology.

References

[1] A. Alisibramulisi, O. R. Myhr, O. –G. Lademo, P. K. Larsen, An experimental investigation of the Heat Affected Zone (HAZ) properties of AA6060 and AA7046 following different heat treatment schedules, Proceedings of the 12th International Conference on Aluminium Alloys, September 5-9 2010, Yokohama, Japan.

[2] A. Consid`ere, Annales des Ponts et Chauss´ees 6 (1885) 574.

[3] A. Guinire, Compte Rend., 206 (1938) 164.

[4] C. D. Marioara, A TEM Study of the Precipitates in a 6082 Al-Mg-Si Alloy System, Doctoral thesis in Department of Physics, 2000, Norwegian University of Science and Technology (NTNU): Trondheim, Norway.

[5] C. Dørum, O. -G. Lademo, O. R. Myhr, T. Berstad, O. S. Hopperstad, Finite element analyses of plastic failure in heat-affected zone of welded aluminium connections, Computers and Structures 88 (2010) 519-528.

[6] C. D. Marioara, S. J. Andersen, J. Jansen, H.W. Zandbergen, The influence of temperature and storage time at RT on nucleation of the β″ phase in a 6082 Al–Mg–Si alloy, Acta Materialia 51(3) (2003)789-796.

[7] E. J. Holm, H. G. Fjær, Inst. for Energy Tech. report: IFE/KR/F-99/021, February 1999.

[8] F. M. Mazzolani, V. Piluso, Prediction of the rotation capacity of aluminium alloy beams, Thin Walled Structures 27(1) (1997) 103-116.

[9] G. Groma, E. Kovacs-Csetenyi, Phil. Mag. 32 (1975) 869-872.

[10] G. Mrówka-Nowotnik, J. Sieniawski, Influence of heat treatment on the microstructure and mechanical properties of 6005 and 6082 aluminium alloys, Worldwide Congress

on Materials and Manufacturing Engineering and Technology (COMMENT), 16-19 May 2005.

[11] G. Waterloo, V. Hansen, J. Gjønnes, S. R. Skjervold, Mater. Sci. Eng. A303 (2001) 226-233.

[12] H. G. Hildrum, Stiffened aluminium plates subjected to impact loading, Doctoral thesis in Department of Structural Engineering, 2002, Norwegian University of Science and Technology (NTNU): Trondheim, Norway.

[13] J. E. Hatch, Aluminium: Properties and Physical Metallurgy, Metals Park, OH, American Society for Metals, 1984.

[14] L. Sandviken, Strekkstav utregner1, Tensile test dimension worksheet, Sintef, 2008.

[15] L. Zheng, D. Petry, H. Rapp, T. Wierzbicki, Characterisation of material and fracture of AA6061 butt weld, Thin-Walled Structures 47 (2009) 431-441.

[16] Livermore Software Technology Corporation (LSTC), LS-DYNA Keyword User's Manual, 2001, Version 960, Vol. I and II.

[17] M. G. Cockroft, D. J. Latham, Ductility and workability of metals, J Inst. Met. 96 (1968) 33-39.

[18] M. Matusiak, Strength and ductility of welded structures in aluminium alloys, Doctoral thesis in Department of Structural Engineering, 1999, Norwegian University of Science and Technology (NTNU): Trondheim, Norway.

[19] M. Murayama, K. Hono, Pre-Precipitate Clusters and Precipitation Processes in Al-Mg-Si Alloys, Acta Materialia 47(5) (1999) 1537-1548.

[20] O. R. Myhr, Modelling the microstructure and strength evolution in Al-Mg-Si alloys during multistage thermal processing, EAA – European Aluminium Technology

Platform- Working Group 5: Modelling, 4th workshop – Precipitation Modelling, Austria, 1-2 February 2011.

[21] O. R. Myhr, H. G. Fjær, S. Klokkehaug, E. J. Holm, Ø. Grong, A. O. Kluken, WELDSIM-An advanced simulation model for aluminium welding, in Ninth International Conference on Computer Technology in Welding 1999: Detroit, Michigan, USA. p. 52-63.

[22] O. R. Myhr, S. Klokkehaug, H. G. Fjær, Ø. Grong, A. O. Kluken, in The 5th International Conference on Trends in Welding Research, 1998: Georgia, USA.

[23] O. R. Myhr, S. Klokkehaug, H. G. Fjær, Ø. Grong, A. O. Kluken, Modelling of microstructure evolution, residual stresses and distortions in 6082-T6 aluminium weldments, Welding Journal 77 (1998) 286-292.

[24] O. R. Myhr, Ø. Grong, A multiscale modelling approach to the optimisation of welding conditions and heat treatment schedules for age hardening aluminium alloys, in 9th International Summer School on Aluminium Alloy Technology, Thermo-mechanical Processing and Forming, 20-24 August 2007: Trondheim, Norway.

[25] O. R. Myhr, Ø. Grong, H. G. Fjær, C. D. Marioara, Modelling of the microstructure and strength evolution in Al-Mg-Si alloys during multistage thermal processing, Acta Mater 52 (2004) 4997-5008.

[26] O. R. Myhr, Ø. Grong, K. O. Pedersen, A combined precipitation, yield strength and work hardening model for Al-Mg-Si alloys, Metallurgical and Materials Transactions A, 22 June 2010.

[27] O. R. Myhr, Ø. Grong, Modelling of non-isothermal transformations in alloys containing a particle distribution, Acta Mater 48 (2000) 1605-1615.

[28] O. R. Myhr, Ø. Grong, O. -G. Lademo, T. Tryland, Optimisation crash resistance of welded aluminium structures, Welding Journal 88 (2009) 42-45.

[29] O. R. Myhr, Ø. Grong, Process Modelling Applied to 6082-T6 Aluminium Weldments I– Reaction Kinetics, Acta metal mater 39(11) (1991) 2693-2702.

[30] O. R. Myhr, Ø. Grong, S. J. Andersen, Modelling of the age hardening behaviour of Al-Mg-Si alloys, Acta Mater 49 (2001) 65-75.

[31] O. R. Myhr, Ø. Grong, S. Klokkehaug, H. G. Fjær, Modelling of the microstructure and strength evolution during ageing and welding of Al-Mg-Si alloys. Mathematical Modelling of Weld Phenomena 6 (Editor H. Cerjak) - The Institute of Materials (2002) 337-363.

[32] O. R. Myhr, Ø. Grong, S. Klokkehaug, H.G. Fjær, Modelling the microstructure and strength evolution during ageing and welding of Al-Mg-Si alloys, 6th International Seminar on Numerical Analyses of Weldability, Graz-Seggau, Austria 1-3 October 2001.

[33] O. R. Myhr, Ø. Grong, Utilizing a predictive tool for designing welded aluminium components, Welding Journal 87(5) (2008) 36-39.

[34] O. -G. Lademo, O. Engler, M. Eriksson, O. S. Hopperstad, T. Berstad, An e experimental and numerical investigation on the applicability of the STM-2D model for rolled aluminium alloys. SINTEF report STF24 F04204, 2005, Trondheim.

[35] O. -G. Lademo, T. Berstad, T. Tryland, T. Furu, O. S. Hopperstad, M. Langseth, A model for process-based crash simulation. 8th International LS-DYNA User's Conference, 2004c, Detroit.

[36] P. Nègre, D. Steglich, W. Brocks, Crack extension in aluminium welds: a numerical approach using the Gurson-Tvergaard-Needleman model. Engineering Fracture Mechanics 71 (2004) 2365-2383.

[37] Standard Vickers Hardness (HV) test method, ISO 6507-1:1997.

[38] T. Belytschko, B. L. Wong, E. J. Plaskacz, Fission-fusion adaptivity in finite elements for nonlinear dynamics of shells, Computers and Structures 33 (1989) 1307–1323.

[39] T. Belytchko, W. K. Liu, B. Moran, Nonlinear Finite Elements for Continua and Structures, Chichester: Wiley, 2000

[40] T. Ungar, J. Lenvai, I. Kovacs, Aluminium 55 (1979) 663-668.

[41] T. Wang, O. S. Hopperstad, O. –G. Lademo, P. K. Larsen, Finite element analysis of welded beam-to –column joints in aluminium alloy EN AW 6082 T6, Finite Element Analysis 44 (2007) 1-16.

[42] V. Tarigopula, S. Dumoulin, Specimen geometries for mechanical testing, CRI-SIMLab Report, 29 August 2008.

[43] W. D. Lockwood, B. Tomaz, A. P. Reynolds, Mater.Sci.Eng. A323 (2002) 348–353.

[44] Z. P. Bazant, G. Pijaudier-Cabot, Nonlocal continuum damage, localisation instability and convergence, Journal of Applied Mechanics 55 (1998) 287-293.

[45] Ø. Grong, Capacity and ductility of welded structures, Progress plans and milestones - Multiscale Modelling of Metallic Materials (M4) Projects -Structural Impact Laboratory (SIMLab), NTNU, 2008, Trondheim, Norway.

[46] Ø. Grong, O. R. Myhr, The Institute of Materials (1993) 300-311.

Appendix: Cross-weld tensile tests

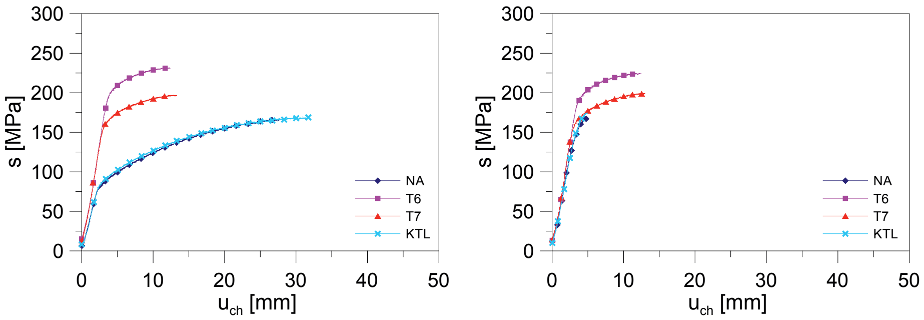

(a) Initial T4 (b) Initial T6

Appendix 1: Cross-weld tensile test results for AA6005, after NA and PWHT – Engineering stress vs. Crosshead deformation

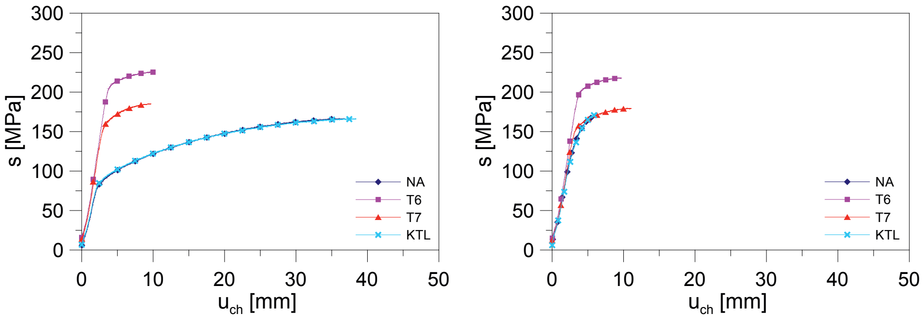

(a) Initial T4 (b) Initial T6

Appendix 2: Cross-weld tensile test results for AA6060, after NA and PWHT – Engineering stress vs. Crosshead deformation

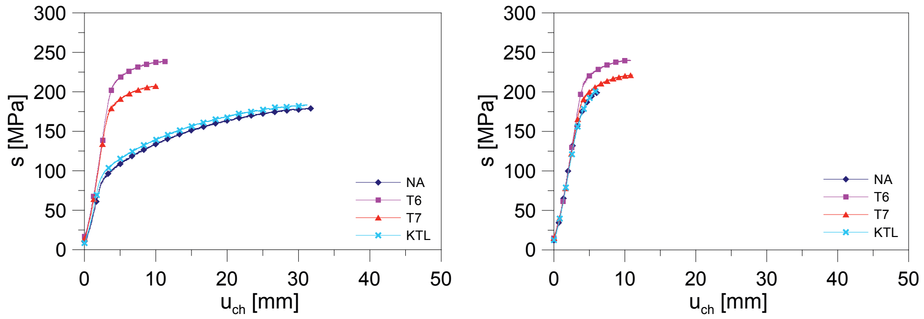

(a) Initial T4 (b) Initial T6

Appendix 3: Cross-weld tensile test results for AA6061, after NA and PWHT – Engineering stress vs. Crosshead deformation

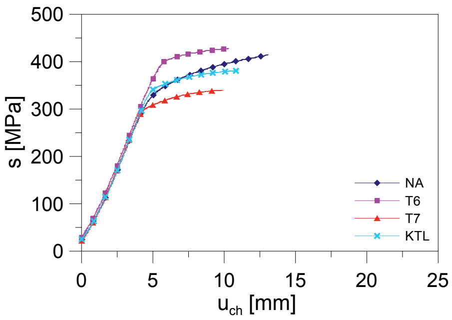

(a) Initial T4

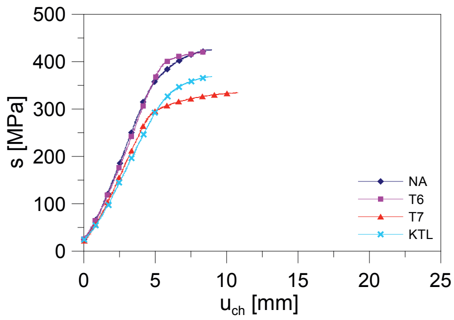

(b) Initial T6

Appendix 4: Cross-weld tensile test results for AA7046, after NA and PWHT – Engineering stress vs. Crosshead deformation

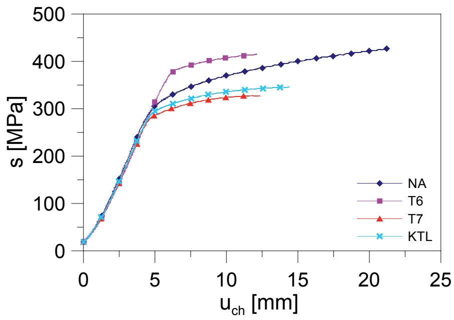

(a) Initial T4

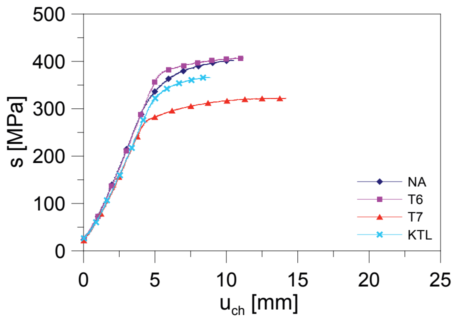

(b) Initial T6

Appendix 5: Cross-weld tensile test results for AA7108, after NA and PWHT – Engineering stress vs. Crosshead deformation

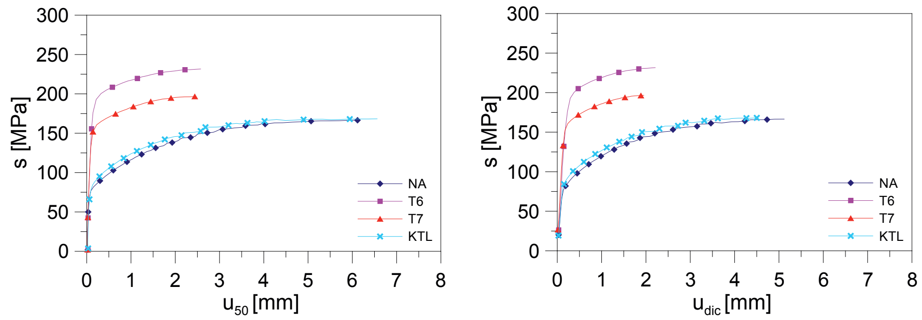

Appendix 6: Stress-deformation curves of cross-weld tensile tests between machine extensometer (u50) and digital extensometer (udic) for AA6005, initial T4

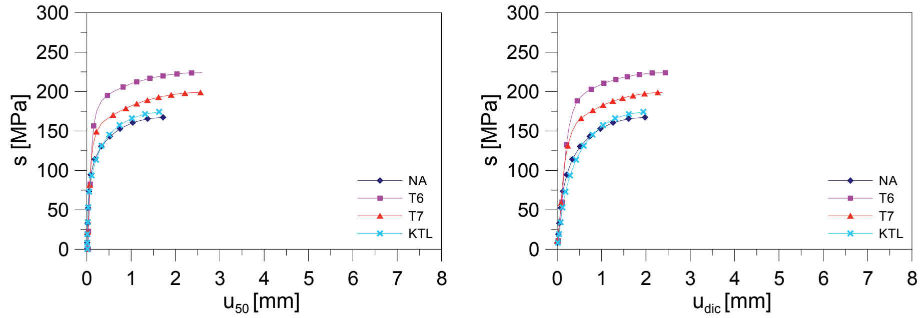

Appendix 7: Stress-deformation curves of cross-weld tensile tests between machine extensometer (u50) and digital extensometer (udic) for AA6005, initial T6

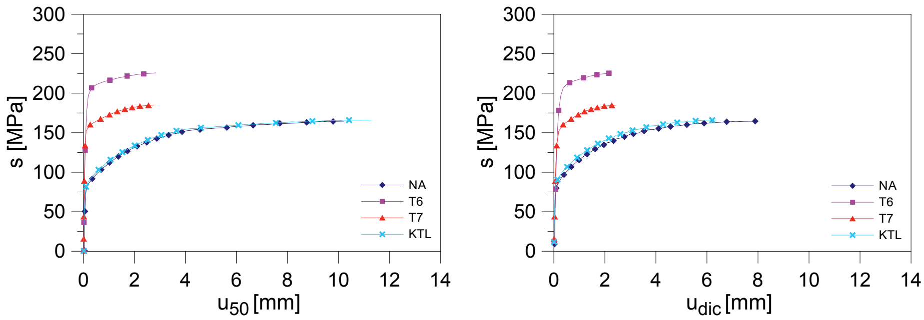

Appendix 8: Stress-deformation curves of cross-weld tensile tests between machine extensometer (u50) and digital extensometer (udic) for AA6060, initial T4

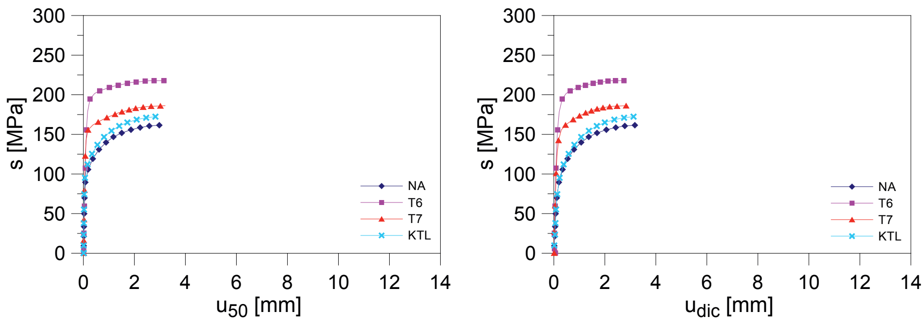

Appendix 9: Stress-deformation curves of cross-weld tensile tests between machine extensometer (u50) and digital extensometer (udic) for AA6060, initial T6

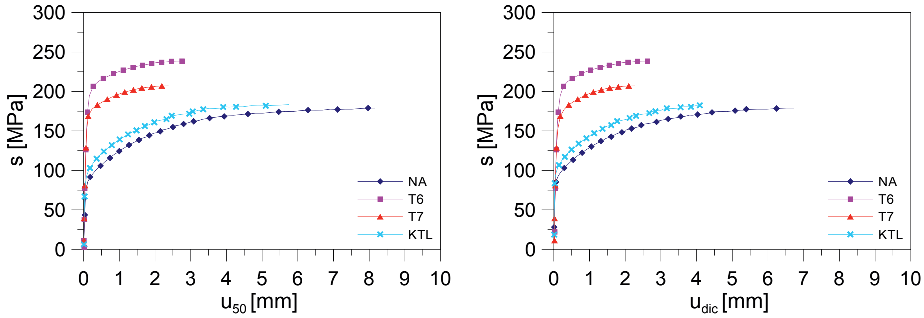

Appendix 10: Stress-deformation curves of cross-weld tensile tests between machine extensometer (u_{50}) and digital extensometer (u_{dic}) for AA6061, initial T4

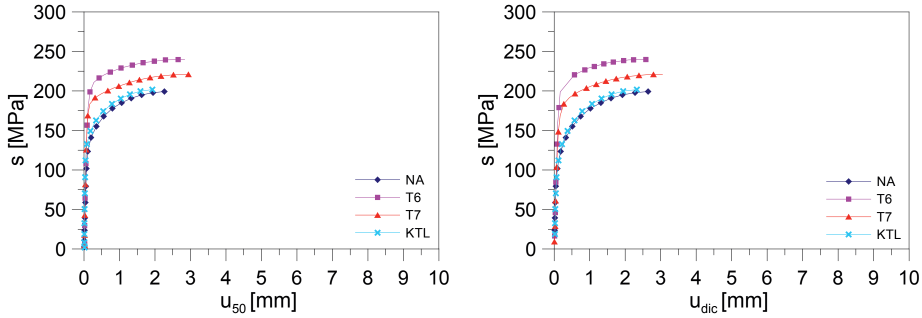

Appendix 11: Stress-deformation curves of cross-weld tensile tests between machine extensometer (u_{50}) and digital extensometer (u_{dic}) for AA6061, initial T6

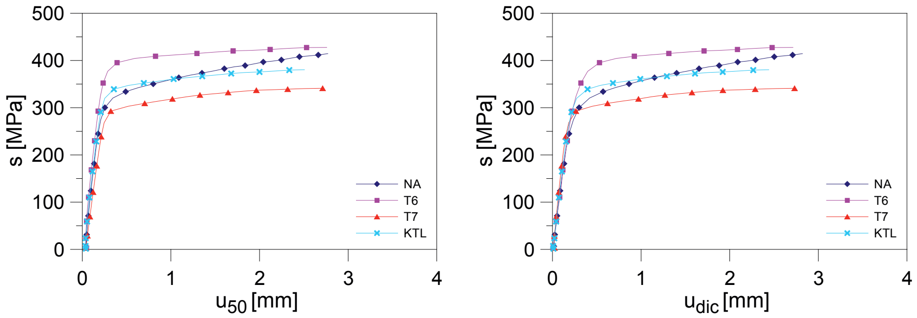

Appendix 12: Stress-deformation curves of cross-weld tensile tests between machine extensometer (u_{50}) and digital extensometer (u_{dic}) for AA7046, initial T4

118

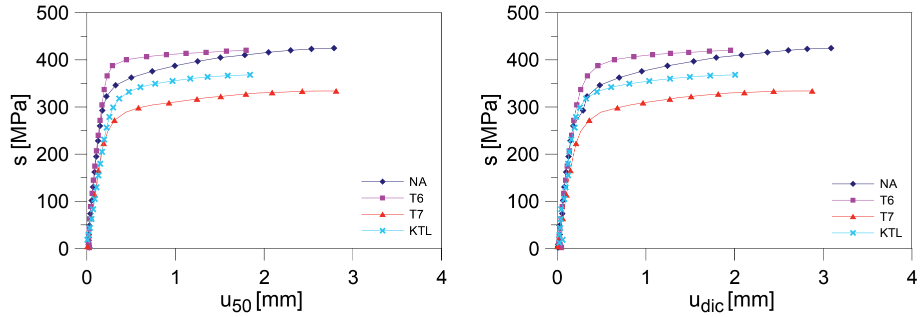

Appendix 13: Stress-deformation curves of cross-weld tensile tests between machine extensometer (u_{50}) and digital extensometer (u_{dic}) for AA7046, initial T6

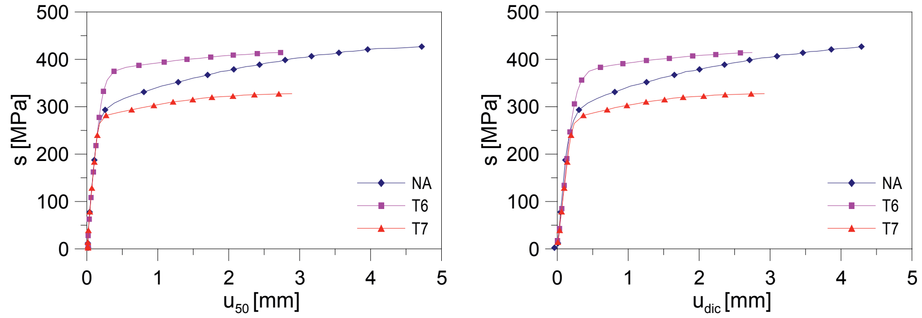

Appendix 14: Stress-deformation curves of cross-weld tensile tests between machine extensometer (u_{50}) and digital extensometer (u_{dic}) for AA7108, initial T4

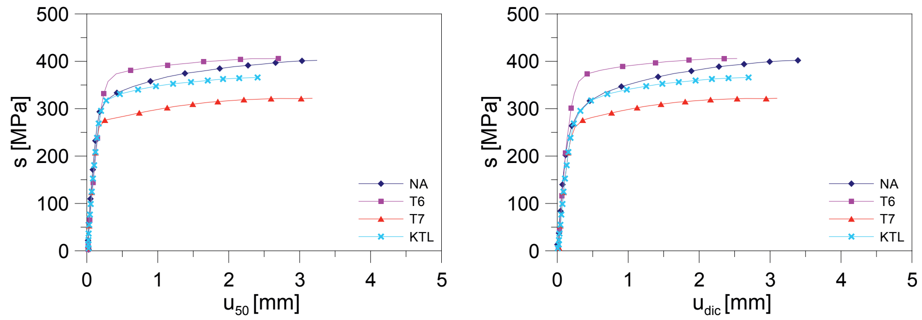

Appendix 15: Stress-deformation curves of cross-weld tensile tests between machine extensometer (u_{50}) and digital extensometer (u_{dic}) for AA7108, initial T6

DEPARTMENT OF STRUCTURAL ENGINEERING
NORWEGIAN UNIVERSITY OF SCIENCE AND TECHNOLOGY

N–7491 TRONDHEIM, NORWAY
Telephone: +47 73 59 47 00 Telefax: +47 73 59 47 01

"Reliability Analysis of Structural Systems using Nonlinear Finite Element Methods",
C. A. Holm, 1990:23, ISBN 82-7119-178-0.

"Uniform Stratified Flow Interaction with a Submerged Horizontal Cylinder",
Ø. Arntsen, 1990:32, ISBN 82-7119-188-8.

"Large Displacement Analysis of Flexible and Rigid Systems Considering Displacement-Dependent Loads and Nonlinear Constraints",
K. M. Mathisen, 1990:33, ISBN 82-7119-189-6.

"Solid Mechanics and Material Models including Large Deformations",
E. Levold, 1990:56, ISBN 82-7119-214-0, ISSN 0802-3271.

"Inelastic Deformation Capacity of Flexurally-Loaded Aluminium Alloy Structures",
T. Welo, 1990:62, ISBN 82-7119-220-5, ISSN 0802-3271.

"Visualization of Results from Mechanical Engineering Analysis",
K. Aamnes, 1990:63, ISBN 82-7119-221-3, ISSN 0802-3271.

"Object-Oriented Product Modeling for Structural Design",
S. I. Dale, 1991:6, ISBN 82-7119-258-2, ISSN 0802-3271.

"Parallel Techniques for Solving Finite Element Problems on Transputer Networks",
T. H. Hansen, 1991:19, ISBN 82-7119-273-6, ISSN 0802-3271.

"Statistical Description and Estimation of Ocean Drift Ice Environments",
R. Korsnes, 1991:24, ISBN 82-7119-278-7, ISSN 0802-3271.

“Properties of concrete related to fatigue damage: with emphasis on high strength concrete”,
G. Petkovic, 1991:35, ISBN 82-7119-290-6, ISSN 0802-3271.

"Turbidity Current Modelling",
B. Brørs, 1991:38, ISBN 82-7119-293-0, ISSN 0802-3271.

"Zero-Slump Concrete: Rheology, Degree of Compaction and Strength. Effects of Fillers as Part Cement-Replacement",
C. Sørensen, 1992:8, ISBN 82-7119-357-0, ISSN 0802-3271.

"Nonlinear Analysis of Reinforced Concrete Structures Exposed to Transient Loading",
K. V. Høiseth, 1992:15, ISBN 82-7119-364-3, ISSN 0802-3271.

"Finite Element Formulations and Solution Algorithms for Buckling and Collapse Analysis of Thin Shells",
R. O. Bjærum, 1992:30, ISBN 82-7119-380-5, ISSN 0802-3271.

"Response Statistics of Nonlinear Dynamic Systems",
J. M. Johnsen, 1992:42, ISBN 82-7119-393-7, ISSN 0802-3271.

"Digital Models in Engineering. A Study on why and how engineers build and operate digital models for decisison support",
J. Høyte, 1992:75, ISBN 82-7119-429-1, ISSN 0802-3271.

"Sparse Solution of Finite Element Equations",
A. C. Damhaug, 1992:76, ISBN 82-7119-430-5, ISSN 0802-3271.

"Some Aspects of Floating Ice Related to Sea Surface Operations in the Barents Sea",
S. Løset, 1992:95, ISBN 82-7119-452-6, ISSN 0802-3271.

"Modelling of Cyclic Plasticity with Application to Steel and Aluminium Structures",
O. S. Hopperstad, 1993:7, ISBN 82-7119-461-5, ISSN 0802-3271.

"The Free Formulation: Linear Theory and Extensions with Applications to Tetrahedral Elements
with Rotational Freedoms",
G. Skeie, 1993:17, ISBN 82-7119-472-0, ISSN 0802-3271.

"Høyfast betongs motstand mot piggdekkslitasje. Analyse av resultater fra prøving i Veisliter'n",
T. Tveter, 1993:62, ISBN 82-7119-522-0, ISSN 0802-3271.

"A Nonlinear Finite Element Based on Free Formulation Theory for Analysis of Sandwich Structures",
O. Aamlid, 1993:72, ISBN 82-7119-534-4, ISSN 0802-3271.

"The Effect of Curing Temperature and Silica Fume on Chloride Migration and Pore Structure of High Strength Concrete",
C. J. Hauck, 1993:90, ISBN 82-7119-553-0, ISSN 0802-3271.

"Failure of Concrete under Compressive Strain Gradients",
G. Markeset, 1993:110, ISBN 82-7119-575-1, ISSN 0802-3271.

"An experimental study of internal tidal amphidromes in Vestfjorden",
J. H. Nilsen, 1994:39, ISBN 82-7119-640-5, ISSN 0802-3271.

"Structural analysis of oil wells with emphasis on conductor design",
H. Larsen, 1994:46, ISBN 82-7119-648-0, ISSN 0802-3271.

"Adaptive methods for non-linear finite element analysis of shell structures",
K. M. Okstad, 1994:66, ISBN 82-7119-670-7, ISSN 0802-3271.

"On constitutive modelling in nonlinear analysis of concrete structures",
O. Fyrileiv, 1994:115, ISBN 82-7119-725-8, ISSN 0802-3271.

"Fluctuating wind load and response of a line-like engineering structure with emphasis on motion-induced wind forces",
J. Bogunovic Jakobsen, 1995:62, ISBN 82-7119-809-2, ISSN 0802-3271.

"An experimental study of beam-columns subjected to combined torsion, bending and axial actions",
A. Aalberg, 1995:66, ISBN 82-7119-813-0, ISSN 0802-3271.

"Scaling and cracking in unsealed freeze/thaw testing of Portland cement and silica fume concretes",
S. Jacobsen, 1995:101, ISBN 82-7119-851-3, ISSN 0802-3271.

"Damping of water waves by submerged vegetation. A case study of laminaria hyperborea",
A. M. Dubi, 1995:108, ISBN 82-7119-859-9, ISSN 0802-3271.

"The dynamics of a slope current in the Barents Sea",
Sheng Li, 1995:109, ISBN 82-7119-860-2, ISSN 0802-3271.

"Modellering av delmaterialenes betydning for betongens konsistens",
Ernst Mørtsell, 1996:12, ISBN 82-7119-894-7, ISSN 0802-3271.

"Bending of thin-walled aluminium extrusions",
Birgit Søvik Opheim, 1996:60, ISBN 82-7119-947-1, ISSN 0802-3271.

"Material modelling of aluminium for crashworthiness analysis",
Torodd Berstad, 1996:89, ISBN 82-7119-980-3, ISSN 0802-3271.

"Estimation of structural parameters from response measurements on submerged floating tunnels",
Rolf Magne Larssen, 1996:119, ISBN 82-471-0014-2, ISSN 0802-3271.

“Numerical modelling of plain and reinforced concrete by damage mechanics”,
Mario A. Polanco-Loria, 1997:20, ISBN 82-471-0049-5, ISSN 0802-3271.

“Nonlinear random vibrations - numerical analysis by path integration methods”,
Vibeke Moe, 1997:26, ISBN 82-471-0056-8, ISSN 0802-3271.
“Numerical prediction of vortex-induced vibration by the finite element method”,
Joar Martin Dalheim, 1997:63, ISBN 82-471-0096-7, ISSN 0802-3271.

“Time domain calculations of buffeting response for wind sensitive structures”,
Ketil Aas-Jakobsen, 1997:148, ISBN 82-471-0189-0, ISSN 0802-3271.

"A numerical study of flow about fixed and flexibly mounted circular cylinders",
Trond Stokka Meling, 1998:48, ISBN 82-471-0244-7, ISSN 0802-3271.

“Estimation of chloride penetration into concrete bridges in coastal areas”,
Per Egil Steen, 1998:89, ISBN 82-471-0290-0, ISSN 0802-3271.

"Stress-resultant material models for reinforced concrete plates and shells",
Jan Arve Øverli, 1998:95, ISBN 82-471-0297-8, ISSN 0802-3271.

"Chloride binding in concrete. Effect of surrounding environment and concrete composition",
Claus Kenneth Larsen, 1998:101, ISBN 82-471-0337-0, ISSN 0802-3271.

"Rotational capacity of aluminium alloy beams",
Lars A. Moen, 1999:1, ISBN 82-471-0365-6, ISSN 0802-3271.

"Stretch Bending of Aluminium Extrusions",
Arild H. Clausen, 1999:29, ISBN 82-471-0396-6, ISSN 0802-3271.

"Aluminium and Steel Beams under Concentrated Loading",
Tore Tryland, 1999:30, ISBN 82-471-0397-4, ISSN 0802-3271.

"Engineering Models of Elastoplasticity and Fracture for Aluminium Alloys",
Odd-Geir Lademo, 1999:39, ISBN 82-471-0406-7, ISSN 0802-3271.

"Kapasitet og duktilitet av dybelforbindelser i trekonstruksjoner",
Jan Siem, 1999:46, ISBN 82-471-0414-8, ISSN 0802-3271.

"Etablering av distribuert ingeniørarbeid; Teknologiske og organisatoriske erfaringer fra en norsk ingeniørbedrift",
Lars Line, 1999:52, ISBN 82-471-0420-2, ISSN 0802-3271.

"Estimation of Earthquake-Induced Response",
Símon Ólafsson, 1999:73, ISBN 82-471-0443-1, ISSN 0802-3271.

"Coastal Concrete Bridges: Moisture State, Chloride Permeability and Aging Effects"
Ragnhild Holen Relling, 1999:74, ISBN 82-471-0445-8, ISSN 0802-3271.

"Capacity Assessment of Titanium Pipes Subjected to Bending and External Pressure",
Arve Bjørset, 1999:100, ISBN 82-471-0473-3, ISSN 0802-3271.

"Validation of Numerical Collapse Behaviour of Thin-Walled Corrugated Panels",
Håvar Ilstad, 1999:101, ISBN 82-471-0474-1, ISSN 0802-3271.

"Strength and Ductility of Welded Structures in Aluminium Alloys",
Miroslaw Matusiak, 1999:113, ISBN 82-471-0487-3, ISSN 0802-3271.

"Thermal Dilation and Autogenous Deformation as Driving Forces to Self-Induced Stresses in High Performance Concrete",
Øyvind Bjøntegaard, 1999:121, ISBN 82-7984-002-8, ISSN 0802-3271.

"Some Aspects of Ski Base Sliding Friction and Ski Base Structure",
Dag Anders Moldestad, 1999:137, ISBN 82-7984-019-2, ISSN 0802-3271.

"Electrode reactions and corrosion resistance for steel in mortar and concrete",
Roy Antonsen, 2000:10, ISBN 82-7984-030-3, ISSN 0802-3271.

"Hydro-Physical Conditions in Kelp Forests and the Effect on Wave Damping and Dune Erosion. A case study on Laminaria Hyperborea",
Stig Magnar Løvås, 2000:28, ISBN 82-7984-050-8, ISSN 0802-3271.

"Random Vibration and the Path Integral Method",
Christian Skaug, 2000:39, ISBN 82-7984-061-3, ISSN 0802-3271.

"Buckling and geometrical nonlinear beam-type analyses of timber structures",
Trond Even Eggen, 2000:56, ISBN 82-7984-081-8, ISSN 0802-3271.

"Structural Crashworthiness of Aluminium Foam-Based Components",
Arve Grønsund Hanssen, 2000:76, ISBN 82-7984-102-4, ISSN 0809-103X.

"Measurements and simulations of the consolidation in first-year sea ice ridges, and some aspects of mechanical behaviour",
Knut V. Høyland, 2000:94, ISBN 82-7984-121-0, ISSN 0809-103X.

"Kinematics in Regular and Irregular Waves based on a Lagrangian Formulation",
Svein Helge Gjøsund, 2000-86, ISBN 82-7984-112-1, ISSN 0809-103X.

"Self-Induced Cracking Problems in Hardening Concrete Structures",
Daniela Bosnjak, 2000-121, ISBN 82-7984-151-2, ISSN 0809-103X.

"Ballistic Penetration and Perforation of Steel Plates",
Tore Børvik, 2000:124, ISBN 82-7984-154-7, ISSN 0809-103X.

"Freeze-Thaw resistance of Concrete. Effect of: Curing Conditions, Moisture Exchange and Materials",
Terje Finnerup Rønning, 2001:14, ISBN 82-7984-165-2, ISSN 0809-103X

"Structural behaviour of post tensioned concrete structures. Flat slab. Slabs on ground",
Steinar Trygstad, 2001:52, ISBN 82-471-5314-9, ISSN 0809-103X.

"Slipforming of Vertical Concrete Structures. Friction between concrete and slipform panel",
Kjell Tore Fosså, 2001:61, ISBN 82-471-5325-4, ISSN 0809-103X.

"Some numerical methods for the simulation of laminar and turbulent incompressible flows",
Jens Holmen, 2002:6, ISBN 82-471-5396-3, ISSN 0809-103X.

"Improved Fatigue Performance of Threaded Drillstring Connections by Cold Rolling",
Steinar Kristoffersen, 2002:11, ISBN: 82-421-5402-1, ISSN 0809-103X.

"Deformations in Concrete Cantilever Bridges: Observations and Theoretical Modelling",
Peter F. Takâcs, 2002:23, ISBN 82-471-5415-3, ISSN 0809-103X.

"Stiffened aluminium plates subjected to impact loading",
Hilde Giæver Hildrum, 2002:69, ISBN 82-471-5467-6, ISSN 0809-103X.

"Full- and model scale study of wind effects on a medium-rise building in a built up area", Jónas Thór Snæbjørnsson, 2002:95, ISBN82-471-5495-1, ISSN 0809-103X.

"Evaluation of Concepts for Loading of Hydrocarbons in Ice-infested water", Arnor Jensen, 2002:114, ISBN 82-417-5506-0, ISSN 0809-103X.

"Numerical and Physical Modelling of Oil Spreading in Broken Ice", Janne K. Økland Gjøsteen, 2002:130, ISBN 82-471-5523-0, ISSN 0809-103X.

"Diagnosis and protection of corroding steel in concrete", Franz Pruckner, 20002:140, ISBN 82-471-5555-4, ISSN 0809-103X.

"Tensile and Compressive Creep of Young Concrete: Testing and Modelling", Dawood Atrushi, 2003:17, ISBN 82-471-5565-6, ISSN 0809-103X.

"Rheology of Particle Suspensions. Fresh Concrete, Mortar and Cement Paste with Various Types of Lignosulfonates", Jon Elvar Wallevik, 2003:18, ISBN 82-471-5566-4, ISSN 0809-103X.

"Oblique Loading of Aluminium Crash Components", Aase Reyes, 2003:15, ISBN 82-471-5562-1, ISSN 0809-103X.

"Utilization of Ethiopian Natural Pozzolans", Surafel Ketema Desta, 2003:26, ISSN 82-471-5574-5, ISSN:0809-103X.

"Behaviour and strength prediction of reinforced concrete structures with discontinuity regions", Helge Brå, 2004:11, ISBN 82-471-6222-9, ISSN 1503-8181.

"High-strength steel plates subjected to projectile impact. An experimental and numerical study", Sumita Dey, 2004:38, ISBN 82-471-6282-2 (printed version), ISBN 82-471-6281-4 (electronic version), ISSN 1503-8181.

"Alkali-reactive and inert fillers in concrete. Rheology of fresh mixtures and expansive reactions." Bård M. Pedersen, 2004:92, ISBN 82-471-6401-9 (printed version), ISBN 82-471-6400-0 (electronic version), ISSN 1503-8181.

"On the Shear Capacity of Steel Girders with Large Web Openings". Nils Christian Hagen, 2005:9 ISBN 82-471-6878-2 (printed version), ISBN 82-471-6877-4 (electronic version), ISSN 1503-8181.

"Behaviour of aluminium extrusions subjected to axial loading". Østen Jensen, 2005:7, ISBN 82-471-6873-1 (printed version), ISBN 82-471-6872-3 (electronic version), ISSN 1503-8181.

"Thermal Aspects of corrosion of Steel in Concrete". Jan-Magnus Østvik, 2005:5, ISBN 82-471-6869-3 (printed version), ISBN 82-471-6868 (electronic version), ISSN 1503-8181.

”Mechanical and adaptive behaviour of bone in relation to hip replacement.” A study of bone remodelling and bone grafting.
Sébastien Muller, 2005:34, ISBN 82-471-6933-9 (printed version), ISBN 82-471-6932-0 (electronic version), ISSN 1503-8181.

“Analysis of geometrical nonlinearities with applications to timber structures”.
Lars Wollebæk, 2005:74, ISBN 82-471-7050-5 (printed version), ISBN 82-471-7019-1 (electronic version), ISSN 1503-8181.

“Pedestrian induced lateral vibrations of slender footbridges”,
Anders Rönnquist, 2005:102, ISBN 82-471-7082-5 (printed version), ISBN 82-471-7081-7 (electronic version), ISSN 1503-8181.

“Initial Strength Development of Fly Ash and Limestone Blended Cements at Various Temperatures Predicted by Ultrasonic Pulse Velocity”,
Tom Ivar Fredvik, 2005:112, ISBN 82-471-7105-8 (printed version), ISBN 82-471-7103-1 (electronic version), ISSN 1503-8181.

“Behaviour and modelling of thin-walled cast components”,
Cato Dørum, 2005:128, ISBN 82-471-7140-6 (printed version), ISBN 82-471-7139-2 (electronic version), ISSN 1503-8181.

“Behaviour and modelling of selfpiercing riveted connections”,
Raffaele Porcaro, 2005:165, ISBN 82-471-7219-4 (printed version), ISBN 82-471-7218-6 (electronic version), ISSN 1503-8181.

”Behaviour and Modelling og Aluminium Plates subjected to Compressive Load”,
Lars Rønning, 2005:154, ISBN 82-471-7169-1 (printed version), ISBN 82-471-7195-3 (electronic version), ISSN 1503-8181.

”Bumper beam-longitudinal system subjected to offset impact loading”,
Satyanarayana Kokkula, 2005:193, ISBN 82-471-7280-1 (printed version), ISBN 82-471-7279-8 (electronic version), ISSN 1503-8181.

“Control of Chloride Penetration into Concrete Structures at Early Age”,
Guofei Liu, 2006:46, ISBN 82-471-7838-9 (printed version), ISBN 82-471-7837-0 (electronic version), ISSN 1503-8181.

“Modelling of Welded Thin-Walled Aluminium Structures”,
Ting Wang, 2006:78, ISBN 82-471-7907-5 (printed version), ISBN 82-471-7906-7 (electronic version), ISSN 1503-8181.

”Time-variant reliability of dynamic systems by importance sampling and probabilistic analysis of ice loads”,
Anna Ivanova Olsen, 2006:139, ISBN 82-471-8041-3 (printed version), ISBN 82-471-8040-5 (electronic version), ISSN 1503-8181.

“Fatigue life prediction of an aluminium alloy automotive component using finite element analysis of surface topography”.
Sigmund Kyrre Ås, 2006:25, ISBN 82-471-7791-9 (printed version), ISBN 82-471-7791-9 (electronic version), ISSN 1503-8181.

”Constitutive models of elastoplasticity and fracture for aluminium alloys under strain path change”,
Dasharatha Achani, 2006:76, ISBN 82-471-7903-2 (printed version), ISBN 82-471-7902-4 (electronic version), ISSN 1503-8181.

“Simulations of 2D dynamic brittle fracture by the Element-free Galerkin method and linear fracture mechanics”,
Tommy Karlsson, 2006:125, ISBN 82-471-8011-1 (printed version), ISBN 82-471-8010-3 (electronic version), ISSN 1503-8181.

“Penetration and Perforation of Granite Targets by Hard Projectiles”,
Chong Chiang Seah, 2006:188, ISBN 82-471-8150-9 (printed version), ISBN 82-471-8149-5 (electronic version), ISSN 1503-8181.

“Deformations, strain capacity and cracking of concrete in plastic and early hardening phases”,
Tor Arne Hammer, 2007:234, ISBN 978-82-471-5191-4 (printed version), ISBN 978-82-471-5207-2 (electronic version), ISSN 1503-8181.

“Crashworthiness of dual-phase high-strength steel: Material and Component behaviour”,
Venkatapathi Tarigopula, 2007:230, ISBN 82-471-5076-4 (printed version), ISBN 82-471-5093-1 (electronic version), ISSN 1503-8181.

“Fibre reinforcement in load carrying concrete structures”,
Åse Lyslo Døssland, 2008:50, ISBN 978-82-471-6910-0 (printed version), ISBN 978-82-471-6924-7 (electronic version), ISSN 1503-8181.

“Low-velocity penetration of aluminium plates”,
Frode Grytten, 2008:46, ISBN 978-82-471-6826-4 (printed version), ISBN 978-82-471-6843-1 (electronic version), ISSN 1503-8181.

“Robustness studies of structures subjected to large deformations”,
Ørjan Fyllingen, 2008:24, ISBN 978-82-471-6339-9 (printed version), ISBN 978-82-471-6342-9 (electronic version), ISSN 1503-8181.

“Constitutive modelling of morsellised bone”,
Knut Birger Lunde, 2008:92, ISBN 978-82-471-7829-4 (printed version), ISBN 978-82-471-7832-4 (electronic version), ISSN 1503-8181.

“Experimental Investigations of Wind Loading on a Suspension Bridge Girder”,
Bjørn Isaksen, 2008:131, ISBN 978-82-471-8656-5 (printed version), ISBN 978-82-471-8673-2 (electronic version), ISSN 1503-8181.

“Cracking Risk of Concrete Structures in The Hardening Phase”,
Guomin Ji, 2008:198, ISBN 978-82-471-1079-9 (printed version), ISBN 978-82-471-1080-5 (electronic version), ISSN 1503-8181.

“Modelling and numerical analysis of the porcine and human mitral apparatus”,
Victorien Emile Prot, 2008:249, ISBN 978-82-471-1192-5 (printed version), ISBN 978-82-471-1193-2 (electronic version), ISSN 1503-8181.

“Strength analysis of net structures”,
Heidi Moe, 2009:48, ISBN 978-82-471-1468-1 (printed version), ISBN 978-82-471-1469-8 (electronic version), ISSN1503-8181.

“Numerical analysis of ductile fracture in surface cracked shells”,
Espen Berg, 2009:80, ISBN 978-82-471-1537-4 (printed version), ISBN 978-82-471-1538-1 (electronic version), ISSN 1503-8181.

“Subject specific finite element analysis of bone – for evaluation of the healing of a leg lengthening and evaluation of femoral stem design”,
Sune Hansborg Pettersen, 2009:99, ISBN 978-82-471-1579-4 (printed version), ISBN 978-82-471-1580-0 (electronic version), ISSN 1503-8181.

“Evaluation of fracture parameters for notched multi-layered structures”,
Lingyun Shang, 2009:137, ISBN 978-82-471-1662-3 (printed version), ISBN 978-82-471-1663-0 (electronic version), ISSN 1503-8181.

“Modelling of Dynamic Material Behaviour and Fracture of Aluminium Alloys for Structural Applications”
Yan Chen, 2009:69, ISBN 978-82-471-1515-2 (printed version), ISBN 978-82 471-1516-9 (electronic version), ISSN 1503-8181.

“Nanomechanics of polymer and composite particles”
Jianying He 2009:213, ISBN 978-82-471-1828-3 (printed version), ISBN 978-82-471-1829-0 (electronic version), ISSN 1503-8181.

“Mechanical properties of clear wood from Norway spruce”
Kristian Berbom Dahl 2009:250, ISBN 978-82-471-1911-2 (printed version) ISBN 978-82-471-1912-9 (electronic version), ISSN 1503-8181.

“Modeling of the degradation of TiB_2 mechanical properties by residual stresses and liquid Al penetration along grain boundaries”
Micol Pezzotta 2009:254, ISBN 978-82-471-1923-5 (printed version) ISBN 978-82-471-1924-2 (electronic version) ISSN 1503-8181.

“Effect of welding residual stress on fracture”
Xiabo Ren 2010:77, ISBN 978-82-471-2115-3 (printed version) ISBN 978-82-471-2116-0 (electronic version), ISSN 1503-8181.

“Pan-based carbon fiber as anode material in cathodic protection system for concrete structures”
Mahdi Chini 2010:122, ISBN 978-82-471-2210-5 (printed version) ISBN 978-82-471-2213-6 (electronic version), ISSN 1503-8181.

“Structural Behaviour of deteriorated and retrofitted concrete structures”
Irina Vasililjeva Sæther 2010:171, ISBN 978-82-471-2315-7 (printed version) ISBN 978-82-471-2316-4 (electronic version) ISSN 1503-8181.

“Prediction of local snow loads on roofs”
Vivian Meløysund 2010:247, ISBN 978-82-471-2490-1 (printed version) ISBN 978-82-471-2491-8 (electronic version) ISSN 1503-8181.

“Behaviour and modelling of polymers for crash applications”
Virgile Delhaye 2010:251, ISBN 978-82-471-2501-4 (printed version) ISBN 978-82-471-2502-1 (electronic version) ISSN 1503-8181.
“Blended cement with reducted CO_2 emission – Utilizing the Fly Ash-Limestone Synergy”,
Klaartje De Weerdt 2011:32, ISBN 978-82-471-2584-7 (printed version) ISBN 978-82-471-2584-4 (electronic version) ISSN 1503-8181.

“Chloride induced reinforcement corrosion in concrete” Concept of critical chloride content – methods and mechanisms.
Ueli Angst 2011:113, ISBN 978-82-471-2769-9 (printed version) ISBN 978-82-471-2763-6 (electronic version) ISSN 1503-8181.

“A thermo-electric-Mechanical study of the carbon anode and contact interface for Energy savings in the production of aluminium”.
Dag Herman Andersen 2011:157, ISBN 978-82-471-2859-6 (printed version) ISBN 978-82-471-2860-2 (electronic version) ISSN 1503-8181.

“Structural Capacity of Anchorage Ties in Masonry Veneer Walls Subjected to Earthquake”. The implications of Eurocode 8 and Eurocode 6 on a typical Norwegain veneer wall.
Ahmed Mohamed Yousry Hamed 2011:181, ISBN 978-82-471-2911-1 (printed version) ISBN 978-82-471-2912-8 (electronic ver.) ISSN 1503-8181.

“Work-hardening behaviour in age-hardenable Al-Zn-Mg(-Cu) alloys”.
Ida Westermann , 2011:247, ISBN 978-82-471-3056-8 (printed ver.) ISBN 978-82-471-3057-5 (electronic ver.) ISSN 1503-8181.

“Behaviour and modelling of selfpiercing riveted connections using aluminium rivets”.
Nguyen-Hieu Hoang, 2011:266, ISBN 978-82-471-3097-1 (printed ver.) ISBN 978-82-471-3099-5 (electronic ver.) ISSN 1503-8181.

“Fibre reinforced concrete”.
Sindre Sandbakk, 2011:297, ISBN 978-82-471-3167-1 (printed ver.) ISBN 978-82-471-3168-8 (electronic ver) ISSN 1503:8181.

“Dynamic behaviour of cablesupported bridges subjected to strong natural wind”.
Ole Andre Øiseth, 2011:315, ISBN 978-82-471-3209-8 (printed ver.) ISBN 978-82-471-3210-4 (electronic ver.) ISSN 1503-8181.

“Constitutive modeling of solargrade silicon materials”
Julien Cochard, 2011:307, ISBN 978-82-471-3189-3 (printed ver). ISBN 978-82-471-3190-9 (electronic ver.) ISSN 1503-8181.

“Constitutive behavior and fracture of shape memory alloys”
Jim Stian Olsen, 2012:57, ISBN 978-82-471-3382-8 (printed ver.) ISBN 978-82-471-3383-5 (electronic ver.) ISSN 1503-8181.

“Field measurements in mechanical testing using close-range photogrammetry and digital image analysis”
Egil Fagerholt, 2012:95, ISBN 978-82-471-3466-5 (printed ver.) ISBN 978-82-471-3467-2 (electronic ver.) ISSN 1503-8181.

“Towards a better under standing of the ultimate behaviour of lightweight aggregate concrete in compression and bending”,
Håvard Nedrelid, 2012:123, ISBN 978-82-471-3527-3 (printed ver.) ISBN 978-82-471-3528-0 (electronic ver.) ISSN 1503-8181.

“Numerical simulations of blood flow in the left side of the heart”
Sigrid Kaarstad Dahl, 2012:135, ISBN 978-82-471-3553-2 (printed ver.) ISBN 978-82-471-3555-6 (electronic ver.) ISSN 1503-8181.

“Moisture induced stresses in glulam”
Vanessa Angst-Nicollier, 2012:139, ISBN 978-82-471-3562-4 (printed ver.) ISBN 978-82-471-3563-1 (electronic ver.) ISSN 1503-8181.

“Biomechanical aspects of distraction osteogensis”
Valentina La Russa, 2012:250, ISBN 978-82-471-3807-6 (printed ver.) ISBN 978-82-471-3808-3 (electronic ver.) ISSN 1503-8181.

“Ductile fracture in dual-phase steel. Theoretical, experimental and numerical study”
Gaute Gruben, 2012:257, ISBN 978-82-471-3822-9 (printed ver.) ISBN 978-82-471-3823-6 (electronic ver.) ISSN 1503-8181.

“Damping in Timber Structures”
Nathalie Labonnote, 2012:263, ISBN 978-82-471-3836-6 (printed ver.) ISBN 978-82-471-3837-3 (electronic ver.) ISSN 1503-8181.

“Biomechanical modeling of fetal veins: The umbilical vein and ductus venosus bifurcation”
Paul Roger Leinan, 2012:299, ISBN 978-82-471-3915-8 (printed ver.) ISBN 978-82-471-3916-5 (electronic ver.) ISSN 1503-8181.

“Large-Deformation behaviour of thermoplastics at various stress states”
Anne Serine Ognedal, 2012:298, ISBN 978-82-471-3913-4 (printed ver.) ISBN 978-82-471-3914-1 (electronic ver.) ISSN 1503-8181.

“Hardening accelerator for fly ash blended cement”
Kien Dinh Hoang, 2012:366, ISBN 978-82-471-4063-5 (printed ver.) ISBN 978-82-471-4064-2 (electronic ver.) ISSN 1503-8181.

"From molecular structure to mechanical properties"
Jianyang Wu, 2013:186, ISBN 978-82-471-4485-5 (printed ver.) ISBN 978-82-471-4486-2 (electronic ver.) ISSN 1503-8181.

"Experimental and numerical study of hybrid concrete structures"
Linn Grepstad Nes, 2013:259, ISBN 978-82-471-4644-6 (printed ver.) ISBN 978-82-471-4645-3 (electronic ver.) ISSN 1503-8181.

"Mechanics of ultra-thin multi crystalline silicon wafers"
Saber Saffar, 2013:199, ISBN 978-82-471-4511-1 (printed ver.) ISBN 978-82-471-4513-5 (electronic ver). ISSN 1503-8181.